



## **Gas-Cooled Fast Reactor (GFR) FY05 Annual Report**

September 30, 2005

**INL/EXT-05-00799**  
**Rev 0**

# **Gas-Cooled Fast Reactor (GFR) FY05 Annual Report**

**September 30, 2005**

**Idaho National Laboratory  
Idaho Falls, Idaho 83415**

**Prepared for the  
U.S. Department of Energy  
Under DOE Idaho Operations Office  
Contract DE-AC07-05ID14517**



## Contributors

### **Idaho National Laboratory**

K. D. Weaver  
T. Marshall  
T. Totemeier  
J. Gan

### **Argonne National Laboratory**

E.E. Feldman  
E.A. Hoffman  
R.F. Kulak  
I.U. Therios  
C. P. Tzanos  
T.Y.C. Wei

### **Brookhaven National Laboratory**

L-Y. Cheng  
H. Ludewig  
J. Jo

### **Oak Ridge National Laboratory**

R. Nanstad  
W. Corwin

### **Auburn University**

V. G. Krishnardula  
W. F. Gale  
J. W. Fergus

### **University of Wisconsin- Madison**

T. Allen

### **Idaho State University**

P. Sabharwall

## Table of Contents

<b>1. Introduction .....</b>	<b>- 6 -</b>
<b>2. Design Options for the GFR.....</b>	<b>- 7 -</b>
2.1 Reference Design.....	- 7 -
2.2 Optional Designs.....	- 7 -
2.3 GFR Fuel.....	- 8 -
<b>3. GFR System Safety, Design, and Integration .....</b>	<b>- 9 -</b>
3.1 Modeling of GFR Decay Heat Removal in a Depressurization Accident....	- 10 -
3.1.1 Reactor and Emergency Cooling System.....	- 10 -
3.1.1.1 Hydraulic Volumes and Heat Structures.....	- 11 -
3.1.1.2 Radiative Heat Transfer .....	- 13 -
3.1.1.3 Emergency Cooling System.....	- 14 -
3.1.2 Reactor Cavity Cooling System.....	- 15 -
3.1.3 Power Conversion Unit.....	- 17 -
3.1.4 Results Of Analysis.....	- 19 -
3.1.4.1 Initial Results .....	- 19 -
3.1.4.2 Results with RCCS .....	- 21 -
3.1.5 Summary and Conclusions.....	- 27 -
3.2 Heated Region Flow Starvation .....	- 28 -
3.3 Large GFR Core Subassembly Design .....	- 31 -
3.3.1 Core Neutronics Design.....	- 32 -
3.3.1.1 Reference Case.....	- 32 -
3.3.1.2 Fuel Cycle and Neutronics Modeling .....	- 33 -
3.3.1.3 Radial Power Distribution.....	- 34 -
3.3.1.4 Control Rod Worth and Safety Parameter Evaluation .....	- 50 -
3.3.1.5 Conclusions .....	- 52 -
3.3.2 Fuel Pin Mechanical Design .....	- 52 -
3.3.2.1 Fuel Pin Geometry .....	- 53 -
3.3.2.2 Fuel Pin and Hexcan Temperature Distributions .....	- 54 -
3.3.2.3 Fuel Pin Material Properties .....	- 55 -
3.3.2.4 Fuel Pin Structural Analysis Configurations .....	- 55 -
3.3.2.5 Fuel Pin Analysis Displacement Results .....	- 59 -
3.3.2.6 Fuel Pin Structural Analysis Results Summary.....	- 65 -
3.3.2.7 Summary and Conclusions.....	- 66 -
3.3.3 Subassembly Thermal-Hydraulic Design .....	- 67 -
3.3.3.1 Subassembly Geometry.....	- 68 -
3.3.3.2 Analytical Model.....	- 69 -
3.3.3.3 Results and Discussion.....	- 70 -
3.3.3.4 Conclusions .....	- 77 -
3.4 Guard Containment CFD Analysis.....	- 77 -
3.4.1 2400 MWt Plant Layout.....	- 78 -
3.4.2 Decay Heat Accidents .....	- 80 -
3.4.3 Guard Containment CFD Model.....	- 81 -
3.4.4 Long Term Steady State Analysis.....	- 83 -

3.4.5	Transient Analysis.....	- 88 -
3.5	<i>System Integration</i> .....	94
<b>4.</b>	<b>GFR Materials for Moderate to High Temperature Use.....</b>	<b>95</b>
4.1	<i>ODS Joining Studies</i> .....	95
4.1.1	Torsional Resistance Pressure Welding.....	95
4.1.1.1	Resistance Pressure Welding Conclusions .....	97
4.1.2	Transient Liquid Phase Bonding of Ferritic ODS Alloys .....	97
4.1.2.1	Substrate and Interlayer Materials .....	97
4.1.2.2	Bonding Trials and Post-Bond Heat-Treatment.....	97
4.1.2.3	Plans for the Next Phase of the Project.....	102
4.2	<i>Ion Irradiation Study on Microstructure Stability of GFR Ceramics: ZrC, ZrN, TiC, TiN and SiC</i> .....	104
4.2.1	Experiments .....	106
4.2.2	Results .....	107
4.2.2.1	ZrC .....	107
4.2.2.2	ZrN.....	108
4.2.2.3	TiC .....	108
4.2.2.4	TiN .....	109
4.2.2.5	SiC.....	109
4.2.3	Discussion .....	110
4.2.3.1	ZrC .....	110
4.2.3.2	ZrN.....	111
4.2.3.3	TiC & TiN.....	111
4.2.3.4	SiC.....	112
4.2.4	Summary and Conclusions.....	113
4.3	<i>Grain Boundary Engineering</i> .....	136
4.3.1	Coordination for I-NERI Project 2004-007-F.....	136
4.3.2	Performance and Stability of Grain Boundary Engineering Alloy 800H .....	136
<b>5.</b>	<b>Fuels .....</b>	<b>139</b>



## **1. Introduction**

The gas-cooled fast reactor (GFR) was chosen as one of the Generation IV nuclear reactor systems to be developed based on its excellent potential for sustainability through reduction of the volume and radio toxicity of both its own fuel and other spent nuclear fuel, and for extending/utilizing uranium resources orders of magnitude beyond what the current open fuel cycle can realize. In addition, energy conversion at high thermal efficiency is possible with the current designs being considered, thus increasing the economic benefit of the GFR. However, research and development challenges include the ability to use passive decay heat removal systems during accident conditions, survivability of fuels and in-core materials under extreme temperatures and radiation, and economical and efficient fuel cycle processes. Nevertheless, the GFR was chosen as one of only six Generation IV systems to be pursued based on its ability to meet the Generation IV goals in sustainability, economics, safety and reliability, proliferation resistance and physical protection.

Current research and development on the Gas-Cooled Fast Reactor (GFR) has focused on the design of safety systems that will remove the decay heat during accident conditions, ion irradiations of candidate ceramic materials, joining studies of oxide dispersion strengthened alloys; and within the Advanced Fuel Cycle Initiative (AFCI) the fabrication of carbide fuels and ceramic fuel matrix materials, development of non-halide precursor low density and high density ceramic coatings, and neutron irradiation of candidate ceramic fuel matrix and metallic materials. The vast majority of this work has focused on the reference design for the GFR: a helium-cooled, direct power conversion system that will operate with on outlet temperature of 850°C at 7 MPa.

In addition to the work being performed in the United States, seven international partners under the Generation IV International Forum (GIF) have identified their interest in participating in research related to the development of the GFR. These are Euratom (European Commission), France, Japan, South Africa, South Korea, Switzerland, and the United Kingdom. Of these, Euratom (including the United Kingdom and Switzerland), France, and Japan have active research activities with respect to the GFR. The research includes GFR design and safety, and fuels/in-core materials/fuel cycle projects. This report outlines the current design status of the GFR, and includes work done in the areas mentioned above for this fiscal year. In addition, this report fulfills the Level 2 milestones, “Complete annual status report on GFR reactor design,” and “Complete annual status report on pre-conceptual GFR reactor designs” in workpackage G-I0401K01.

GFR funding for FY05 included FY04 carryover funds, and was comprised of multiple tasks. These tasks involved a consortium of national laboratories and universities, including the Idaho National Laboratory (INL), Argonne National Laboratory (ANL), Brookhaven National Laboratory (BNL), Oak Ridge National Laboratory (ORNL), Auburn University (AU), Idaho State University (ISU), and the University of Wisconsin-Madison (UW-M).

## 2. Design Options for the GFR

### 2.1 Reference Design

The reference GFR system features a fast-spectrum, helium-cooled reactor and closed fuel cycle (see Figure 1). This was chosen as the reference design due to its close relationship with the VHTR, and thus its ability to utilize as much VHTR material and balance-of-plant technology as possible. Like thermal-spectrum helium-cooled reactors such as the Gas-Turbine Modular Helium Reactor (GT-MHR) and the Pebble Bed Modular Reactor (PBMR), the high outlet temperature of the helium coolant makes it possible to deliver electricity, hydrogen, or process heat with high conversion efficiency. The GFR reference design will utilize a direct-cycle helium turbine for electricity (42% efficiency at 850°C), and process heat for thermochemical production of hydrogen.

In order to withstand the high temperatures within the reactor, special consideration must be given to the fuel and in-core materials. The reference fuel matrix for the Generation IV GFR is a cermet dispersion fuel in a refractory ceramic matrix, based on a balance between conductivity and high temperature capability. These fuels will be mixed carbide or nitrides.

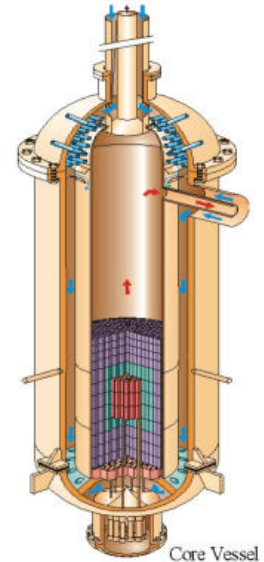


Figure 1. Schematic of the GFR vessel and core configuration for block/plate core.

### 2.2 Optional Designs

The primary optional design is also a helium-cooled system, but utilizes an indirect Brayton cycle for power conversion. The secondary system of the alternate design utilizes supercritical CO<sub>2</sub> (S-CO<sub>2</sub>) at 550°C and 20 MPa (see Figure 2). This allows for more modest outlet temperatures in the primary circuit (~ 600-650°C), reducing the strict fuel, fuel matrix, and material requirements as compared to the direct cycle, while maintaining high thermal efficiency (~ 42%).

The secondary optional design is a S-CO<sub>2</sub> cooled (550°C outlet and 20 MPa), direct Brayton cycle system. The main advantage of this design is the modest outlet temperature in the primary circuit, while maintaining high thermal efficiency (~ 45%). Again, the modest outlet temperature (comparable to sodium-cooled reactors) reduces the requirements on fuel, fuel matrix/cladding, and materials, and even allows for the use of more standard metal alloys within the core. This has the potential of significantly reducing the fuel matrix/cladding development costs as compared to the reference design, and reducing the overall capital costs due to the small size of the turbo machinery and other system components. The power conversion cycle is equivalent to that shown in Figure 2, where the IHX would be replaced by the reactor and reactor pressure vessel.

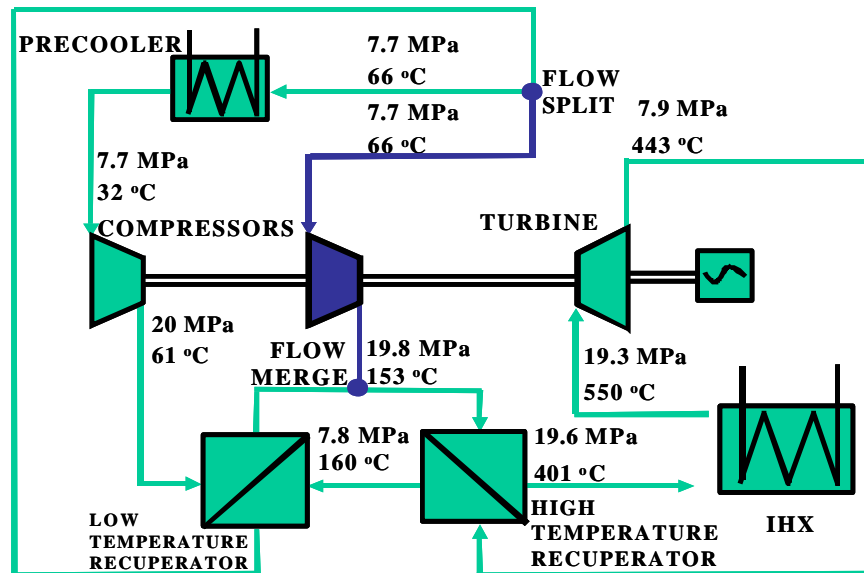


Figure 2. Schematic of the S-CO<sub>2</sub> recompression cycle.

### 2.3 GFR Fuel

The safety system design will be affected by the choice of primary coolant, whether a direct or indirect power conversion cycle is used, and the core geometry (i.e., block, plate, or pin). The trade-off between high conductivity and high temperature capabilities has led to the choice of ceramics, including refractory ceramics. The reference fuel matrix for the Generation IV GFR is a cermet dispersion fuel, based on a balance between conductivity and high temperature capability. The optional fuel is a ceramic fuel in a ceramic (composite) cladding.

Current fuel designs are based on dispersion fuels (either as fibers or particles) in an inert plate/block type matrix, with an option to use solid solution fuel clad in a refractory ceramic (e.g., SiC/SiC composites). The reference fuels chosen for the GFR are UC and UN for their high heavy metal density, high conductivity, and minimal impact on neutron spectrum (although limited irradiation data exists). The matrix materials are dependent on the coolant and operating temperatures, and can be classified into three categories: ceramic (for high temperatures), refractory metal (for modest to high temperatures), and metal (for modest temperatures).

It is important to note that fuel development, including fabrication and irradiation performance, is a key viability issue for the GFR, and cannot be separated from the safety design and performance of the GFR. Fuel mechanical and thermal properties are needed from beginning to end-of-life of the reactor to support the safety case, and will have a significant impact on the safety system design work. In addition, fuel development will include the viability of using minor actinide bearing material, which will have further effects on the performance of the GFR.

### **3. GFR System Safety, Design, and Integration**

Current design studies are focused on two power options, 600MWt and 2400MWt, utilizing a direct cycle with helium at 850°C outlet temperature, and 7MPa. The advantages to each of these power options are given below:

- 600 MWt
  - Enables “modular” design (i.e., small vessel, small core, etc., that can be transported to site)
  - Can utilize the 300 MWe VHTR balance-of-plant (BOP) development, thus minimizing R&D costs
- 2400 MWt
  - Better neutron economy, thus reducing the heavy metal inventory requirement
  - More adaptable to large base load operation
  - Can utilize current VHTR reactor pressure vessel size/technology (i.e., core will fit in current VHTR RPV)

Several core designs exist, and are presently being assessed using several performance measures, including safety characteristics that are addressed here. The GFR differs from the thermal gas reactor in several respects important for safety behavior. Past studies of the thermal gas reactor operating under a direct cycle have shown that safety for unprotected accidents is assured largely as a result of a very low power density, and a combination of a high temperature to fuel failure, large Doppler feedback, and large thermal inertia. By contrast, the power density in the GFR is an order of magnitude greater, the coolant density coefficient adds reactivity during depressurization accidents (which has no counterpart in the thermal core), and there are no large blocks of graphite (thermal inertia). These fundamental differences give the reactivity feedbacks a more prominent role in the safety of the fast reactor compared to the thermal gas reactor. As a consequence, an important design objective is to engineer the fast reactor core to have sufficient inherent negative reactivity feedback that core power safely adjusts to the available heat sink.

While a core layout and balance of plant exist for the 600 MWt design studied, the plant control system has not yet been designed. In addition, only preliminary designs for the 2400 MWt gas-cooled fast reactor have been evaluated. Note that the important aspect of the design is the removal of decay heat under depressurized conditions. Because the current fast reactor design is to have a power density of 50-100 W/cc, a flowing reactor coolant must remove most of the decay heat. A requirement that the reactor be passively safe during a total loss of power at the reactor site necessitates the employment of natural convection. Past studies have shown that natural convection is not effective at atmospheric pressure. Therefore, a guard containment that encloses the primary vessel is used to preserve a backpressure that maintains a high coolant density. During a total loss of site power, the leakage around the seals of the primary system will allow the reactor pressure to slowly decrease toward atmospheric pressure if it were not for the secondary (or guard) containment. The design goal is to limit the pressure that the guard



containment must maintain, since the cost of the guard containment increases with its required pressure capability.

### ***3.1 Modeling of GFR Decay Heat Removal in a Depressurization Accident***

The reactor system under consideration utilizes a closed helium Brayton cycle in its power conversion system. The reactor and the power conversion system are enclosed in a guard containment. The transient analysis of decay heat removal has been performed for a depressurization accident initiated by a postulated breach in the power conversion unit (PCU). Two passive decay heat removal mechanisms have been explicitly incorporated in the ATHENA model of the GFR. They are natural circulation and thermal radiation.

Owing to the coast down of the turbo-machine inside the PCU there is also a period of time during which forced flow cooling of the core is effective.

Decay heat removal by natural circulation cooling is enabled by an emergency cooling system (ECS) that directs the hot helium gas from the reactor to an ex-vessel heat exchanger. A dominant factor in determining the effectiveness of natural circulation cooling is the system pressure. A higher pressure results in a denser gas and that leads to a higher buoyancy head and subsequently a higher flow rate. In a depressurization accident initiated by a component breach the pressures of the reactor vessel and the guard containment will converge to an intermediate value. The impact of this common pressure on the maximum fuel temperature has been evaluated parametrically as part of the study [1].

An alternate means to remove decay heat is via the reactor cavity cooling system (RCCS) that surrounds the reactor vessel. Core decay heat is transferred to the reactor vessel by conduction and radiation and the RCCS absorbs the thermal energy from the reactor vessel both directly by radiation and indirectly by convection from the guard containment atmosphere. The impact of the RCCS on the guard containment atmosphere and the maximum fuel temperature has been examined as part of this study also [2].

An integral part of the transition from forced flow to natural circulation is the dynamic behavior of the turbo-machinery of the PCU. This report also describes the progress in the modeling of the different components of a PCU that will become part of the ATHENA model of the GFR plant system [3].

The following description of the ATHENA model of the GFR represents progress made during FY05. Details of the models and results of the calculations can be found in the interim reports [1,2,3].

#### **3.1.1 Reactor and Emergency Cooling System**

An ATHENA model of the reactor system has been constructed to address different parametric effects that influence the steady state and transient behavior of a 2400 MW pin core under natural circulation cooling at decay heat power levels [1]. The model consists of two power conversion system loops, an emergency heat exchanger loop with

its heat sink, and a guard containment surrounding the primary system. The two power conversion system loops consists of one and three PCU's respectively. The loop with a single PCU (600MW) is to model the breach that causes the depressurization. The other loop is a lumped representation of the remaining three PCU's. This arrangement is shown schematically in Figure 1.

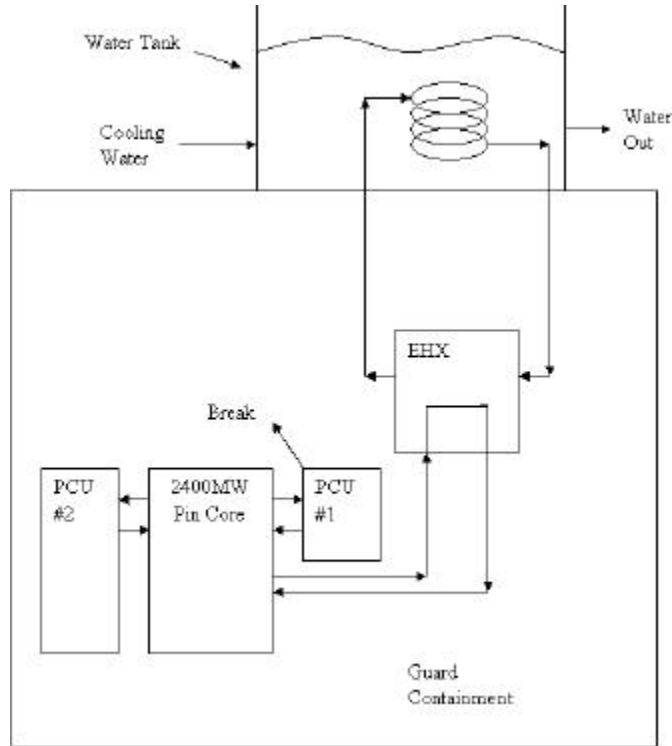


**Figure 1 – GFR System with Emergency Cooling Loop.**

### **3.1.1.1 Hydraulic Volumes and Heat Structures**

The ATHENA model of the GFR consists of two basic building blocks, hydraulic volumes representing flow channels for the helium and heat structures representing solid components with internal heat generation and/or thermal capacity and resistance. Hydraulic volumes of the primary system and the power conversion unit (PCU) are shown in Figure 2. It is seen that all the components of the power conversion unit are represented. However, at this stage the actual turbine, compressors, generator models and heat exchangers are not complete. The actual models for these components, including performance maps and inertia terms, will be added at a later date. The detail modeling of the PCU components is discussed in a later section.

Several volumes are used to represent the core and the pressure vessel. The fuel and metal components are represented as heat structures. Details of the heat structures used in the ATHENA model for convective and radiative heat transfer are shown in Figure 3.

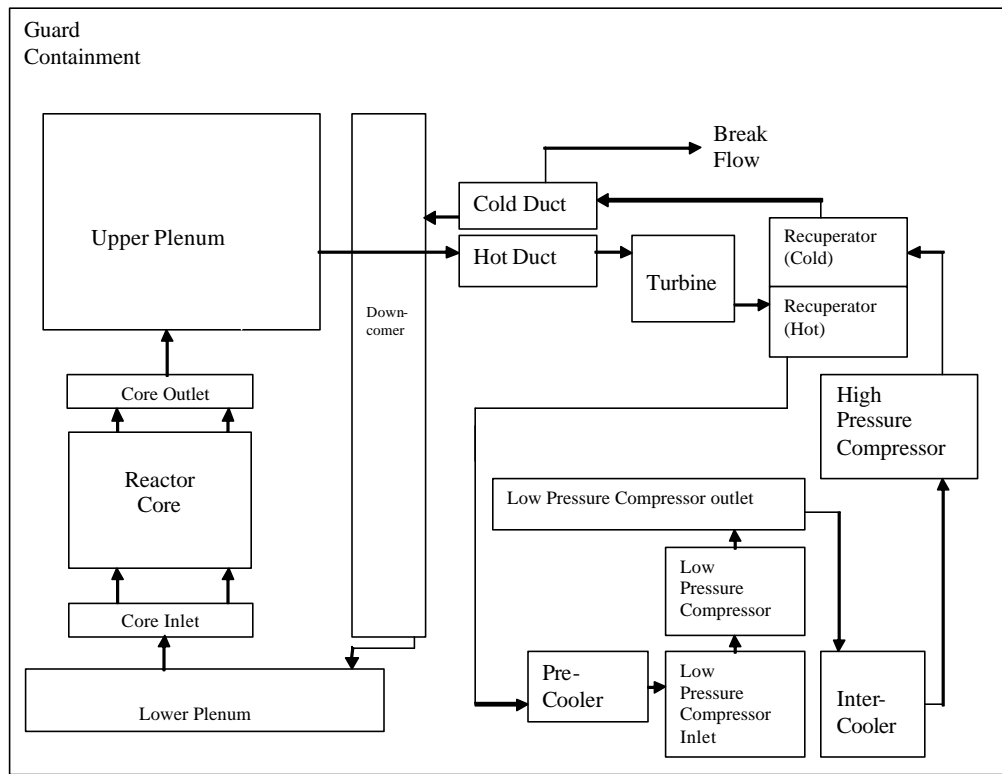


**Figure 2 – Reactor Vessel and Power Conversion Unit Volume Arrangement.**

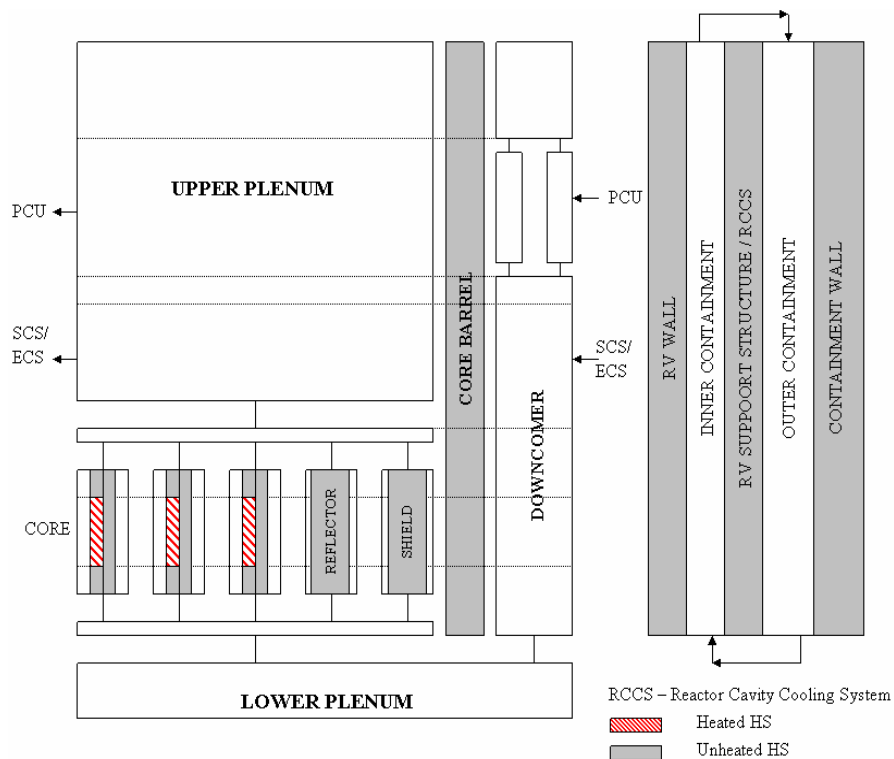


**Figure 3 – Reactor Vessel and Guard Containment Heat Structures.**

The core model consists of three radial zones and ten axial zones. The three radial zones include a hot assembly, a hot zone, and an average zone. Each of the radial zones is divided into ten axial zones. Power generation in each zone is obtained from output of the reactor physics analysis. Beyond the core there is a radial reflector, shield, core barrel, reactor pressure vessel wall and support structure, and finally the guard containment wall. It is noted that explicit heat generation is only modeled in the core volumes. Heat generation in the other volumes is of marginal importance, and these structures act only as thermal capacitors.

### 3.1.1.2 Radiative Heat Transfer

Radiative heat transfer is modeled between the heat structures [1]. Shown in Figure 4 is the conceptual arrangement of heat structures involved in the heat transfer by radiation.

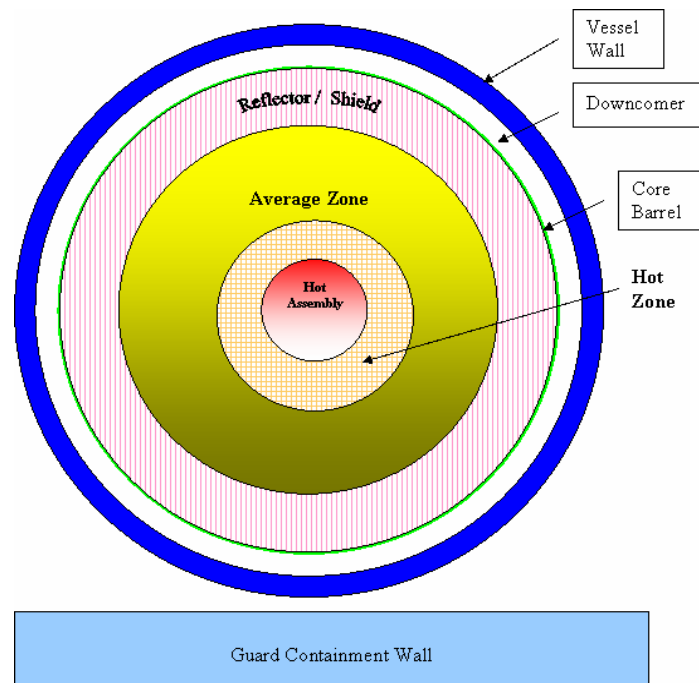


**Figure 4 – Heat Structures for Radiative Heat Transfer.**

This model allows for radial radiation heat transfer only, and couples the hot inner core parts to the cooler outer parts. Figure 4 is thus a radial section through the core and associated guard containment wall, since these are the heat structures involved in the heat transfer process. It is seen that the fuel pins radiate to the assembly cans, which in turn radiate to each other. At the outer core boundary the element cans radiate to the inner reflector surface, which radiates to the radial shield. Finally the shield radiates to the core barrel, which radiates to the reactor pressure vessel, and it finally radiates to the guard containment wall. It is assumed that the guard containment wall is kept at a constant temperature by a thermal management system embedded in the wall.

It is clear from the above discussion that the core heat transfer model has both a convective and a radiative component. Convectively, heat is removed from the core by

helium gas flowing up along the fuel pins. This mechanism is either forced or natural convection. The second heat transfer mechanism is radiation from the hotter parts of the core to the cooler parts of the core.

### 3.1.1.3 Emergency Cooling System

During natural circulation thermal energy is removed from the helium via the shutdown and emergency cooling system that is sized to handle 2% decay heat removal by natural convection in a 4x50% configuration, i.e. four separate loops of 1% power capacity. In the ATHENA model the emergency heat removal system is represented by one heat exchanger, which is sized to handle 2% of full power. Thus, once the decay heat reaches a level of 2 % of full power the emergency heat removal system should be able to handle the heat load. Details of the volume representation of the Shutdown Cooling System/Emergency Cooling System (SCS/ECS) are shown in Figure 5.

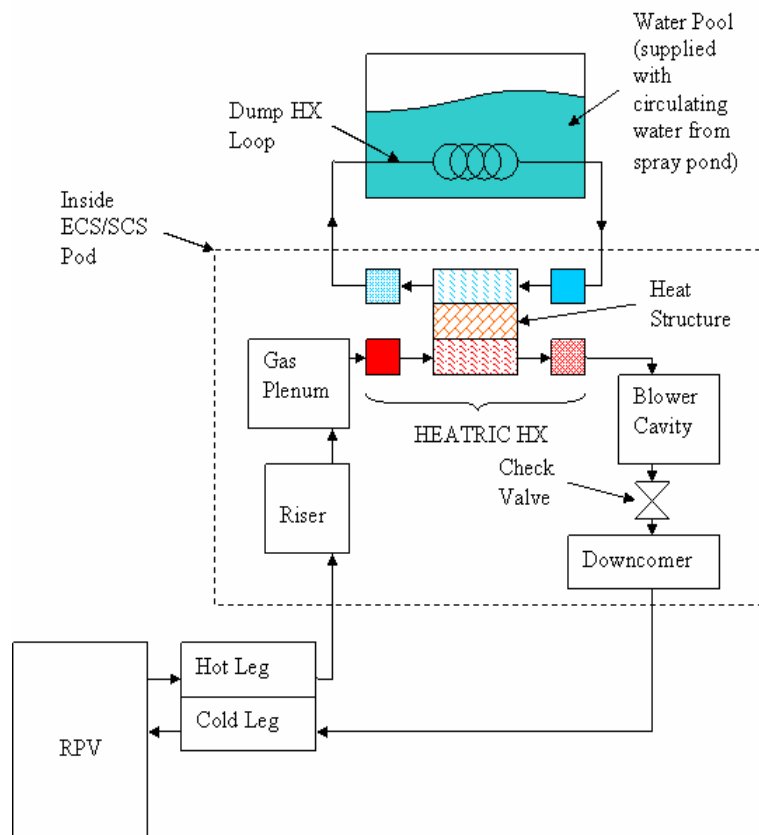


**Figure 5 – Schematic of Shutdown Cooling System/Emergency Cooling System.**

The intermediate heat exchanger is based on the HEATRIC concept. The ultimate heat sink of the SCS/ECS consists of a large water tank located outside the guard containment building. The inlet and outlet of the SCS/ECS loop is connected to the upper plenum and the downcomer of the reactor pressure vessel respectively. Although the blower volume is explicitly modeled, the actual blower rotating components are not included at this stage. The inertia of the drive motor and/or the possible availability of backup battery

power both of which could assist in forcing coolant to circulate around the primary circuit are thus not included in this analysis.

For this analysis the emergency heat exchanger system is modeled after an MIT design [1], shown in Figure 5. The HEATRIC heat exchanger consists of alternating layers of helium and pressurized water counter-current micro-channels. The HEATRIC heat exchanger is represented in the ATHENA model as a plate heat structure separating the counter-current primary and secondary fluids. In Figure 5 the heat exchanger is shown in the horizontal orientation. However initial calculations showed a period of steam void formation at the start of heat transfer to the water side. Thus, for the calculations presented in this report the flow channels were oriented vertically to ease the establishment of natural circulation flow on the water side. The secondary heat exchanger, located in the ultimate heat sink, consists of a tube and shell design with ten tube passes and one shell pass. The shell side is a water tank that represents an ultimate heat sink. The tank is assumed to be very large, and if necessary can be refilled. The arrangement of the SCS/ECS heat exchanger as it is located in a pod in the guard containment is shown in Figure 6.

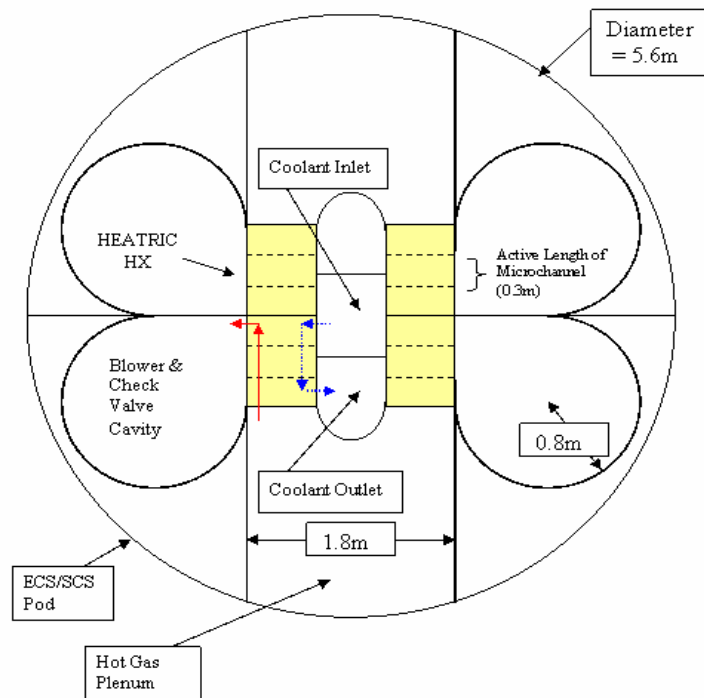


**Figure 6 – Schematic of SCS/ECS Heat exchanger Located in a Pod within the Guard Containment.**

### 3.1.2 Reactor Cavity Cooling System

The reactor cavity cooling system (RCCS) is an active system that absorbs radiant heat from the reactor vessel and removes heat from the guard containment atmosphere by natural convection. The ATHENA model of the guard containment has been modified by

adding heat structures and hydraulic volumes to represent the RCCS and the new system replaces the heat structure in the previous model that represented the reactor vessel support structure [2]. The heat structures used in the ATHENA model for convective and radiative heat transfers are shown in Figure 3. The heated heat structures (HS), i.e. the fuel pins, identified in Figure 3 is the source of energy and the unheated heat structures are other components that participate in the exchange of thermal energy by radiation. For the radiative heat transfer model implemented, the zone of influence of radiative heat transfer is assumed to be confined to the cylindrical section that coincides with the vertical extent of the fueled region of the core. As an example, though the core barrel (also, the reactor vessel wall, and the reactor vessel support structure) extends to the upper plenum, only the lower portion between the lower and upper boundaries of the fueled zone (1.347m in height) participates in radiative heat transfer. This assumption is relaxed in the current analysis to accommodate the RCCS that spans the entire height of the reactor vessel. In particular the entire core barrel now communicates radiatively with the full height of the reactor vessel wall and in turn the full height of the reactor vessel radiates to either the vessel support structure (old configuration) or the RCCS (new configuration).

The ATHENA model for the RCCS is based on a set of input developed at INL [4]. As shown in Figure 7 the RCCS is modeled with three cylindrical heat structures that are concentric with the reactor vessel.

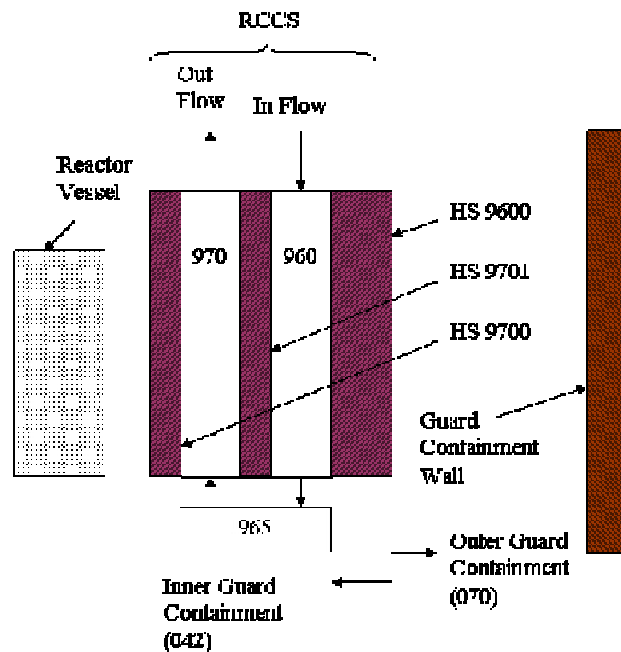


**Figure 7 - ATHENA Model of the RCCS.**

The inner wall (HS 9700), closest to the reactor vessel is followed by the interior wall (HS 9701) and the outer wall (HS 9600) respectively. The incoming (down flow) and outgoing (up flow) streams of cooling water are separated by the interior wall. The inner wall is made of stainless steel and has a wall thickness of 0.0127m. This wall is in contact with the inner guard containment volume (042) that occupies the part of the guard

containment that is within the confine of the RCCS and also includes the region above the reactor and the RCCS. The interior wall of the RCCS is modeled with a 0.01746m of low conductivity material. The outer wall of the RCCS has two layers, a 0.0127m of stainless steel and a 1m thick wall of concrete. The concrete wall is in contact with the atmosphere of the outer guard containment volume (070). The inner and outer guard containment volumes are connected at the top and bottom to facilitate internal recirculation. The wall of the 44m high guard containment is modeled with a 0.02m concrete wall.

It is assumed in the ATHENA calculations that the outside surface of the guard containment wall is kept at a constant temperature of 30°C by a thermal management system embedded in the wall. The RCCS is assumed to be cooled by 30°C water and the flow is high enough to maintain the temperature rise to less than 1 deg. C. These two boundary conditions are set to maximize the cooling of the guard containment atmosphere by the containment wall and the RCCS.

### 3.1.3 Power Conversion Unit

It has been recognized from the results of initial analyses of the depressurization accident that the coolant flow due to the coast down of the turbo-machine of the power conversion unit (PCU) is an important factor in initially cooling the core following reactor scram, and in establishing the natural circulation flow. Currently this flow is approximated by linearly reducing the flow velocity to zero in 180 seconds. A more realistic model of this flow reduction (both mass flow rate and time) is required to make more accurate estimates of the maximum fuel temperature, and ultimately the guard containment volume. In order to carry out this more realistic calculation a complete PCU model is required. The following is a discussion of the progress made in the modeling of the PCU that will become part of the ATHENA model of the GFR plant system [3].

A node diagram showing the gas volumes in a PCU is shown in Figure 8.

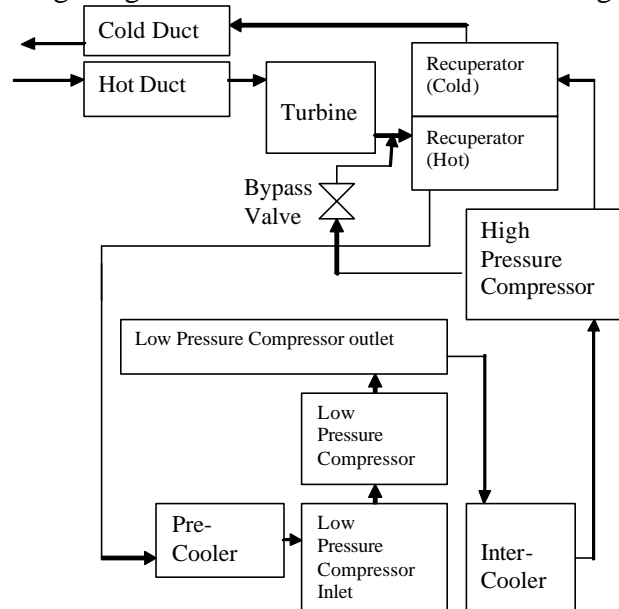


**Figure 8 – Node Diagram of Power Conversion Unit.**



The power conversion unit (PCU) of interest is a design that is being developed by General Atomics (GA) and its Russian partner for a 600 MWt Gas Turbine-Modular Helium Reactor (GT-MHR). Conceptual design of the GT-MHR was done by GA and further development is being carried out in Russian with support from the US government. A PCU has two major parts, the turbo-machine and the heat exchangers. The components of a PCU are housed in a vertical vessel that is placed near the reactor. The PCU and the reactor are connected by a short cross vessel that is made up of an inner hot duct and a concentric outer cold duct. Components of the turbo-machine, namely, the generator, turbine, low and high pressure compressors, are all on one shaft. The heat exchangers consist of recuperator, precoolers, and intercoolers. A bypass valve that connects the high and low pressure side of the PCU is used for the over-speed protection of the turbine.

Stand-alone ATHENA models of the turbine, compressors, recuperator, precoolers, and intercoolers have been prepared. In general the predicted thermal capacities of the components are within a few percent of the values shown in Table 1.

**Table 1 – Helium State Points**

Component	Inlet Conditions	Outlet Conditions	Thermal Capacity
Turbine	848 °C 7.07 MPa	508 °C 2.61 MPa	558.5 MW
Recuperator (Low Pressure)	508 °C 2.61 MPa	130.3 °C 2.58 MPa	639 MW
Precooler	130.3 °C 2.58 MPa	26.4 °C 2.55 MPa	173 MW
Low Pressure Compressor	26.4 °C 2.55 MPa	107.5 °C 4.31 MPa	132.3 MW
Intercooler	107.5 °C 4.31 MPa	26 °C 4.28 MPa	130.2 MW
High Pressure Compressor	26 °C 4.28 MPa	110.3 °C 7.24 MPa	134.5 MW
Recuperator (High Pressure)	110.3 °C 7.24 MPa	488 °C 7.16 MPa	639 MW

Since the performance data for the multi-stage turbine is not available only an approximate ATHENA model is used to represent the gas turbine. It is modeled as a single stage type 2 turbine, i.e. constant efficient stage.

As the ATHENA model of a compressor is only made available recently, in the interim approximate models are used to represent the low and high pressure compressors. The pump model is used as a surrogate for the compressor. In order to make full use of the compressor model in ATHENA knowledge of the performance characteristics of the compressors is required.

Located in the annular space between the turbine-compressors and the PCU vessel is the recuperator, the precoolers and the intercooler. The coolers are cooled by running water that transfers heat to the ultimate heat sink.

The recuperator is a vertical modular heat exchanger with plate-fin heat transfer surface and operating with countercurrent flow. The heat transfer coefficient calculated by ATHENA for a flat plate is adjusted by using the fouling factor input to achieve the desired heat transfer rate for a given flow and surface area.

The precoolers and the intercooler have similar design. They are both modular vertical heat exchangers. Each module consists of a number of straight tubes with outer fins and the tubes are arranged in a triangular array. Cooling water flows inside the tubes. A displacer rod located inside each tube enhances the heat transfer by increasing the flow velocity. Helium flows on the outside of the tubes, countercurrent to the water flow.

### **3.1.4 Results Of Analysis**

Two series of transient calculations were done to exercise the modeling of decay heat removal in a GFR during a depressurization accident. In both series of calculations the reactor was at full power (2400 MW) when a  $0.00645\text{m}^2$  ( $1.0\text{ in}^2$ ) rupture in the #1 loop (see Figure 1) of the PCU cold leg initiated the transient.

#### **3.1.4.1 Initial Results**

The first series of calculations utilizing the ATHENA model described earlier was performed to evaluate the effect of guard containment pressure on the passive mode of decay heat removal by natural circulation cooling [1]. The effect of back pressure on natural circulation cooling of the pin core was evaluated by parametrically varying the free volume of the guard containment. The nominal case (Case 1) had an assumed guard containment volume of  $27000\text{ m}^3$  and a final calculated pressure of  $0.574\text{MPa}$ . The other cases had volumes and final pressures as shown in Table 2. Only two of the four cases, namely Case 2 and 4, resulted in an end state whereby natural circulation cooling has sufficient capacity to remove decay heat generated by the 2400 MW core. A natural circulation cooling transient was considered a success or adequate if the maximum fuel temperature in the hot channel remained less than  $1600^\circ\text{C}$  throughout the transient. Results from this first series of calculations indicate that the guard containment back pressure has a dominant effect on the rate of heat removal by natural circulation, with a higher pressure leading to a higher flow rate.

The contribution of radiation heat transfer to the overall cooling of the fuel pins is demonstrated by the following tabulation (Table 3) that shows the energy balance for the upper half of the fuel pin in the hot assembly for Case 4 at the end of the calculation (24000s). In Table 3 the axial location of the mid-point of heat structures representing the top half of the active fuel is relative to the core mid-plane.

**Table 2 – Summary of Initial Results**

Case Identification	Guard Containment Free Volume (m <sup>3</sup> )	Final Containment Pressure (MPa)	Maximum Fuel Temperature (°C)
Case 1	27000 (Nominal)	0.574	Exceeded 1600
Case 2	0.5 x Nominal	0.901	1001
Case 3	1.33 x Nominal	0.472	Exceeded 1600
Case 4	0.75 x Nominal	0.675	1464

**Table 3 – Energy Balance for the Top Half of Fuel Pins in Hot Assembly**

Heat Structure Location	Loss by Radiation (W)	Loss by Convection (W)	Power Source (W)	Net Loss of Power (W)
0.15 (Node 550006)	12796	44351	56987	159.71
0.45 (Node 550007)	14102	38994	52931	165.25
0.725 (Node 550008)	11292	27168	38335	124.76
0.925 (Node 550009)	6362	14334	20629	67.159

The corresponding heat structure temperatures and the coolant temperatures are shown in Table 4. The above tabulation shows that radiation accounts for 20-30% of the power loss from the fuel pin in the hot assembly. Radiation heat transfer becomes less significant for heat structures as their distance from the hot assembly is increased. The presence of unheated heat structures inside the reactor vessel increases the heat capacity of the system and this also helps to lower the heat up of the helium gas inside the vessel.

**Table 4 – Temperatures in the Top Half of the Hot Assembly**

Heat Structure Location	Length of Node (m)	Fuel Temperature (°C)	HEX Can Temperature (°C)	Coolant Temperature (°C)
0.15 (Node 550006)	0.20205	1135	1106	1110
0.45 (Node 550007)	0.20205	1295	1270	1274
0.725 (Node 550008)	0.168381	1405	1385	1388
0.925 (Node 550009)	0.101029	1463	1446	1448

### 3.1.4.2 Results with RCCS

The second series of calculations was done with the addition of the RCCS [2]. These calculations were performed by using the same system model and the same depressurization accident as described in Section 3.1.4.1. With the modifications to the radiative heat transfer model for the core barrel, vessel wall, and vessel support structure, it becomes necessary to establish a new baseline analysis for use in comparison with the case of the RCCS. The new baseline case is similar to Case 4. The depressurization accident is initiated by a 0.00645 m<sup>2</sup> (1.0 in<sup>2</sup>) rupture in the cold leg of one of the PCUs (4 loops of 600MW each). A guard containment free volume of 20250 m<sup>3</sup> is assumed and the initial pressure and temperature of the guard containment atmosphere are one atmosphere and 30°C respectively.

Two transient cases had been run, one with and one without the RCCS. The later is the new base case. The benefits of having the RCCS are evident in the guard containment conditions. Both the pressure and temperature of the guard containment are lower in the case with RCCS (Case 5) than the case without (Case 4a, the base case) it. The trend of lower temperature however does not extend to the peak fuel temperature. Results of the two cases, at the end of a 24000s run, are summarized below.

**Table 5 – Summary of Results with RCCS**

Case Identification	Final Peak Fuel Temperature (°C)	Final Containment Pressure (MPa)	Final Containment Temperature (°C)
Case 4a (No RCCS, Base Case)	1321	0.658	82.
Case 5 (With RCCS)	1499	0.611	52.

It is noted that the maximum fuel temperature during the depressurization accident is only a few degrees from the final peak fuel temperature shown in the above table. With a lower guard containment pressure, the natural circulation flow established in the reactor is correspondingly lower in the case with RCCS. This then leads to a higher peak fuel temperature in Case 5. The result of the peak fuel temperature demonstrates that the predominant mode of decay heat removal is by convection while radiative heat transfer only serves a minor role in heat dissipation from the fuel. For the purpose of comparison, at the initial steady-state reactor power of 2400MW, the RCCS removes about 2MW of power while the emergency cooling system (ECS) removes about 20MW of power from the reactor at the end of the calculation at 24000s.

It is noted that though Case 4a is the same transient as Case 4, the new analysis has a few modifications in the inputs for the heat structures. These changes resulted in a generally lower guard containment pressure and lower temperatures (fuel and guard containment) than before.

The progression of the depressurization transient for Case 4a and Case 5 is very similar. The following sections discuss the thermal-hydraulic response of some of the more important system parameters during the transient. For each system parameter the ATHENA results for both cases are plotted together to facilitate the comparison of the two cases.

#### 3.1.4.2.1 Heat Removal Rate of the Emergency Cooling System

Plotted in Figure 9 is the rate of heat transfer into the water side of the HEATRIC heat exchanger in the emergency cooling system.

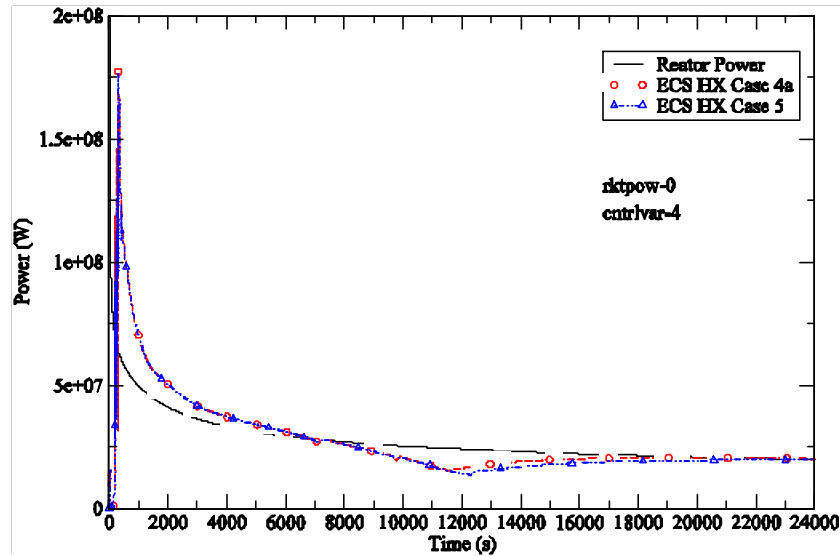


**Figure 9 – Reactor Power and Emergency Heat Exchanger Heat Removal Rate.**

The reactor power also is shown in the figure for comparison. The initial surge in the heat removal rate is due to the hydraulic transient on the water side of the heat exchanger as explained in [1]. A comparison between Figures 9, 10 and 11 shows that as the reactor pressure comes into equilibrium with the guard containment pressure, indicating an end to the depressurization phase of the transient, there is a slow migration of the heat exchanger heat removal rate towards the reactor power. This trend is indicative of the approach to a quasi-steady state where the natural circulation heat removal rate matches that of the reactor power.

#### 3.1.4.2.2 Reactor Pressure

The pressure of the reactor upper plenum is shown in Figure 10. With the initiation of the break at time zero, the current RELAP5/ATHENA model assumes a linear coast down of flow velocity from the power conversion unit (PCU) to the reactor. This is an interim scheme to simulate the behavior of a tripped PCU until a compressor/turbine model is developed for a more realistic representation of the PCU. The mean initial pressure of the PCU is less than the reactor pressure. With no rotating machinery in the current model to provide hydraulic head in the PCU, helium gas in the reactor quickly depressurizes into the PCU volumes. This results in a rapid drop in reactor pressure at time zero. The rest of

the depressurization is more gradual and is due to leakage through the break into the guard containment. For much of the depressurization transient the helium flow through the leak is choked and thus both cases have similar reactor pressure until the point at which the reactor pressure equalizes with the guard containment pressure. It is noted that the blow down takes a little longer in Case 5 than Case 4a. The reason is a lower back pressure in the latter (see Figure 11).

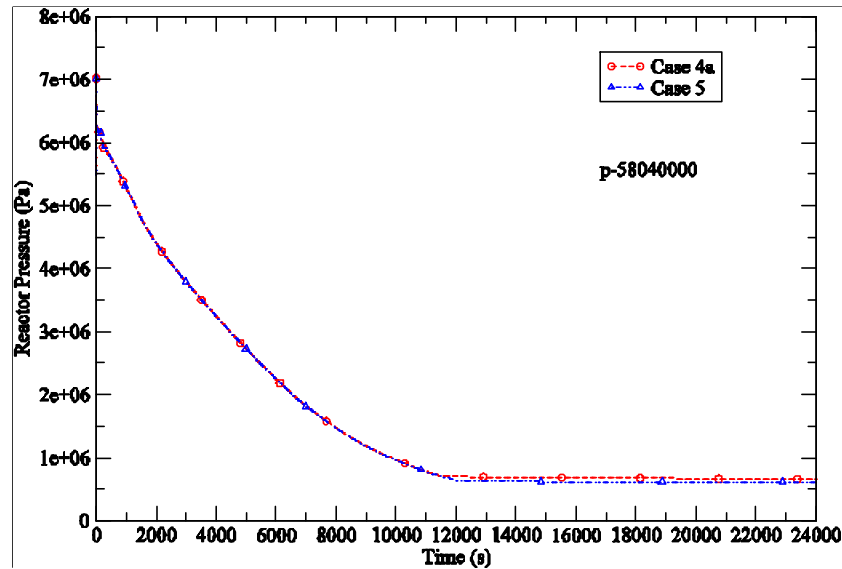


Figure 10 – Reactor Pressure in the Upper Plenum.

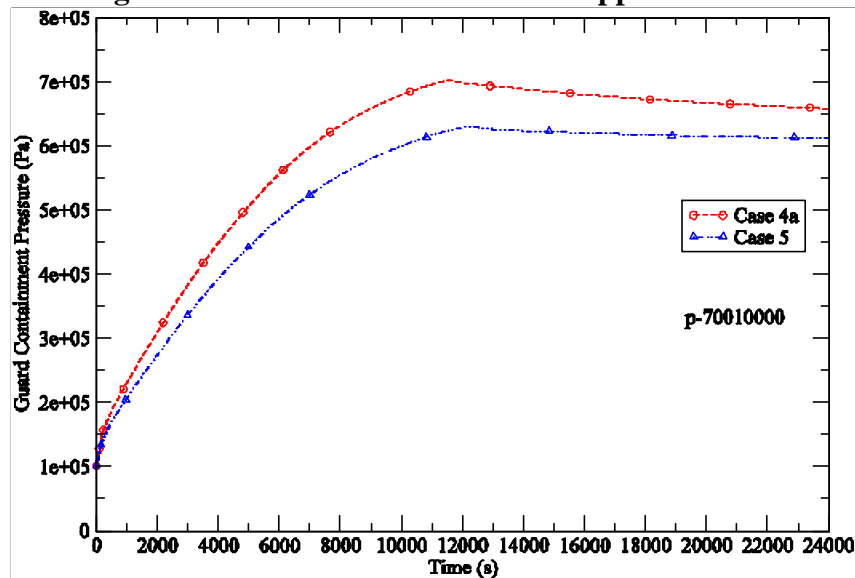


Figure 11 – Guard Containment Pressure.

#### 3.1.4.2.3 Guard Containment Pressure

There are several factors that determine the pressure build up in the guard containment after a leak in the reactor primary circuit. They are:

1. Initial state of the guard containment atmosphere, i.e. temperature, pressure, and volume.
2. Presence of heat structure to absorb sensible heat inside the guard containment.
3. Presence of active cooling device in the guard containment.
4. Through wall heat transfer to the outside.
5. Energy and mass transfer through the leak into the guard containment.

In Figure 11 the rate of pressure build up is seen to be faster for Case 4a than Case 5 and the former also has a higher containment pressure. A peak pressure is reached when the reactor and guard containment have reached the same pressure and the combined heat removal from the Emergency Cooling System, Reactor Cavity Cooling System, and heat conduction through the guard containment wall exceeds the decay power.

#### 3.1.4.2.4 Guard Containment Gas Temperature

The gas temperature of the guard containment increases rapidly after the initiation of the depressurization accident because of the relatively low heat capacity of its atmosphere. Figure 12 shows that the gas temperature is lower when the RCCS is included in the analysis. A high gas temperature is of concern not only for the environmental qualification of equipment and instruments inside the guard containment but also for the structural integrity of the support structures and the guard containment itself.

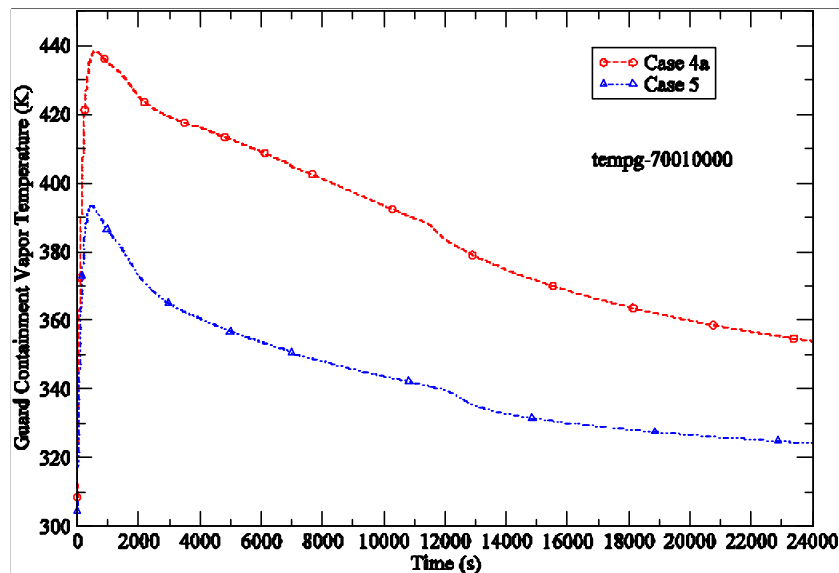


Figure 12 – Gas Temperature Inside the Guard Containment.

#### 3.1.4.2.5 Peak Fuel Temperature

Figure 13 shows the peak fuel temperature as a function of time. It is obtained from the RELAP5/ATHENA results by defining a control variable that searches for the maximum temperature for all fuel heat structures at all axial locations. It is noted that there is little deviation between the peak fuel temperatures for the two cases until about 12000s when Case 4a has finished its blow down. Before that time the two cases have the same reactor

pressure and almost the same natural circulation flow (see Figure 14). In both cases the maximum fuel temperature during the transient is within the success criterion of 1873K, with the RCCS case (Case 5) exhibiting a closer approach to the limit.

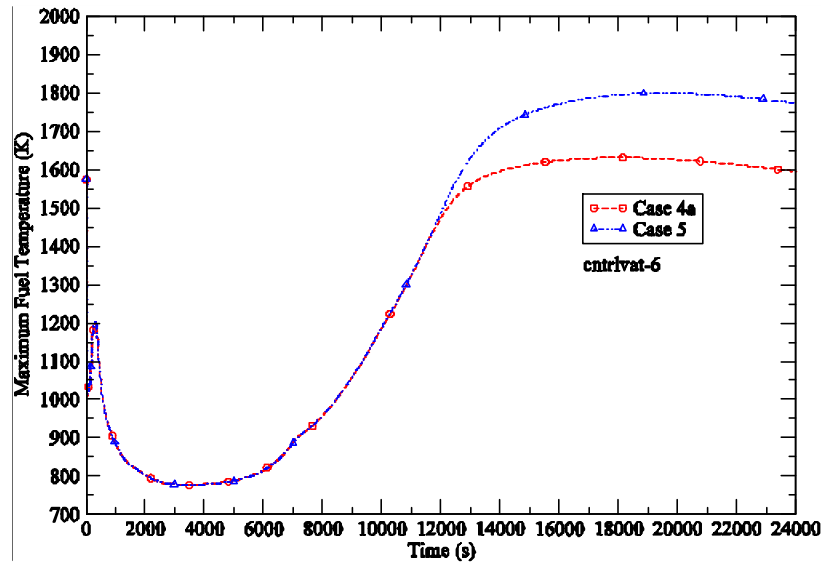


Figure 13 – Peak Fuel Temperature Core-wide.

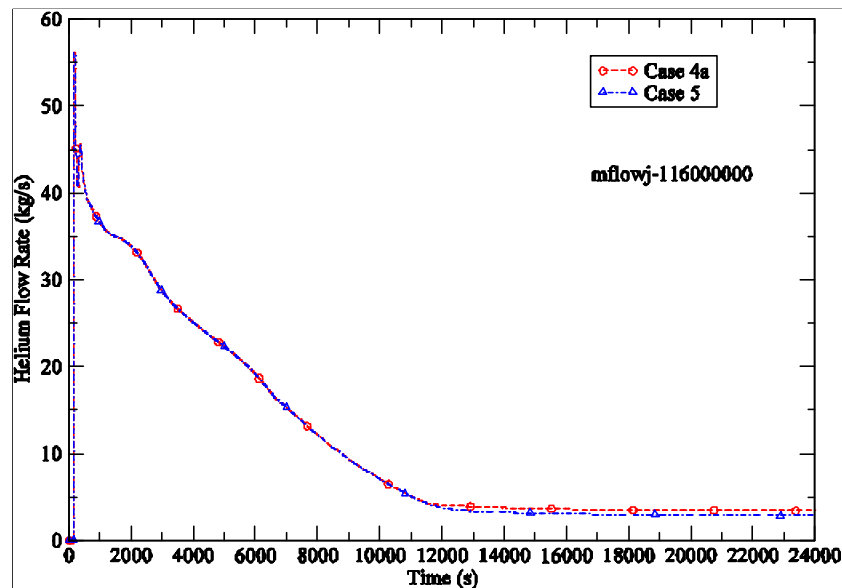


Figure 14 – Natural Circulation Flow Rate of Helium Gas.

#### 3.1.4.2.6 Helium Flow in Natural Circulation

Natural circulation flow is established when the pressure difference across the check valve in the emergency heat exchanger loop has reached a threshold value. The helium flow rate shown in Figure 14 clearly demonstrates its dependence on the reactor pressure (see Figure 10). Higher flow rates are achieved at higher pressures and that is the reason for the base case to have a higher flow rate than the RCCS case when the system pressure



has reached its quasi-steady state value. Based on economic and engineering constraints a maximum design pressure will be specified for the guard containment and that will have a direct bearing on the maximum passive heat removal rate achievable by natural circulation alone.

#### 3.1.4.2.7 Gas Temperature at Core Outlet

The gas temperature at core outlet, shown in Figure 15, generally reflects the rate of heat transfer from the core to the helium flow. The progression of the core outlet temperature thus follows the trend of the fuel temperature shown in Figure 13.

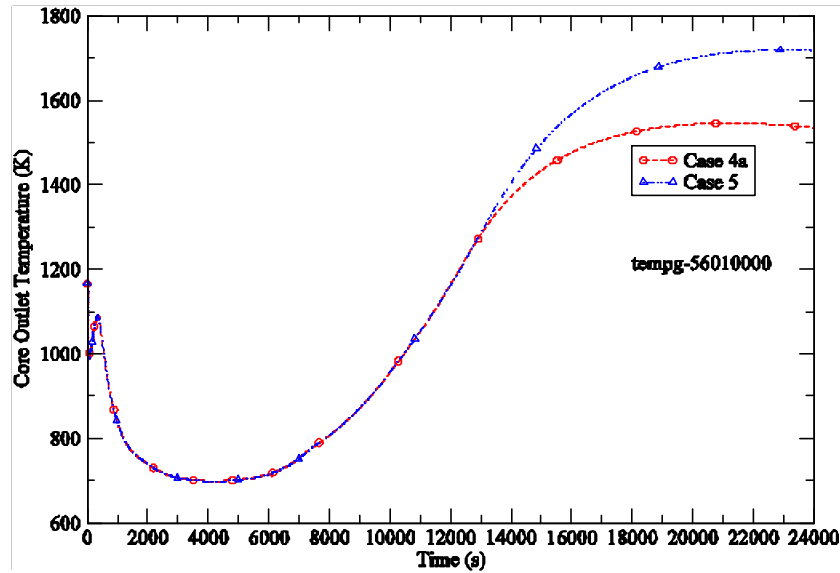
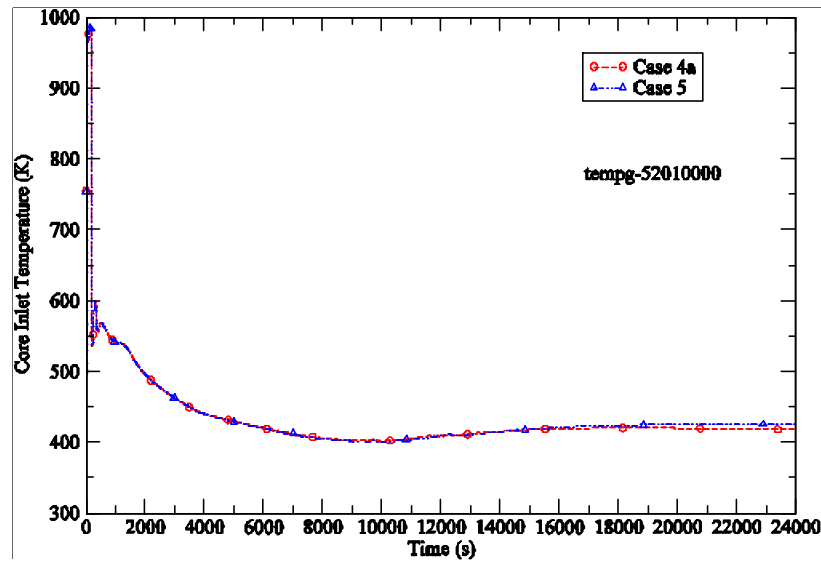


Figure 15 – Gas Temperature at Core Outlet.

#### 3.1.4.2.8 Gas Temperature at Core Inlet

The initial surge in the core inlet temperature, shown in Figure 16, is somewhat unrealistic and is due to an approximation in the current PCU model discussed earlier in relation to the reactor pressure. In general the trend of the core inlet temperature corresponds to the difference between the heat removal rate of the emergency heat exchanger and reactor power. A positive differential implies a decrease in core inlet temperature and vice versa. The core inlet temperature is very similar for both cases and the general trend follows the ECS heat exchanger heat removal rate shown in Figure 9.



**Figure 16 – Gas Temperature at Core Inlet.**

### 3.1.5 Summary and Conclusions

An ATHENA model of a 2400MW GFR has been developed for the transient analysis of decay heat removal by natural circulation cooling. The model includes the passive emergency cooling system and the reactor cavity cooling system. Two modes of decay heat removal have been considered, namely convection and thermal radiation. Progress has also been made in the modeling of the turbo-machinery and heat exchangers of the power conversion unit.

Results of calculations using the ATHENA model have highlighted the effects of the guard containment back pressure on the maximum fuel temperature. A higher pressure leads to a higher natural circulation flow and a corresponding lower fuel temperature.

Heat structures and radiative heat transfer are important phenomena in the post-accident thermal progression of the core. The effect of including these phenomena is to redistribute the radial temperature profile compared to not including them. Briefly, the hot zones (fuel) are reduced in temperature, and the cold zones (reflector, shield etc.) are increased in temperature relative to not including the above mentioned phenomena.

Results of analysis including the RCCS show that while the system is good for lowering the guard containment pressure and temperature, its presence has a negative impact on the peak fuel temperature because the lower back pressure also reduces the natural circulation flow that removes most of the decay heat by convection. While the RCCS may be beneficial for other non-LOCA type accidents its impact in a depressurization accident would require further studies to evaluate the trade-offs. The same observation applies to other active or passive means of cooling the guard containment atmosphere. One example is the heat loss through the guard containment wall. Internal flow inside the guard containment tends to be quite complex and to correctly model the loss of heat by convection to the wall would require a more detailed analysis than what is possible with a

system code. This is confirmed by the CFD analyses initiated for the guard containment atmosphere and documented in Section 3.4.

The coolant flow due to the coast down of the Turbine-Compressor-Generator (TCG) unit is an important factor in initially cooling the core following a reactor scram and in establishing the natural circulation flow. Currently this flow is approximated by linearly reducing the flow velocity to zero in 180 seconds. A more realistic model of this flow reduction (both mass flow rate and time) is required to make more accurate estimates of the maximum fuel temperature, and ultimately the guard containment volume and pressure. In order to carry out this more realistic calculation a complete Turbine Compressor model is required and the modeling effort is in progress. This model will require the appropriate performance maps, inertia of the rotating parts, and some estimate of the internal friction of the blades rotating in the working fluid.

With a 100W/cc core power density the sensitivity of maximum fuel temperature to core power distribution has pointed to the need of a more uniform core power distribution radially and axially. Fuel pin design (pellet size, gap and clad thickness) also has a significant impact on the fuel temperature response in a depressurization accident.

#### References

- [1] Cheng, L., Ludewig, H. and Jo, J., "Passive Decay Heat Removal for a 2400 MW Pin Core by Natural Circulation," BNL report submitted to the DOE GEN-IV Program, January 2005.
- [2] Cheng, L. and Ludewig, H., "Analysis Of Depressurization Accident for a 2400 MW Gas Cooled Reactor – Effects of the Reactor Cavity Cooling System," BNL report submitted to the DOE GEN-IV Program, April 15 2005.
- [3] Cheng, L. and Ludewig, H., "Modeling of the Power Conversion Unit (PCU)," BNL report submitted to the DOE GEN-IV Program, July 15 2005.
- [4] Davis, C., Personal communication with L. Cheng (Electronic files related to major improvements made to the RELAP5-3D/ATHENA computer code for analysis of the GFR as part of an annual report (2004) for an INL LDRD), April 7, 2005.

### ***3.2 Heated Region Flow Starvation***

Recent studies [1] have revealed that during off-normal conditions (e.g., Loss Of Coolant Accident) flow instability can occur within the hot channels resulting in choked flow. The choked flow differs from the traditional definition of choked flow, as it is the result of a phenomenon called "laminarization". Laminarization is caused when the coolant velocity is theoretically in the turbulent regime, but the heat transfer properties are indicative of the coolant velocity being in the laminar regime [2]. It is important to examine the potential for laminarization in the GFR design because, as a first approximation, the helium's operating temperatures appear conducive to the phenomenon's occurrence. That is, the high heating rate of the GFR core results in the helium's elevated temperatures, acceleration, and viscosity; ideal conditions for the onset of laminarization. In this paper, we propose to study the effects of laminarization by keeping the helium mass flow rate constant, while increasing the temperature. With this

approach we hope to identify which of the four variables (Reynold's number, heat flux, buoyancy parameter, and acceleration parameter) are most influential in creating laminarization and, thus, hot channel instability.

A RELAP5-3D/ATHENA model of a prototypical GFR design was created using the most current design information. Variables from the RELAP5-3D analyses were used to calculate Reynolds number, buoyancy parameter, and acceleration parameter to determine the presence of laminarization. For an arbitrary cross-section, the acceleration parameter ( $K_v$ ) can be defined [3] as:

$$K_v = \frac{4(P_h/P_w)\Phi^*}{Re_{Dh}} \quad (1)$$

The RELAP5-3D/ATHENA model of the GFR uses uranium-carbide fuel that is dispersed in a silicon-carbide matrix, as shown in Figure 1. This geometry of the fuel assembly features the coolant channels as cylindrical holes in the block fuel, which allows the ratio of the heated to wetted perimeter ( $P_h/P_w$ ) to be equal to 1.

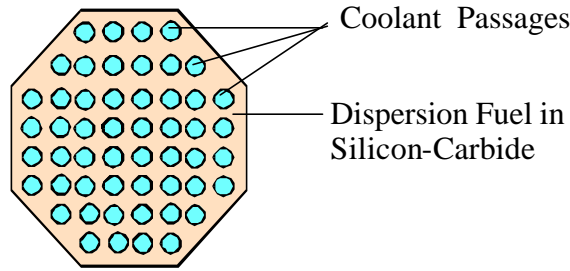


Fig. 1. GFR block-type fuel with coolant passages

Therefore,

$$K_v = \frac{4 \Phi^*}{Re_{Dh}} \quad (2)$$

Moretti and Kays [4] suggested that for  $K_v$  values less than approximately  $3 \times 10^{-6}$ , the flow will remain turbulent. However, higher values of  $K_v$  are believed to laminarize the flow, which causes a substantial reduction in the heat transfer coefficients.

For non-circular ducts, the resulting acceleration threshold parameter can be defined [3] as:

$$Ac = \frac{K_v d_M \left( \frac{\gamma_w}{\gamma_b} \right) \left( \frac{\gamma_w}{\gamma_b} \right)^{\frac{1}{2}}}{\left( \frac{f_t}{2} \right)^{\frac{3}{2}} (Pr)^{0.4}} \quad (3)$$

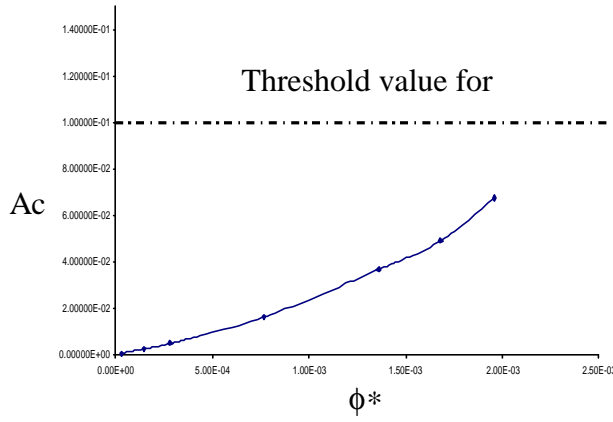


Fig. 2. Acceleration parameter as a function of non-dimensional heat flux

The value obtained for the acceleration parameter (Figure 2) was below the threshold for significance, but would certainly be of importance for higher powers. This study was limited to 1000 MW in order not to exceed the fuel temperature limit. At the highest power level, the ratio of wall to bulk temperatures was found to be equal to 1.55, and according to Gnielinski [8], would cause an 18% reduction in the heat transfer coefficient.

Also important is the influence of heat flux, the buoyancy parameter, and the Reynolds number on hot channel flow. An approximate analysis for the onset of buoyancy in terms of a buoyancy parameter was developed by Jackson [5].

$$Bo = \frac{Gr^* d_M (\rho_w / \rho_B) (\rho_w / \rho_B)^{0.5}}{\{2 Nu_{DH} Re_{DH}^3 (f_t / 2)^{1.5} Pr^{0.4}\}} \quad (4)$$

Applying the Dittus-Boelter correlation [6] for gases and the Blasius friction correlation, Jackson [7] reduced the buoyancy parameter to:

$$Bo^* = \frac{Gr^*}{Re_{DH}^{3.425} Pr^{0.8}} \geq 6 \times 10^{-7} \quad (5)$$

for fully developed flows in circular channels.

The power of the developed RELAP5-3D model was varied from 10 MW to 1000 MW with constant inlet temperature and with constant mass flow rate of 490°C and 332 kg/s, respectively (these values correspond to the normal operating condition). The value obtained for the buoyancy parameter was also well below the threshold criteria, indicating no significance of this phenomenon on the heat transfer coefficient. Thus, for the cases evaluated there is no apparent effect due to laminarization. The potential for laminarization at reduced flow will be investigated in the future.

## References

1. P. HEJZLAR, W. C. WILLIAMS, M. J. DRISCOLL, "Hot Channel Flow Starvation of Helium Cooled GFRs in Laminar Natural Convection," *American Nuclear Society Transactions*, **91**, pp. 202-204 (2004).
2. C. A. BANKSTON, "The Transition from Turbulent to Laminar Gas Flow in a Heated Pipe," *International Journal of Heat and Mass Transfer*, **92**, pp. 569-579 (1970).
3. D. M. MCELIGOT, J. D. JACKSON, "Deterioration Criteria for Convective Heat

- Transfer in Gas Flow through Non-Circular Ducts,” *Nuclear Engineering Design*, **232**, pp. 327-333 (2000).
4. P. M. MORETTI, W. M. KAYS, “Heat Transfer to a Turbulent Boundary Layer with Varying Free-Stream Velocity and Varying Surface Temperature-an Experimental Study,” *International Journal of Heat and Mass Transfer*, **8**, pp. 1187-1202 (1965).
  5. D. P. MIKIELEWICZ, A. M. SHEHATA, J. D. JACKSON, D. M. MCELIGOT, “Temperature, Velocity and Mean Turbulence Structure in Strongly-Heated Internal Gas Flows. Comparison of Numerical Predictions with Data,” *International Journal of Heat and Mass Transfer*, **45**, pp. 4333-4352 (2002).
  6. F. W. DITTUS, L. M. K. BOELTER, “Heat Transfer in Automobile Radiators of the Turbulent type,” *Publication in Engineering University of California Berkeley*, **2**, pp. 443-461 (1930).
  7. J. D. JACKSON, M. A. COTTON, “Studies of Mixed Convection in Vertical Tubes,” *International Journal of Heat and Fluid Flow*, **10**, pp. 2-15 (1989).
  8. V. GNIELINSKI, “New Equations for Heat and Mass Transfer in Turbulent Pipe and Channel Flow,” *American Institute of Chemical Engineers*, **16**, pp. 359-367 (1976).

### **3.3 Large GFR Core Subassembly Design**

The current analysis has focused on the evaluation of low-pressure drop, pin-core designs with favorable passive cooling properties. Initial evaluation of the passive cooling safety case for the GFR during depressurized decay heat removal accidents with concurrent loss of electric power have resulted in requirements for a reduction of core power density to the 100 w/cc level and a low core pressure drop of 0.5 bars. Additional design constraints and the implementation of their constraints are evaluated in this study to enhance and passive cooling properties of the reactor.

Passive cooling is made easier by a flat radial distribution of the decay heat. One goal of this study was to evaluate the radial power distribution and determine to what extent it can be flattened, since the decay heat is nearly proportional to the fission power at shutdown. In line with this investigation of the radial power profile, an assessment was also made of the control rod configuration. The layout provided a large number of control rod locations with a fixed area provided for control rods. The number of control rods was consistent with other fast reactor designs. The adequacy of the available control rod locations was evaluated. Future studies will be needed to optimize the control rod designs and evaluate the shutdown system.

The case for low pressure drop core can be improved by the minimization of pressure drop sources such as the number of required fuel spacers in the subassembly design and by the details of the fuel pin design. The fuel pin design is determined by a number of neutronic, thermal-hydraulic (gas dynamics) and fuel performance considerations. For the purposes of this study, the starting point is the fuel pin design established by the CEA-ANL/US I-NERI collaboration project for the selected 2400 MWt large reactor option. Structural mechanics factors are now included in the design assessment. In particular, thermal bowing establishes a bound on the minimum of fuel pin spacers required in each fuel subassembly to prevent the local flow channel restrictions and pin-to-pin mechanical interaction. There are also fabrication limitations on the maximum length of SiC fuel pin cladding that can be manufactured. This geometric limitation

affects the minimum ceramic clad thickness that can be produced. This ties into the fuel pin heat transfer and temperature thresholds. All these additional design factors were included in the current iteration on the subassembly design to produce a lower core pressure drop. A more detailed definition of the fuel pin/subassembly design is proposed here to meet these limitations.

This subassembly design was then evaluated under low pressure natural convection conditions to assess its acceptability for the decay heat removal accidents. A number of integrated decay heat removal (DHR) loop plus core calculations were performed to scope the thermal-hydraulic response of the subassembly design to the accidents of interest. It is evident that there is a large sensitivity to the guard containment back pressure for these designs. The implication of this conclusion and possible design modifications to reduce this sensitivity will be explored under the auspices of the International GENIV GFR collaborative R&D plan.

### **3.3.1 Core Neutronics Design**

#### **3.3.1.1 Reference Case**

The reference design is a 2400 MWt pancake ( $H/D \sim 0.28$ ) core. The conversion ratio was approximately 1.0 for the three-batch scatter loading with an average 10% discharge burnup. The equilibrium-recycle fuel cycle was analyzed. Since the conversion ratio was maintained at unity, all the TRU is supplied from recycled fuel. The makeup uranium was depleted uranium. The core consists of 366 fuel (271 fuel pins) assemblies, 54 fuel assemblies (234 fuel pins) with a central control rod, and 7 fuel assemblies (234 fuel pins) with a central shutdown rod. Figure 2.1 shows the reactor layout for the reference design.

The assembly design included both fuel and control assemblies as indicated above. The fuel pins in all assemblies are the same design. The control assemblies have a centrally located control tube which replaces 37 of the fuel pins. The details of the reference assembly design are provided in Table 2.1.

The reference fuel cycle is a scatter-load 3-batch core with recycle. The TRU enrichment (TRU/HM) was adjusted to achieve the targeted cycle length. The goal of this study was to flatten the radial power distribution relative to the reference loading. Fuel loading options including enrichment splitting, fuel shuffling were considered. An annular core design was evaluated with and without enrichment splitting. The power distribution of a 600 MWt design is provided for comparison.

The conversion ratio and average discharge burnup remained fixed for the different design variants. The fuel pin diameter was adjusted to maintain a conversion ratio equal to unity. Variations in pin diameter change the fuel loading and average discharge burnup. The cycle length was adjusted to compensate and maintain the average discharge burnup at 10%. None of the designs required significant changes to maintain these parameters.

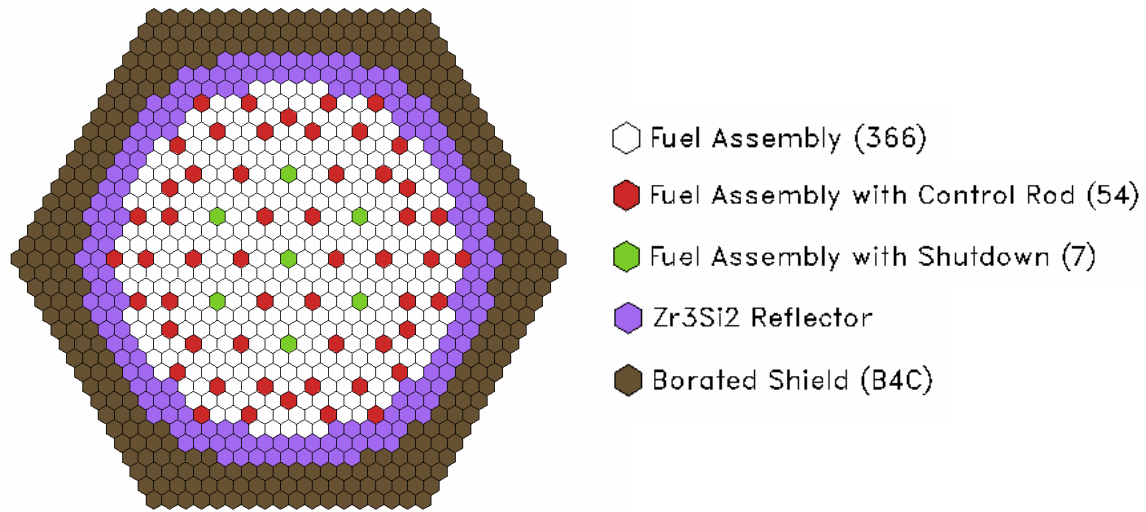


Figure 2.1. Reference Reactor Layout.

Table 2.1. Equilibrium TRU Breakeven Gas-Cooled Fast Reactor Designs.

Assembly Type	Fuel	Control	Reflector	Shield
Assembly Pitch (mm)	222	222	222	222
Assembly Flat-to-Flat (mm)	215	215	215	215
Duct Thickness (mm)	3.7	3.7	3.7	3.7
Duct Material	SiC	SiC	Zr <sub>3</sub> Si <sub>2</sub>	W
Pins	271	234	19	19
Pin Diameter (mm)	9.57	9.57	40.1	40.1
Clad Thickness (mm)	1.00	1.00	N/A	0.019
Clad Material	SiC	SiC	N/A	W
Pellet Outer Diameter (mm)	7.37	7.37	N/A	38.9
Pellet Inner Diameter (mm)	3.02	3.02	N/A	N/A
Pellet Material	(U,TRU)C	(U,TRU)C	Zr <sub>3</sub> Si <sub>2</sub>	B <sub>4</sub> C
Control Rod Outer Diameter (mm)	N/A	80.5	N/A	N/A
Control Rod Cladding Thickness (mm)	N/A	1	N/A	N/A
B <sub>4</sub> C Diameter (mm)	N/A	78.5	N/A	N/A

### 3.3.1.2 Fuel Cycle and Neutronics Modeling

Full-core, equilibrium-cycle calculations were performed using the REBUS-3 fuel cycle analysis code [2.1]. An enrichment search was performed to determine the TRU enrichment required to achieve an end of equilibrium cycle (EOEC) unpoisoned  $k_{\text{eff}}=1.0$ . An external cycle time of three years and 0.1% losses of the actinides were assumed.

Region-dependent 33-group cross sections were generated with the MC<sup>2</sup>-2 code [2.2] based on ENDF/B-V nuclear data. Beginning of cycle material compositions and temperatures from the reference design were used to generate the cross section library. The flux distributions were obtained using the nodal diffusion theory option of the DIF3D code [2.3].



A number of reactivity parameters were calculated by using the beginning of equilibrium cycle (BOEC) and EOEC number densities from the REBUS-3 calculations, generating individual finite-difference DIF3D cases, and new cross section sets using MC<sup>2</sup>-2 for the reference conditions and the perturbed conditions. The values were calculated by eigenvalue difference. This was done with the exception of the axial and radial expansion calculations, where the unperturbed BOEC or EOEC cross section library was used. The delayed neutron fraction and prompt neutron lifetime were calculated at the BOEC and EOEC with VARI3D [2.4] using the real and adjoint fluxes calculated with DIF3D for the unperturbed conditions.

The reactivity effect of a depressurization accident was evaluated. The coolant pressure was assumed to fall instantaneously to atmospheric pressure throughout the system. New coolant number density was calculated at one atmosphere using the ideal gas law. The reactivity effect of instantaneous depressurization was evaluated at BOEC and EOEC.

For the expansion cases, the core volume is increased 5% by either radial or axial expansion. The number densities, except for the coolant, were reduced to conserve mass. The coolant number densities remained constant.

### **3.3.1.3 Radial Power Distribution**

The primary goal was to estimate the minimum radial assembly peaking factor. The primary motivation for flattening the power distribution is passive cooling after shutdown. The decay heat is roughly proportional to the power at shutdown, but other factors such as burnup, TRU enrichment, and isotopics have significant impacts on the actual decay heat production as a function of time after shutdown. These secondary effects would need to be evaluated in order to accurately estimate the assembly power sharing after shutdown.

There are a large number of options for flattening the radial power distribution. A number of these options were explored. The design variants were not completely optimized, but significant further reductions in the peaking factor are not likely. Each option was considered independently. Power redistribution limited the ability to flatten the power distribution. Shorter cycle lengths would limit this effect, but were not analyzed. The power distribution map is a color-coded sixth core map. The peak to average assembly power density for each assembly is provided with colors split into seven color-coded groups: >1.4 in red; >1.2 in orange; >1.05 in gold; >0.95 in yellow; >0.8 in light green; >0.4 in sky blue; <0.4 in blue; and black for the non-fuel assemblies. The fuel assemblies are normalized to the average power density in the fueled portion of the assembly. This corrects for the central control assembly in the control and shutdown assemblies.

#### **3.3.1.3.1 Uniform Initial Enrichment**

The initial case evaluated was for the reference design. This design has a uniform TRU enrichment and a scatter loading pattern. Assembly by assembly modeling would be too time consuming at this stage of design. The core model has radial and axial depletion zones with homogeneous compositions. This results in each assembly in a zone having

the same composition, which includes equal fractions of fresh, once-burned, and twice-burned fuel. Therefore, differences in power sharing within a zone resulting from depletion are not modeled, but the conversion ratio of unity and the fast spectrum will limit the impact of this modeling approximation.

Figures 2.2 to 2.4 show the radial power distribution for BOEC, MOEC, and EOEC, respectively. The results show a large peak to average power of 1.74 at BOEC. There is very little power redistribution over the cycle with the peak to average power being 1.62 at EOEC with the peak still located at the center.

#### ***3.3.1.3.2 Out to In Fuel Shuffle***

The first methodology used to reduce the power peaking was to evaluate an out-to-in fuel shuffle. The number of fuel batches was increased from three to four and the central shutdown assembly was unfueled to make an integer number of fuel assemblies in each batch and to reduce the central peaking factor.

Figures 2.5 to 2.7 show the radial power distribution for BOEC, MOEC, and EOEC, respectively. The results show a large peak to average power of 1.57 at BOEC. There is very little power redistribution over the cycle with the peak to average power being 1.47 at EOEC with the peak still located near the center. The conversion ratio of unity leads to very little change in reactivity as the fuel assemblies are depleted. Therefore, fuel shuffling appears to have limited ability to flatten the profile for this system.

#### ***3.3.1.3.3 Non-Uniform Initial Enrichment (Flat BOEC)***

A split-batch fuel loading strategy was evaluated with four different initial enrichments in each batch. The initial enrichment and number of assemblies in each split batch were adjusted to minimize the BOEC peak to average assembly power. Initially, there was no limit on the TRU enrichment, but the conversion ratio was maintained at near unity.

Figures 2.8 to 2.10 show the radial power distribution for BOEC, MOEC, and EOEC, respectively. The results show a large reduction in the peak to average power. At BOEC, the peak to average power was reduced to 1.06. Unfortunately, there is significant power redistribution over the cycle with the peak to average power increasing to 1.25 at EOEC. The power redistributes because the higher enriched assemblies near the periphery are burning TRU, which lowers their reactivity over their lifetime, while the lower enriched assemblies near the center are breeding TRU and increasing in reactivity over their lifetime. The net effect of this TRU burning and breeding is a core that remains a TRU breakeven core, but the power as well as the TRU redistributes from the high-enriched assemblies near the periphery to the low enriched assemblies near the center.

The results are not fully optimized, but show that even if a perfectly uniform power distribution were achieved at BOEC, the power would quickly shift towards the center. By MOEC, the peak has increased to 1.17 from 1.06 at BOEC. This suggests that even a reduction in cycle length by one half would only reduce the peak to approximately 1.1 in an idealized situation.

#### ***3.3.1.3.4 Non-Uniform Initial Enrichment (No TRU limit)***

A split-batch fuel loading strategy was evaluated with five different initial enrichments in each batch. The previous section looked at minimizing the BOEC peak to average assembly power, while this analysis attempted to minimize this parameter for the entire cycle by peaking the power near the periphery of the core and allowing the power to redistribute towards the center of the core. The TRU enrichment is still not limited and the conversion ratio was maintained at near unity.

Figures 2.11 to 2.13 show the radial power distribution for BOEC, MOEC, and EOEC, respectively. The results show a small reduction in the peak to average power relative to the previous case. At BOEC, the peak to average power was 1.15 that is higher than the previous case. There is significant power redistribution over the cycle with the peak to average power decreasing to 1.08 at MOEC and then increasing to 1.18 at EOEC. The maximum peak to average power is 1.18, which is an improvement over the previous case. This is near the limit for this cycle length because the peak of 1.15 near the periphery at BOEC is nearly equal to the peak of 1.18 near the center at EOEC. Any further shifts of power from the center at EOEC to the periphery at the BOEC will simply shift the location and time of the maximum assembly power without reducing the magnitude. The maximum enrichment is 25 w/o TRU/HM, which exceeds the imposed limit of 20%.

#### ***3.3.1.3.5 Non-Uniform Initial Enrichment***

A split-batch fuel loading strategy was evaluated with five different initial enrichments in each batch. The previous section imposed no limit on the maximum TRU enrichment. For this section, the TRU enrichment was limited to 20% TRU/HM and the conversion ratio was maintained at near unity.

Figures 2.14 to 2.16 show the radial power distribution for BOEC, MOEC, and EOEC, respectively. The results show a small increase in the peak to average power relative to the previous case. At BOEC, the peak to average power was 1.10 that is slightly lower than the previous case because the 20% limit prevents pulling the power toward the periphery as effectively as the higher enrichment of the previous case. There is significant power redistribution over the cycle with the peak to average power increasing to 1.17 at MOEC and further increasing to 1.25 at EOEC. The maximum peak to average power is 1.25, which is higher than the previous case.

#### ***3.3.1.3.6 Annular Core – Uniform Enrichment***

Since the high power assemblies are located in the center, an annular core that removes these assemblies would reduce the radial power peaking. The 37 centrally located assemblies had the fuel removed and were replaced with reflector material. To maintain similar power density and core height, 36 reflector assemblies were replaced with fuel assemblies. This design was evaluated for a uniform TRU enrichment with a conversion ratio of unity.

Figures 2.17 to 2.19 show the radial power distribution for BOEC, MOEC, and EOEC, respectively. The annular core shows a large reduction in the peak to average power

relative to the reference design with uniform enrichment. At BOEC, the peak to average power was 1.30, which is significantly lower than the 1.74 value for the reference design. There is very little power redistribution over the cycle with the peak to average power decreasing slightly to 1.28 at EOEC. The advantage of the annular core is that without batch splitting, the power distribution improves significantly and there is very little power redistribution over the cycle. The annular core will have a larger core diameter.

#### ***3.3.1.3.7 Annular Core – Non-Uniform Enrichment***

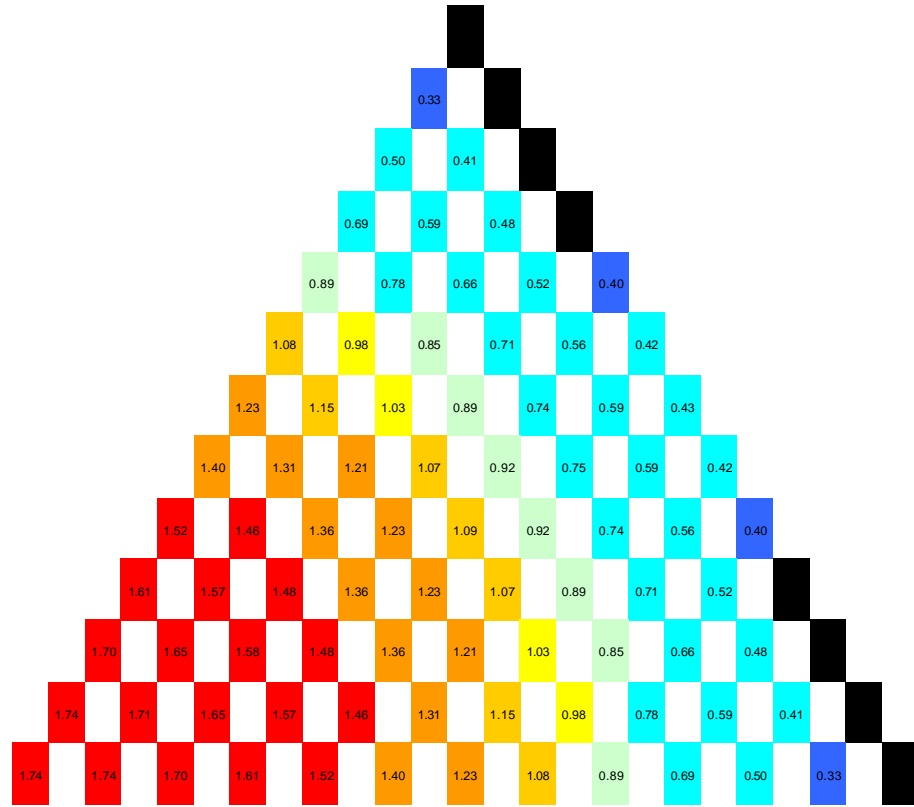
The power distribution can be improved further by using enrichment splitting. The annular core was evaluated for a split-batch fuel loading strategy with four different initial enrichments limited to 20% TRU/HM.

Figures 2.20 to 2.22 show the radial power distribution for BOEC, MOEC, and EOEC, respectively. The enrichment splitting shows a significant improvement over the previous case. At BOEC, the peak to average power was 1.19, which is significantly lower than the 1.30 value for the uniform enrichment case. Even for this enrichment splitting case, there is very little power redistribution over the cycle in the annular core. The maximum peak to average power is 1.19, which is lower than any other case. Despite having the lower peaking factor, the reference core layout was maintained and the annular core is a secondary option.

#### ***3.3.1.3.8 600 MWt Core***

Previous analysis had looked at a variety of design options, including small cores such as the 600MWt design included here. This design was for a uniform-enrichment scatter-loaded core. This design did not include fuel in the control assemblies.

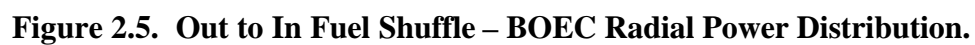
Figures 2.23 to 2.25 show the radial power distribution for BOEC, MOEC, and EOEC, respectively. The results show a much smaller peak to average power of 1.22 for the small core. The large leakage flattens the power distribution for the small core. The large core diameter of the 2400 MWt core and poor (relative to breeding blankets) reflector results in a significant peaking of the radial power distribution. The minimum peaking factor achieved with the split-enrichment fuel loading was only slightly lower than that in the 600 MWt core with a uniform enrichment. This shows that it is simpler to produce a more uniform radial power distribution in the small core.

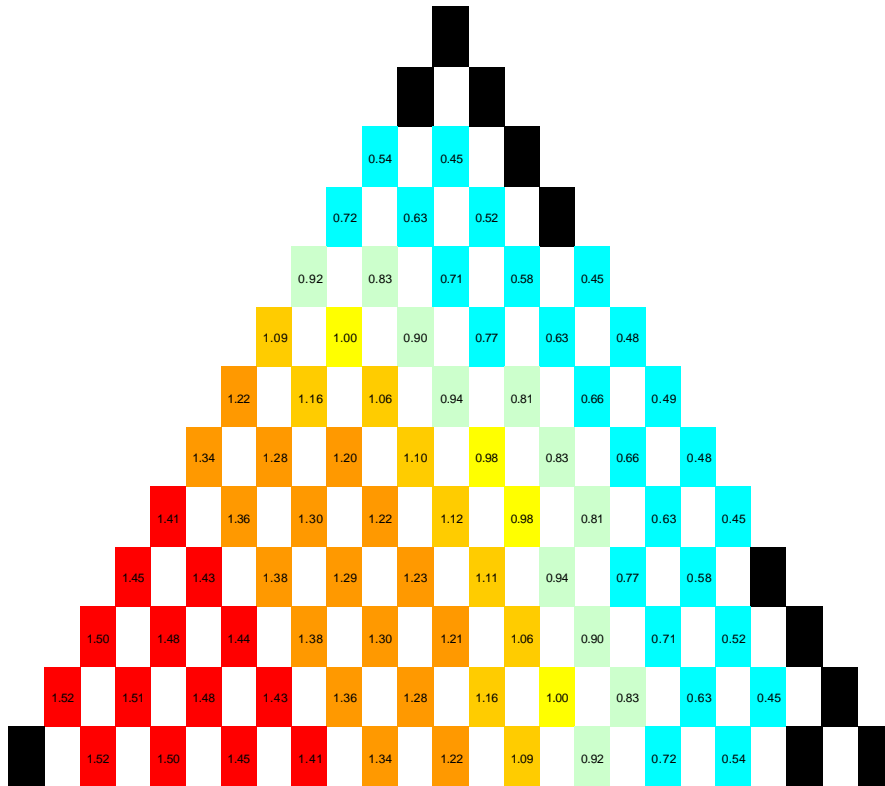


**Figure 2.2. Uniform Initial Enrichment – BOEC Radial Power Distribution.**

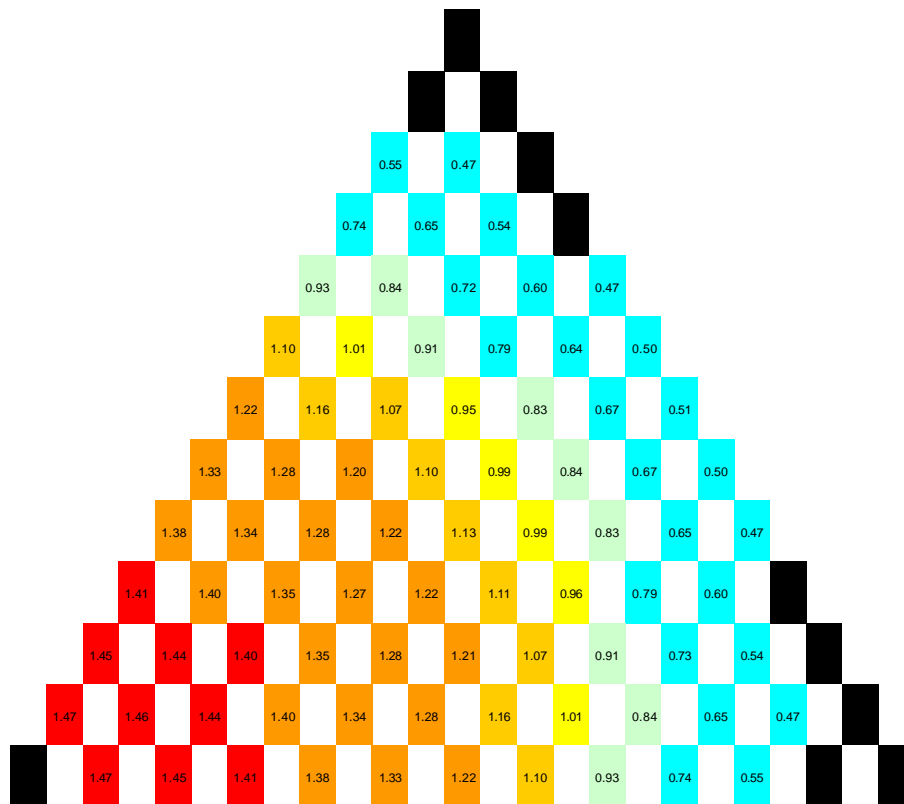


**Figure 2.3. Uniform Initial Enrichment – MOEC Radial Power Distribution.**

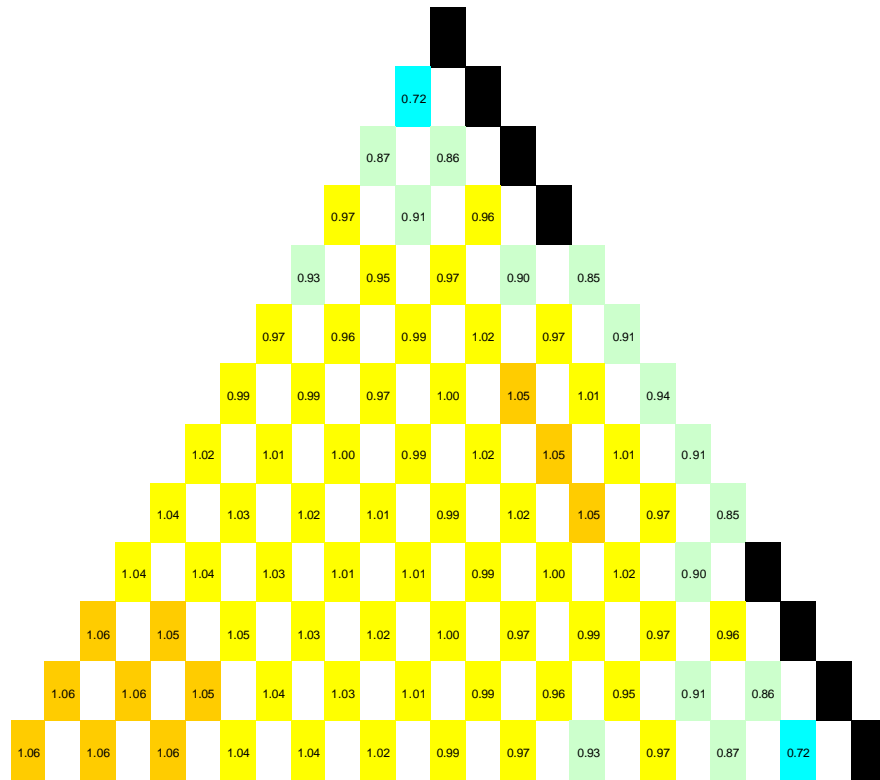




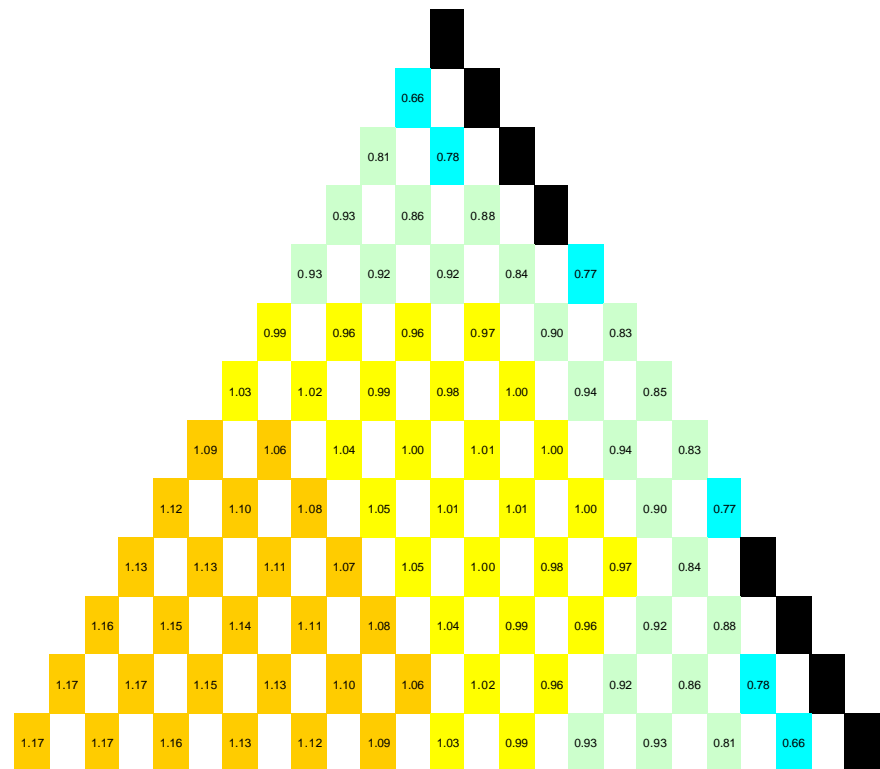
**Figure 2.6. Out to In Fuel Shuffle – MOEC Radial Power Distribution.**



**Figure 2.7. Out to In Fuel Shuffle – EOEC Radial Power Distribution.**

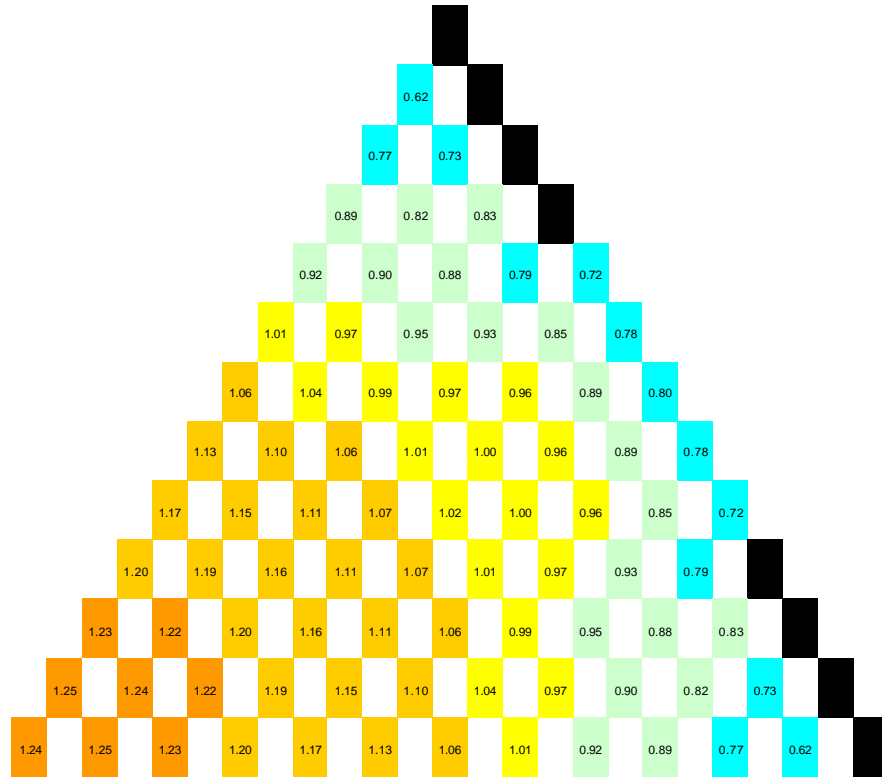


**Figure 2.8. Non-uniform Enrichment / Flat BOEC – BOEC Radial Power Distribution.**

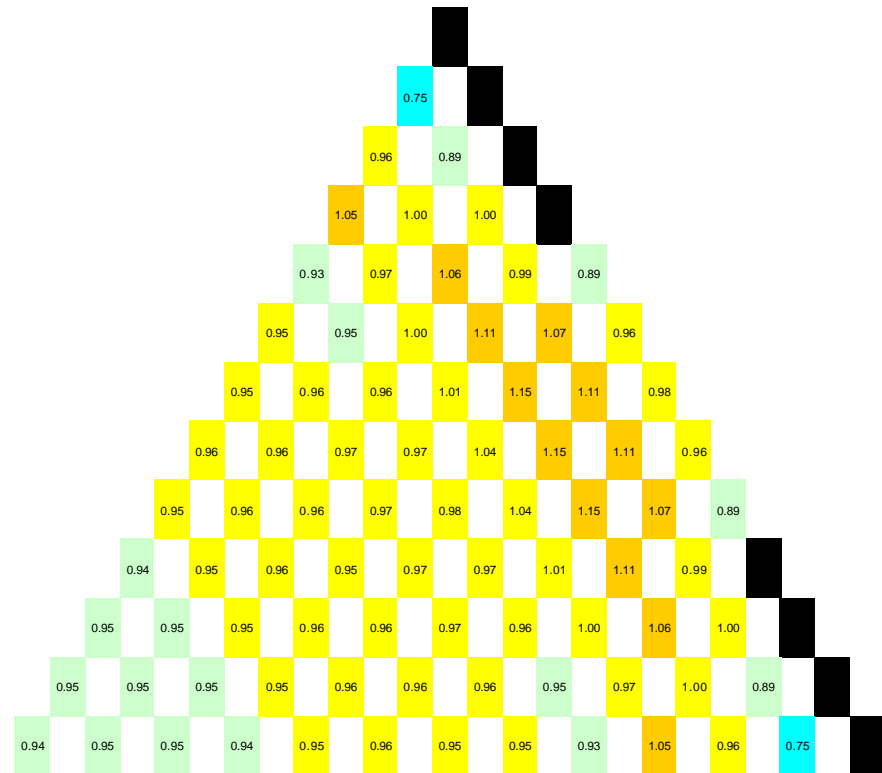


**Figure 2.9. Non-uniform Enrichment / Flat BOEC – MOEC Radial Power Distribution.**

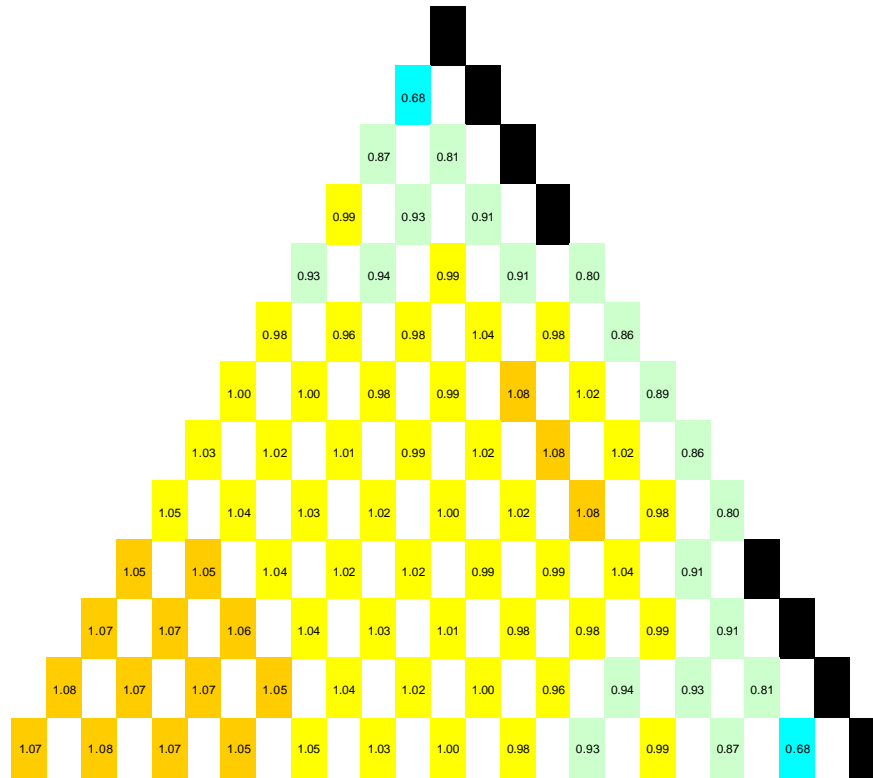




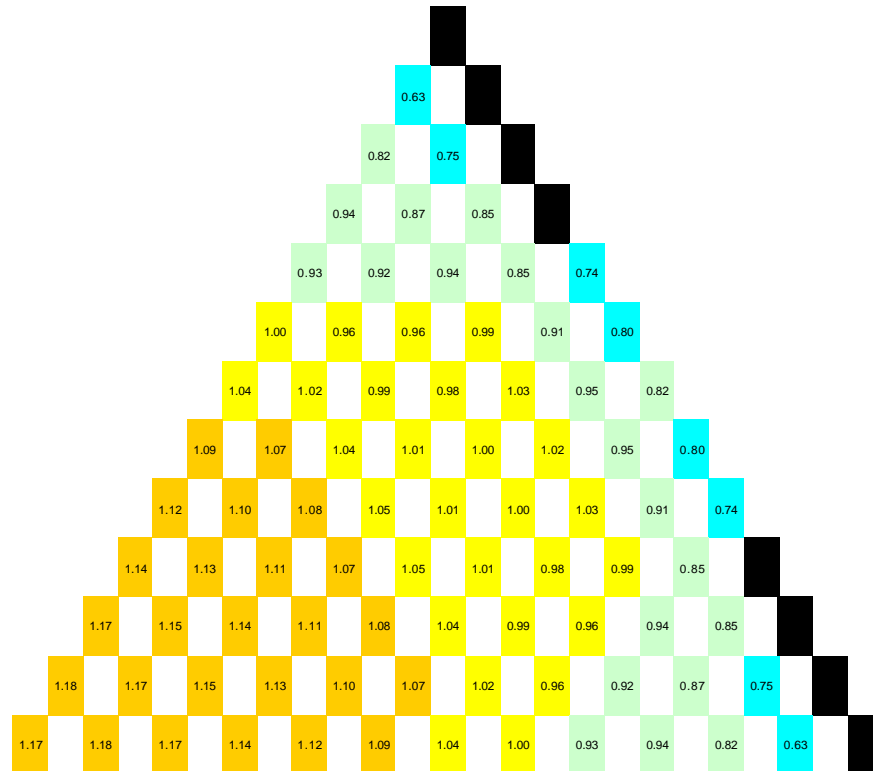
**Figure 2.10. Non-uniform Enrichment / Flat BOEC – EOEC Radial Power Distribution.**



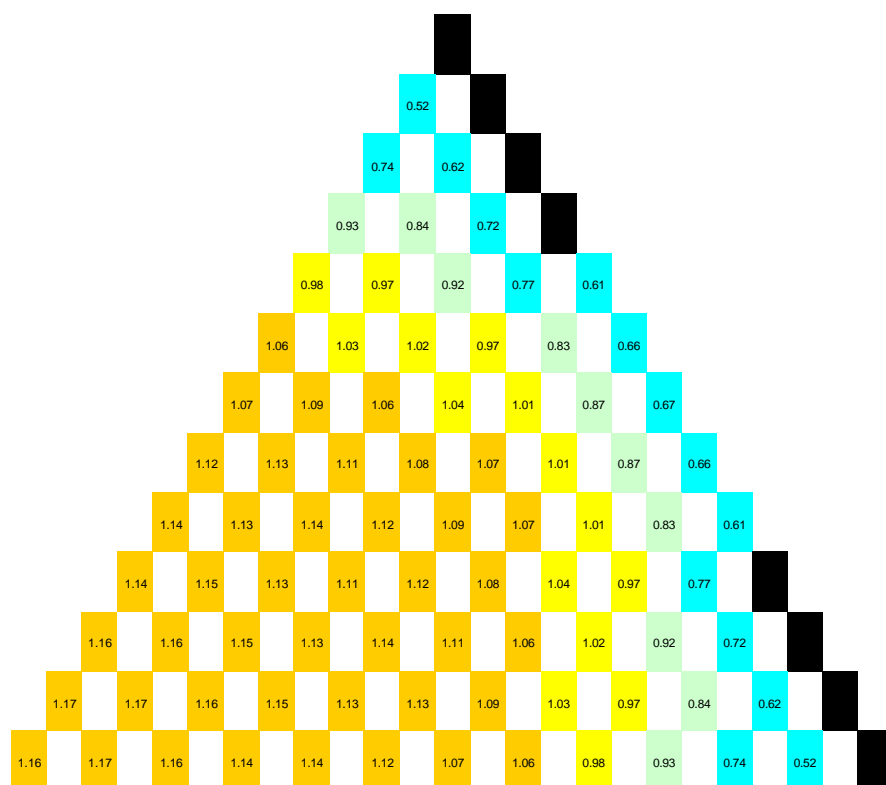
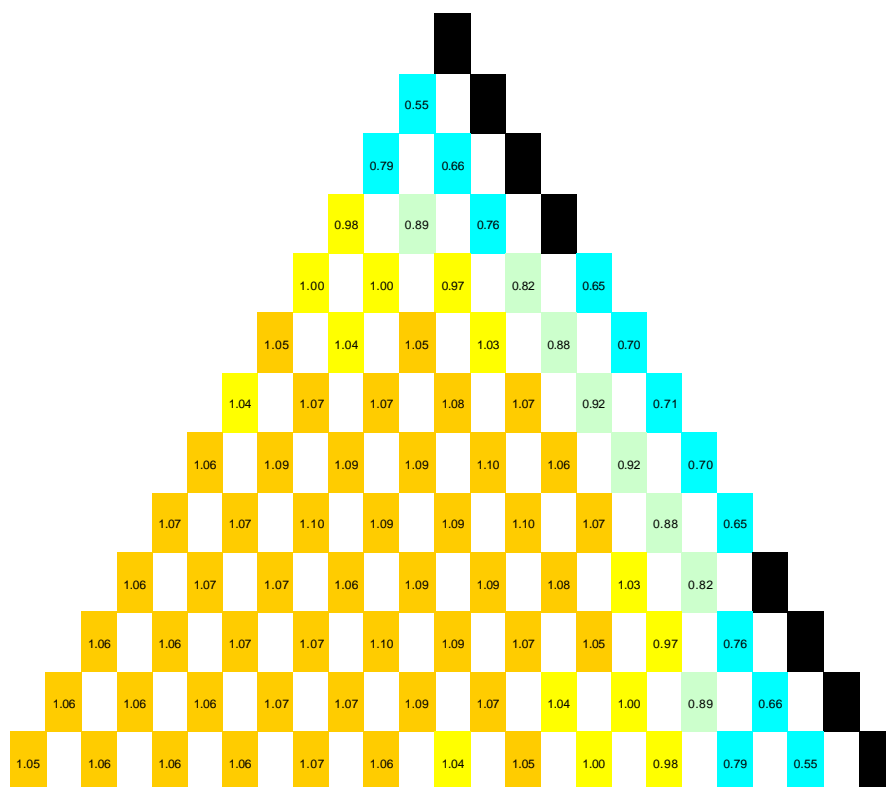
**Figure 2.11. Non-uniform Enrichment / No TRU limit – BOEC Radial Power Distribution.**



**Figure 2.12. Non-uniform Enrichment / No TRU limit – MOEC Radial Power Distribution.**



**Figure 2.13. Non-uniform Enrichment / No TRU limit – EOEC Radial Power Distribution.**





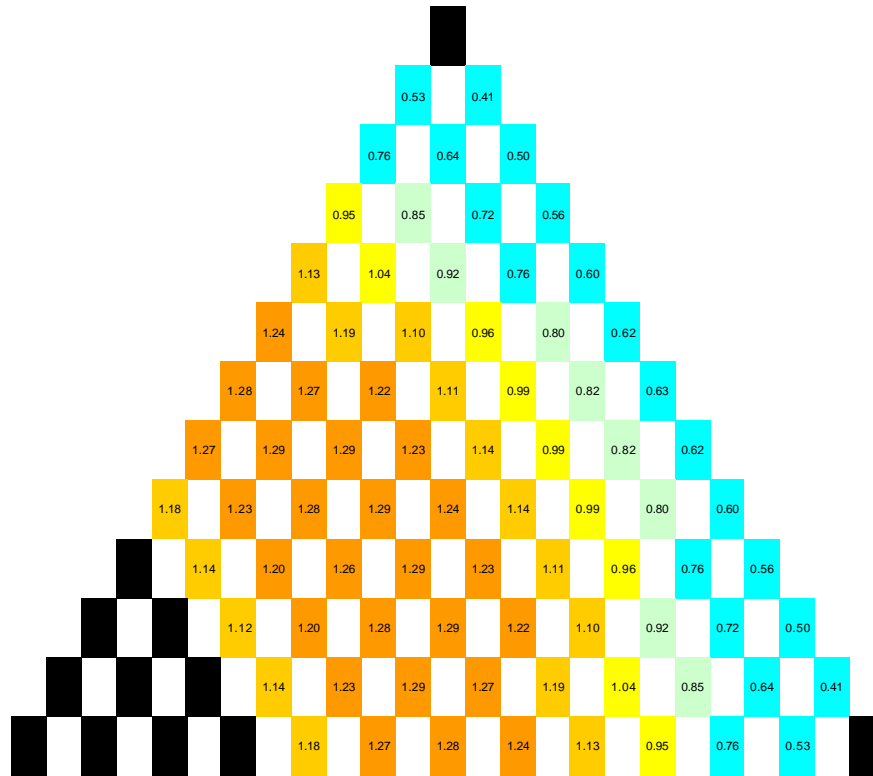


**Figure 2.18. Annular Core / Uniform Enrichment – MOEC Radial Power Distribution.**

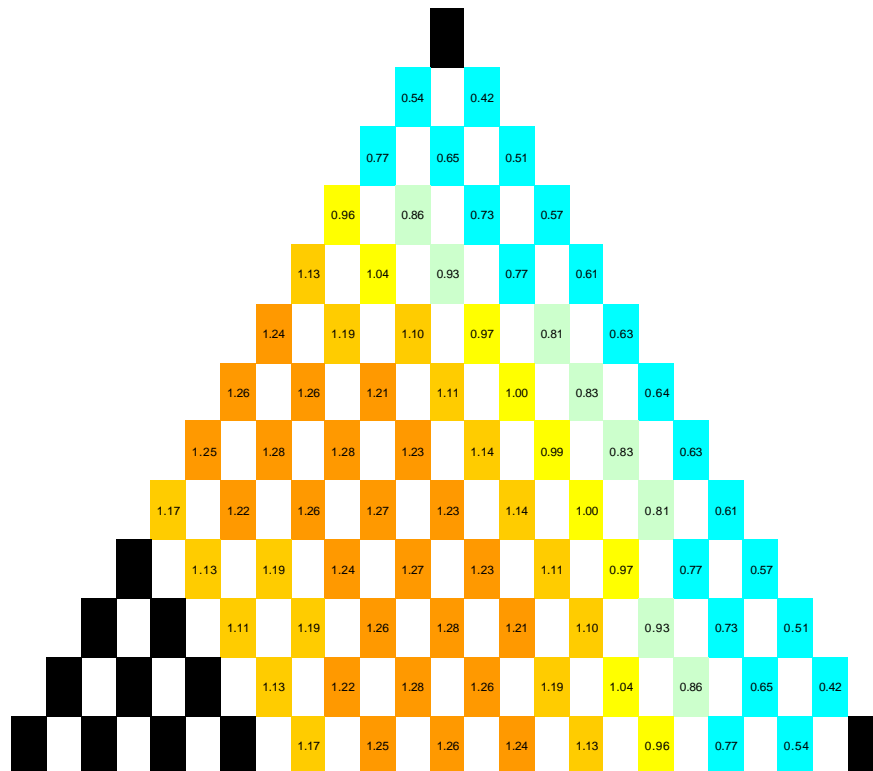


**Figure 2.19. Annular Core / Uniform Enrichment – EOEC Radial Power Distribution.**

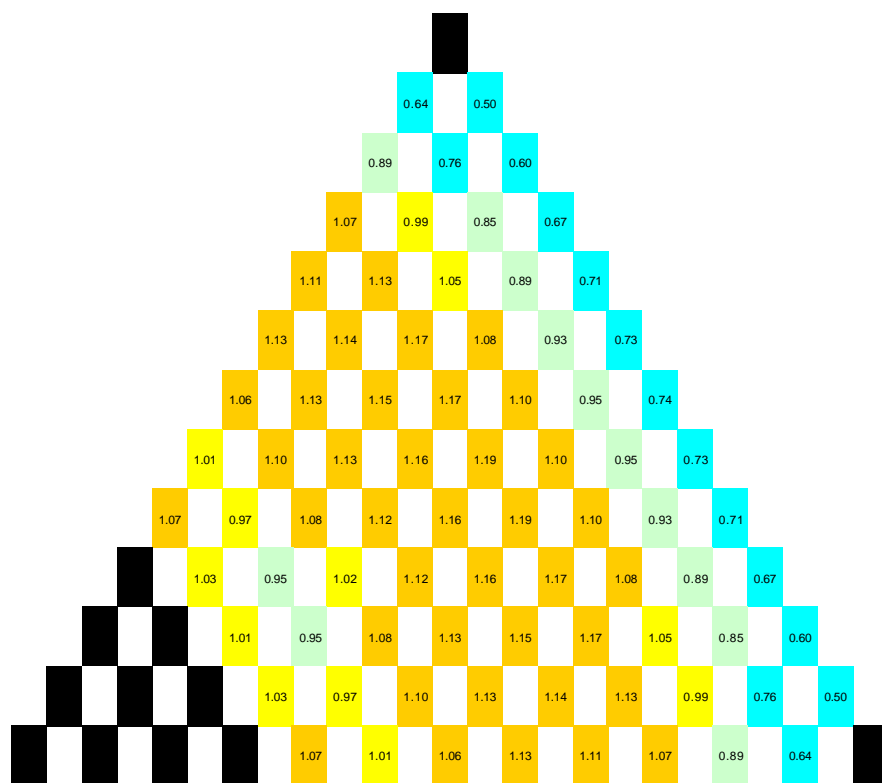


**Figure 2.20. Annular Core / Non-uniform Enrichment – BOEC Radial Power Distribution.**

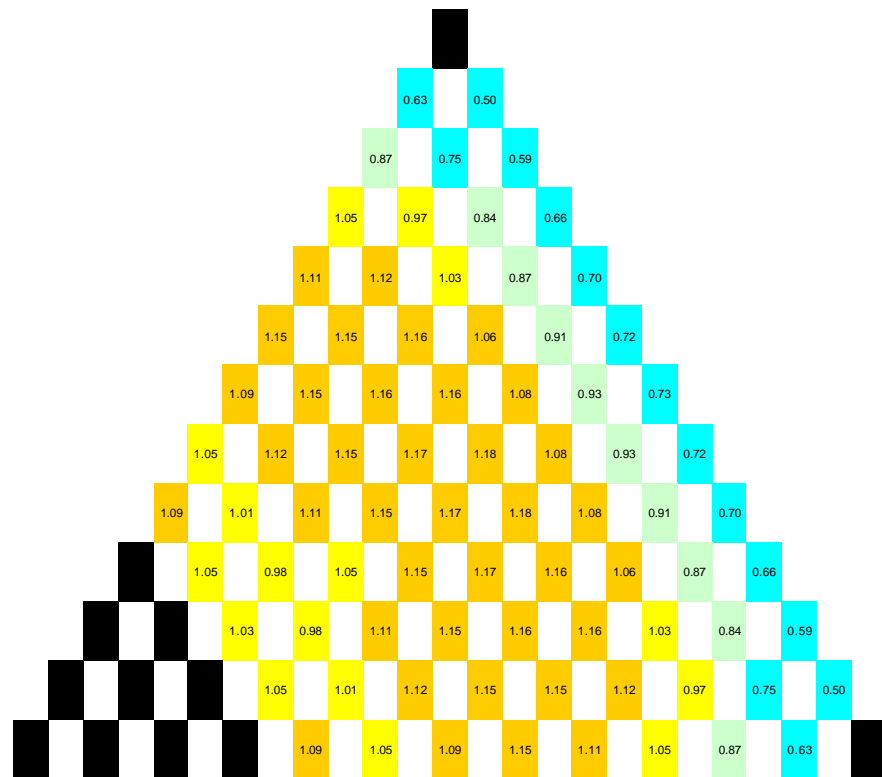


**Figure 2.21. Annular Core / Non-uniform Enrichment – MOEC Radial Power Distribution.**

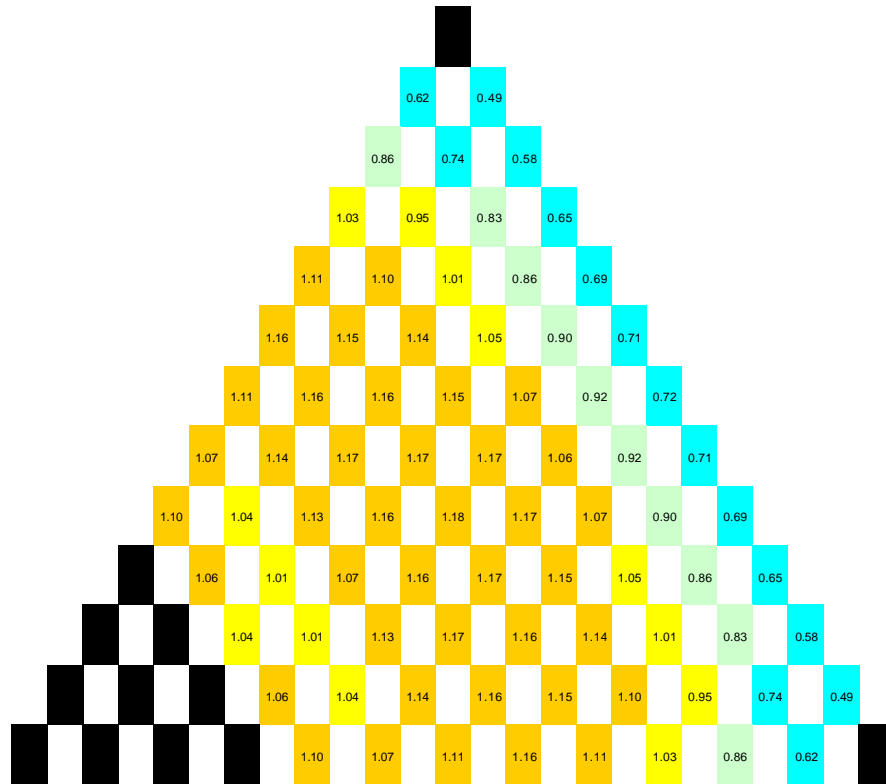


**Figure 2.22. Annular Core / Non-uniform Enrichment – EOEC Radial Power Distribution.**

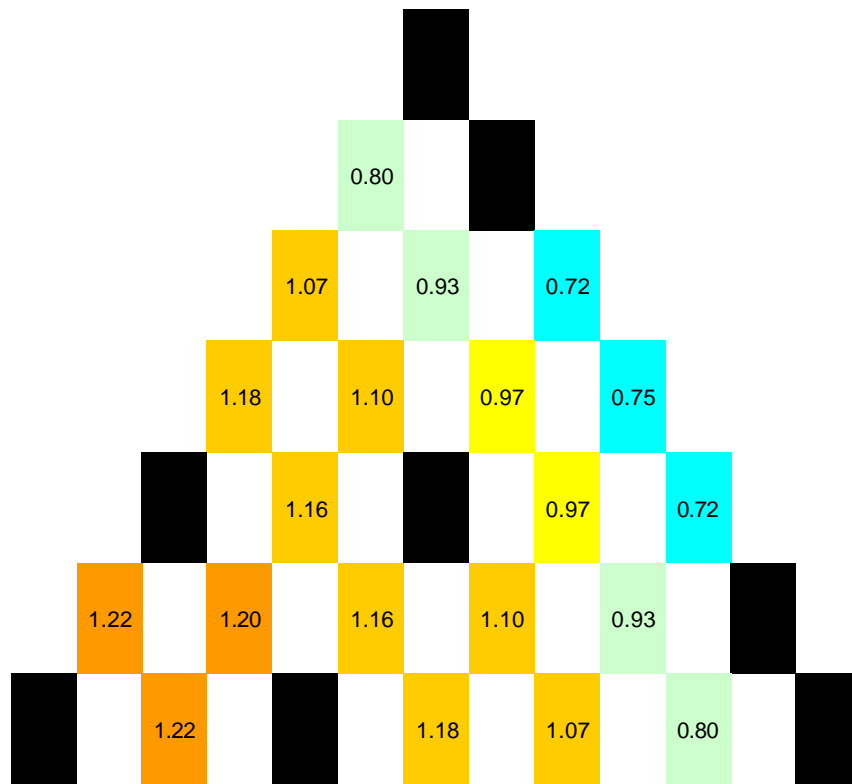


**Figure 2.23. Small 600 MWt Core – BOEC Radial Power Distribution.**

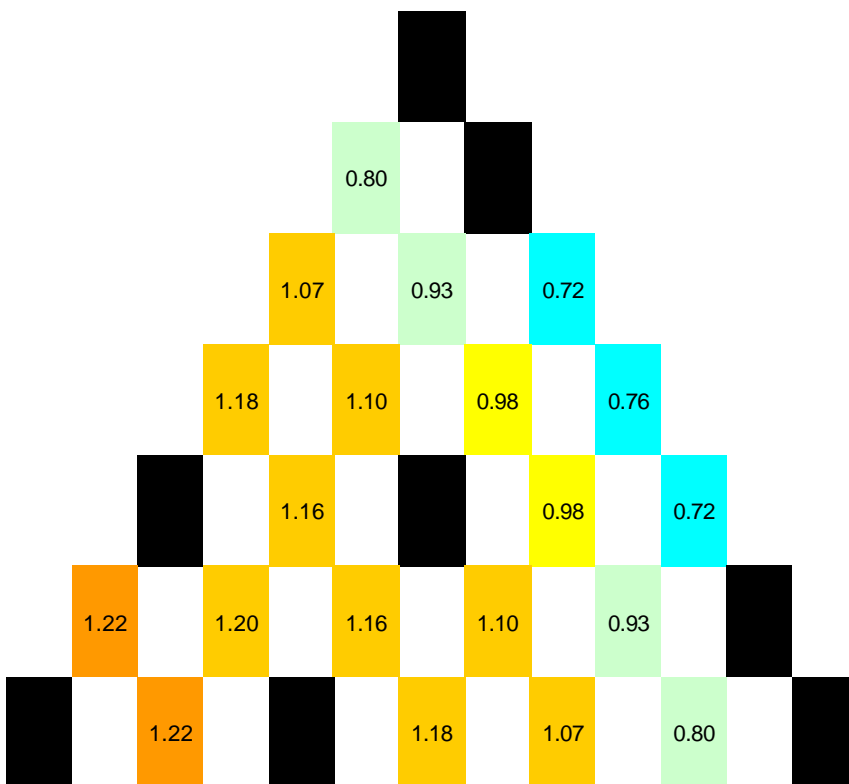


**Figure 2.24. Small 600 MWt Core – MOEC Radial Power Distribution.**

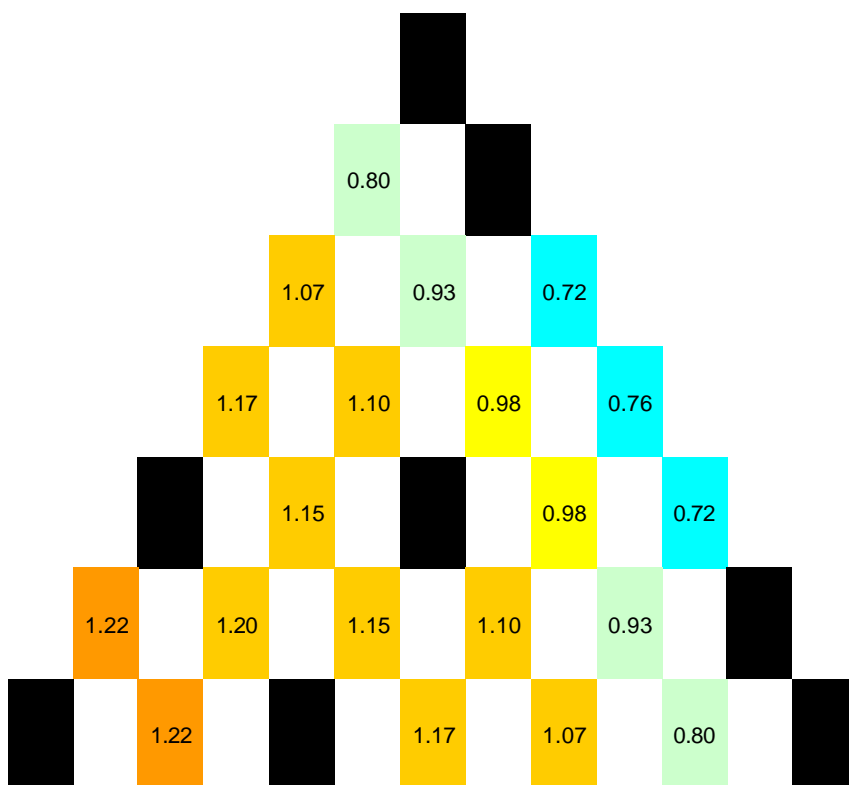


**Figure 2.25. Small 600 MWt Core – EOEC Radial Power Distribution.**



### 3.3.1.4 Control Rod Worth and Safety Parameter Evaluation

The reference core layout with a split batch fuel loading strategy with the maximum TRU enrichment limited to 20% TRU/HM was chosen for further analysis. This included the determination if sufficient control rod locations were included in the design and evaluation of a number of safety parameters. Table 2.2 includes a summary for this design. The performance is essentially unchanged from the original designs. Figure 2.26 shows the charge enrichment of each assembly in the split-batch design with the control and shutdown assemblies identified by bold outline.

The usual set of safety parameters were evaluated to confirm that there were no changes resulting from the enrichment splitting that could compromise the safety of the reactor. The results are included in Table 2.3. There are some significant changes from the uniform loading. The magnitude of the Doppler temperature coefficient increased by 50% and the depressurization reactivity is approximately 20% smaller relative to the uniform enrichment case.

The goal of the control rod analysis was to determine if sufficient control rod locations were included, but it was not intended to optimize the control rod design or even evaluate individual control rod worths. The methodology was to evaluate the  $k_{\text{eff}}$  of the reactor under a number of different conditions and evaluate the reactivity change based on the difference in  $k_{\text{eff}}$ . The results are provided in Table 2.4. Despite the lower core reactivity state at EOEC, the control rod worth required is actually limiting because the difference in neutron spectrum and power distribution reduces the worth of the control rods.

Natural boron in the form of  $B_4C$  was used in the available control locations. The results show that slightly less than the required reactivity is provided. The most reactive rod has nearly \$1 worth of reactivity. There is clearly sufficient space allocated to the control rods because the average rod reactivity required is only \$0.18. The B-10 enrichment needs to be increased in the control rods near the periphery and reduced in the centrally located control rods to increase the total reactivity of all the control rods and to spread the reactivity more uniformly among the individual control rods.

**Table 2.2. Design Summary.**

	Uniform	Split-Batch
Power (MWt)	2,400	2,400
Height / Diameter Ratio	0.282	0.282
Cycle Length (EFPD)	786	786
Cycles in Core	3	3
Charge Enrichment (TRU/HM)	16.5%	15-20%
Enrichment Zones	1	5
BOEC Heavy Metal Loading (MT)	56.4	56.6
EOEC Heavy Metal Loading (MT)	54.5	54.6
BOEC TRU Loading (MT)	9.6	10.3
EOEC TRU Loading (MT)	9.6	10.4
Average Discharge Burnup	10.0%	9.9%

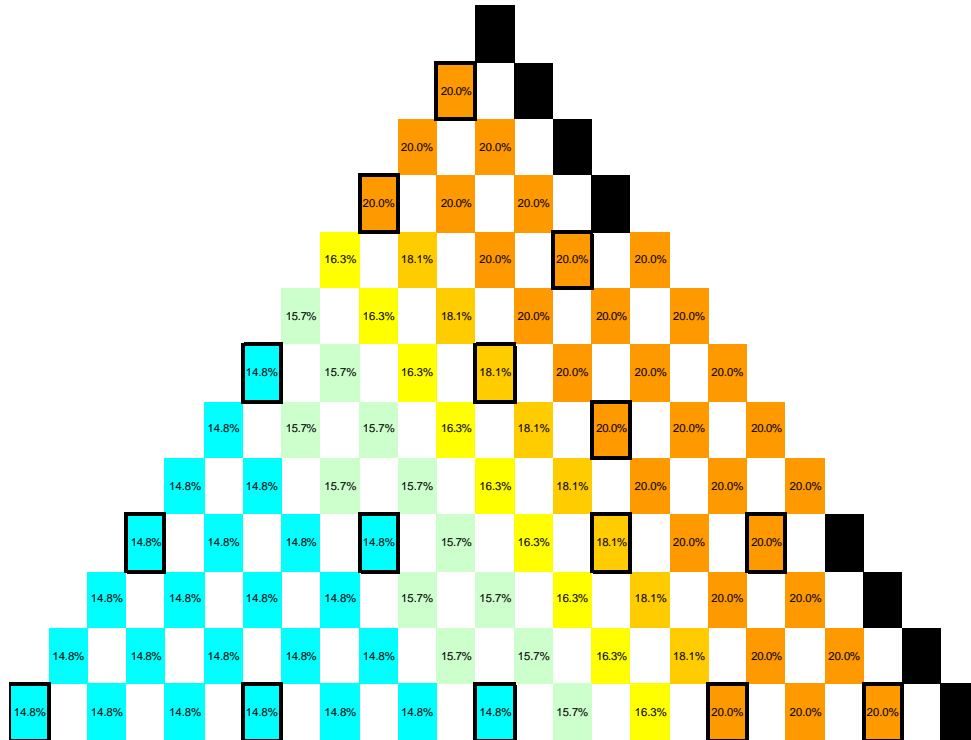


**Figure 2.26. TRU Charge Enrichment for the Split-Batch Core Design.**

**Table 2.3. Safety Parameters.**

	Uniform		Split-Batch	
	BOEC	EOEC	BOEC	EOEC
Beta	3.45E-3	3.39E-3	3.46E-3	3.40E-3
Prompt Neutron Lifetime ( $\mu\text{sec}$ )	2.54	2.03	2.67	2.15
Doppler Temperature Coefficient ( $^{\circ}\text{C}/\text{K}$ )	-0.19	-0.17	-0.30	-0.28
Radial Expansion Coefficient ( $\$/\text{cm}$ )	-0.52	-0.53	-0.42	-0.41
Axial Expansion Coefficient ( $\$/\text{cm}$ )	-0.08	-0.08	-0.15	-0.13
Depressurization Reactivity ( $\$$ )	1.33	1.39	1.09	1.15

**Table 2.4. Control Rod Reactivity Requirements.**

	BOEC	EOEC
Excess Reactivity	\$0.76	\$0.00
Depressurization	\$1.09	\$1.15
Hot-to-Cold (excludes expansion)	\$4.58	\$4.61
Minimum Shutdown	\$2.89	\$2.94
Extra Margin	\$1.00	\$1.00
Total Excess Reactivity Required	\$10.33	\$9.70
All Rods	-\$11.04	-\$9.56
All Rods - Minus Most Reactive Rod	-\$10.06	-\$8.64
Average Rod Reactivity Required	-\$0.19	-\$0.18
Most Reactive Rod	-\$0.98	-\$0.92

### 3.3.1.5 Conclusions

The minimum radial assembly peaking factor was estimated for a 2400 MWt, low-pressure drop ( $H/D=0.282$ ) design. Very low peaking (i.e.,  $<1.05$ ) does not seem to be practical in this large core. The minimum peak-to-average assembly power was estimated at approximately 1.2. Split-enrichment fuel loading was most effective at reducing the radial peaking. Increased TRU enrichment of the outer assemblies was used to pull the power from the center towards the periphery. Since the core was required to maintain a conversion ratio of unity, the power redistributed over the course of a cycle. Therefore, the minimum radial peaking factor was achieved by peaking the core towards the periphery, which would lead to a flatter power distribution at the middle of the cycle and then a core that was peaked towards the center at the end of the cycle. The use of enrichment greater than 20% only allowed for relatively small improvements over the design limited to a maximum of 20%. Part of the difficulty of flattening the power distribution was a result of eliminating the breeding blankets, which are a higher quality reflector than the  $Zr_3Si_2$  reflectors.

Fuel shuffling produces only a small improvement because the high conversion ratio produces small reactivity change over fuel lifetime. An annular core design, however gave a slightly lower peaking factor with very little power redistribution. The annular core requires a larger core diameter to accommodate the central reflector region. A small core (e.g., 600 MWt) will tend to have a much flatter radial power distribution.

The split-batch, 20% TRU enrichment limited core design was chosen for further evaluation. The performance and safety parameters were similar to that of the uniform enrichment designs. The total control rod worth for this layout was slightly low with natural boron used in all control rod locations. Using different boron enrichments in the various control rod locations should easily provide sufficient reactivity control and prevent excessive reactivity in a single control rod.

### References

- 2.1 Toppel B. J., "A User's Guide to the REBUS-3 Fuel Cycle Analysis Capability," ANL-83-2, Argonne National Laboratory (1983).
- 2.2 Henryson II H., Toppel B. J., and Stenberg C. G., "MC2-2: A Code to Calculate Fast Neutron Spectra and Multigroup Cross Sections," ANL-8144, Argonne National Laboratory (1976).
- 2.3 Derstine K. L., "DIF3D: A Code to Solve One-, Two-, and Three-Dimensional Finite-Difference Diffusion Theory Problems," ANL-82-64, Argonne National Laboratory (1984).
- 2.4 Adams C. H., "Specifications for VARI3D – A Multidimensional Reactor Design Sensitivity Code," FRA-TM-74, Argonne National Laboratory (1975).

### 3.3.2 Fuel Pin Mechanical Design

A scoping study was performed to investigate the thermal mechanical behavior of several conceptual designs for the fuel pin. The material specified for the pin cladding was silicon carbide (SiC), which has excellent high temperature mechanical properties. The

study only looked at the response of a single fuel pin attached to the support grid of a hexcan. Finite element analyses were performed for the different fuel pin configurations subjected to axial temperature variations; circumferential temperature variations were not considered at this time. For the recommended configuration, a conceptual design is proposed for the attachment of the fuel pin to the hexcan support grids.

### 3.3.2.1 Fuel Pin Geometry

Due to current projections of fabrication restrictions on long SiC tubing, and the required length of the fuel pin, the fuel pin is assumed to be made in two 1.67 m long sections as shown in Figure 3.1. The two-piece fuel pin will also be referred to as the two pin design, as each piece will be capped at both ends.

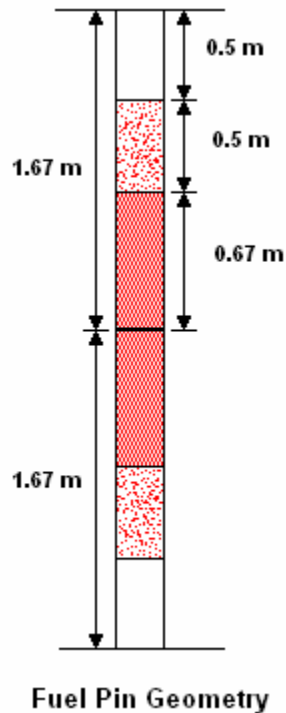


Figure 3.1 Fuel pin geometry

The upper and lower sections of the two-piece fuel pin are essentially identical, i.e., mirror images. The top of the upper fuel pin section is a 0.5 m long upper axial fission gas plenum, below which there is a 0.5 m long upper axial reflector. The lower portion of the upper fuel pin section contains a 0.67 m length of fuel pellets that when combined with the 0.67 m upper portion of the lower fuel pin section forms the 1.34 m active core length. The lower portion of the lower fuel pin section forms a 0.5 m lower axial reflector length and a 0.5 m lower axial fission gas plenum length. The fuel pin outside diameter is 0.957 cm and the fuel clad thickness is 0.1 cm.

### 3.3.2.2 Fuel Pin and Hexcan Temperature Distributions

Data was provided for the axial temperature distribution in the active core region of the fuel pin. The coolant temperature at the inlet is given as 485 °C. From this data, the temperature at the bottom of the fuel pin is assumed to equal the inlet coolant temperature, and the axial temperature in the lower portion of the fuel pin is assumed to vary linearly through the plenum and reflector until the temperature of the bottom of the active core region is reached. The axial temperature distribution in the “unheated” upper reflector and plenum regions is assumed to vary linearly from the temperature at the top of the active core region, 993.58 °C, to approximately 915 °C. This is basically the bulk coolant outlet temperature. The axial temperature profile of the fuel pin is shown in Figure 3.2. The fuel pin temperature was assumed to be constant in the circumferential direction.

The axial temperature profile assumed for the hexcan (Figure 3.2) is dictated by the temperature of the fuel pin at its endpoints, where the fuel pin is attached to the hexcan. Essentially, the hexcan, which is unheated, follows the coolant temperature profile up the flow channel. The hexcan temperature was assumed to be constant in the circumferential direction also.

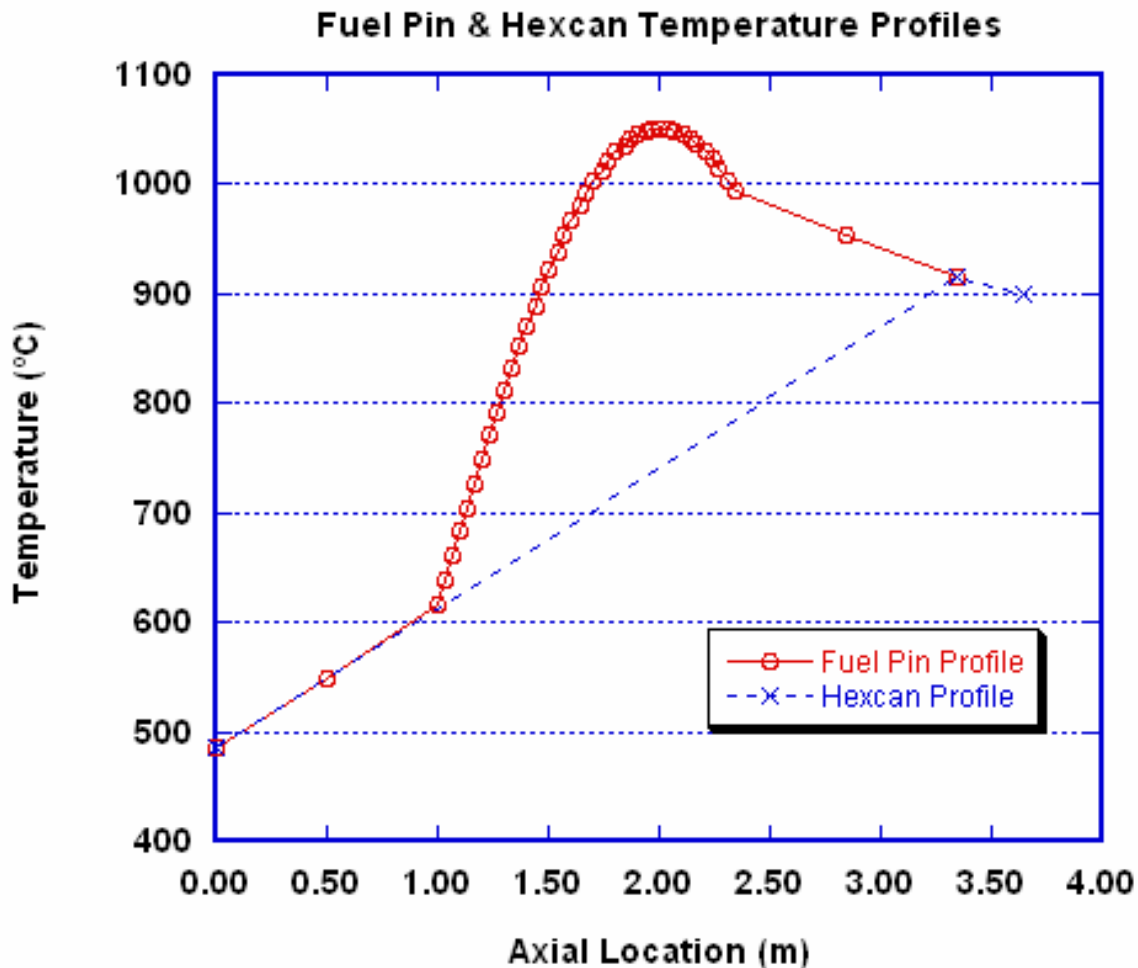


Figure 3.2 Fuel pin and hexcan axial temperature profiles

### 3.3.2.3 Fuel Pin Material Properties

The fuel pin clad is made of SiC. The properties of bulk SiC used in the finite element analysis are:

- Elastic Modulus: 460 GPa
- Density: 3.25 g/cm<sup>3</sup>
- Coefficient of Thermal Expansion:  $4.0 \times 10^{-6}/^{\circ}\text{C}$
- Poisson's Ratio: 0.18
- Tensile Strength: 100 MPa
- Flexural Strength (@RT): 700 MPa
- Compressive Strength (@RT): 4.6 GPa

It should be noted that from a theoretical consideration, the flexural strength should be equal to the tensile strength. However, it has been observed that for brittle materials, which are sensitive to surface flaws, these two values are usually not equal. Thus, the lower valued tensile strength could be considered a lower bound value for failure, and the flexural strength as the most probable value for failure in bending.

### 3.3.2.4 Fuel Pin Structural Analysis Configurations

Six fuel pin configurations were examined using finite element analysis. In four of the six cases, the two-piece fuel pin was modeled as a single piece fuel pin. This simplification presupposes that the two sections of the fuel pin can be joined in such a way to form one contiguous length of material, or that a method can be found to form full length SiC fuel pins. Also in four of the six cases, the effect of connecting and constraining the fuel pin within a hexcan is introduced.

#### 3.3.2.4.1 Case 1: One-piece simply supported fuel pin

This configuration represents the simplest case possible (Figure 3.3). The ends of the fuel pin are constrained so as to restrict translational motion only. The ends of the fuel pin will be attached to the fuel support plates. A translational constraint in the  $i$ -th coordinate direction is denoted by  $\mathbf{T}_i$ , and a rotational constraint about the  $i$ -th coordinate axis is denoted by  $\mathbf{R}_i$ . Thus,  $\mathbf{T}_{xyz}$  indicates that the point is constrained from motion in the  $x$ ,  $y$  and  $z$  directions, and  $\mathbf{R}_x$  indicates that rotation about the  $x$ -axis is constrained. This is the case of a fuel bundle with no spacer grids.



Figure 3.3 Case 1: One-piece simply supported fuel pin

#### 3.3.2.4.2 Case 2: Two-piece fuel pin with ends simply supported and center fixed

This configuration represents the case of two fuel pins joined together with all motion restricted at the connection (Figure 3.4). This is the case of a fuel bundle design with a single fuel support grid at the midplane of the fuel pins.

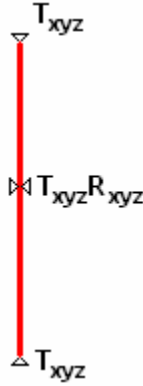


Figure 3.4 Case 2: Two-piece simply supported fuel pin with center fixed

#### 3.3.2.4.3 Case 3: One-piece fuel pin within hexcan

Case 3 introduces the effects of the hexcan in constraining the fuel pin (Figure 3.5). The lower end of the fuel pin and hexcan are joined and simply supported. The upper end of the hexcan is simply supported and allowed to move in the axial direction, while the upper end of the fuel pin is joined to the hexcan and is thus constrained to move with the hexcan. The top and bottom fuel support grids provide the structural attachment. This model takes into account the axial thermal expansion of the hexcan

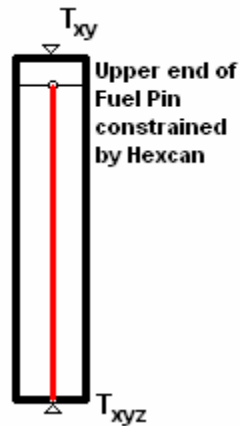


Figure 3.5 Case 3: One-piece fuel pin within hexcan

#### 3.3.2.4.4 Case 4: One-piece fuel pin and single spacer within hexcan

Case 4 is identical to Case 3 with the addition of a single spacer centered axially along the fuel pin (Figure 3.6). The spacer restricts the fuel pin from moving laterally within the hexcan but allows for axial motion likely to occur due to thermal expansion.

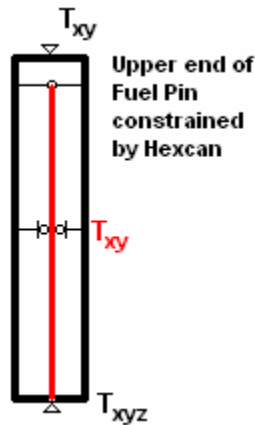


Figure 3.6 Case 4: One-piece fuel pin and single spacer within hexcan

#### 3.3.2.4.5 Case 5: One-piece fuel pin and three spacers within hexcan

Case 5 expands on Case 4 by adding two more spacers located at the ends of the active core of the fuel pin (Figure 3.7). The spacers restrict fuel pin lateral movement while allowing for axial motion likely to occur due to thermal expansion.

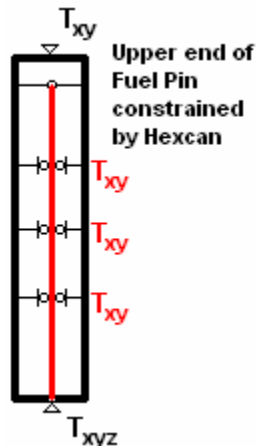


Figure 3.7 Case 5: One-piece fuel pin and three spacers within hexcan

#### 3.3.2.4.6 Case 6: Two-piece fuel pin fixed to the hexcan at the center support grid with ends free to expand axially

Case 6 introduces a conceptual design for the attachment of the fuel pin to the hexcan supports to mitigate thermal stresses developed and minimize lateral bowing of the fuel pin (Figure 3.8). A two-piece fuel pin is rigidly attached to the hexcan so the ends of the two fuel pin sections are joined at the axial center of the hexcan with the center support grid (Figure 3.9). The other ends of the two fuel pin sections are constrained to prevent lateral motion but are allowed to translate axially to accommodate thermal expansion (Figure 3.10).



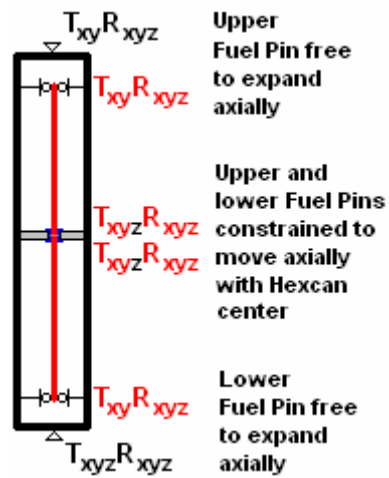


Figure 3.8 Case 6: Two-piece fuel pin with free ends and centers fixed to hexcan

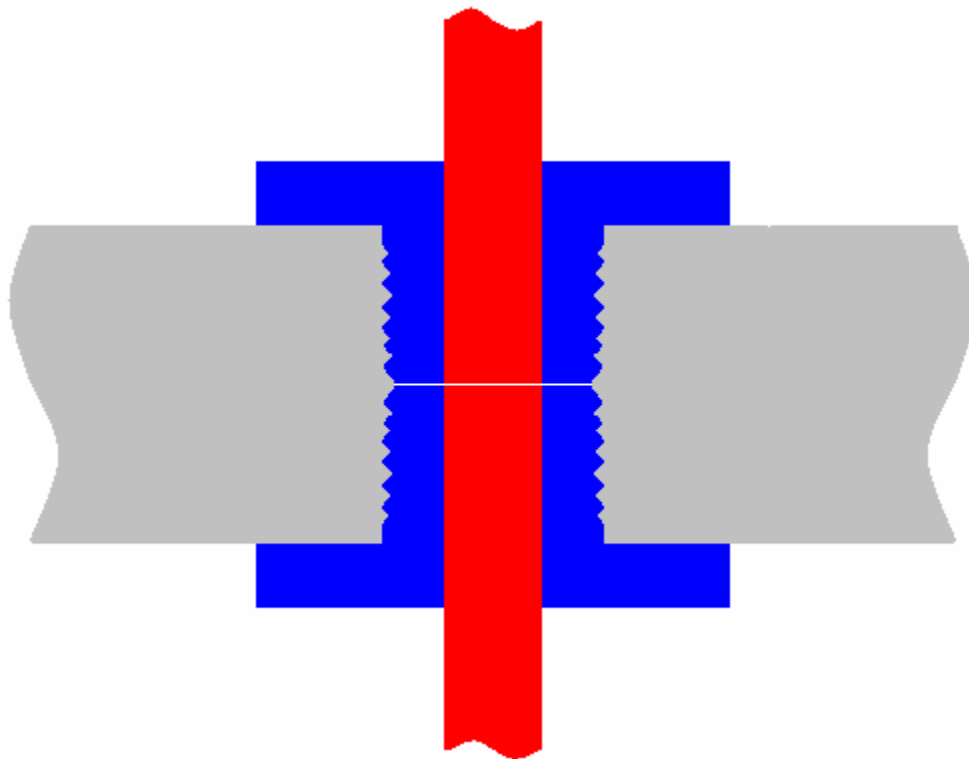


Figure 3.9 Conceptual design for fuel pin attachment to center support grid

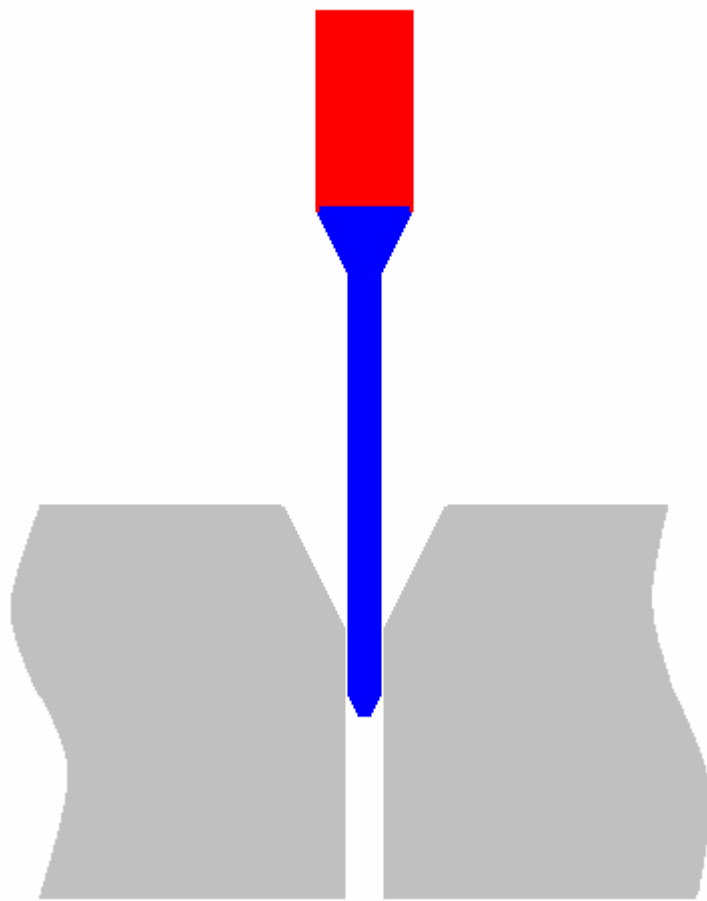


Figure 3.10 Conceptual design for fuel pin end support

### **3.3.2.5 Fuel Pin Analysis Displacement Results**

Finite element analyses were performed for each configuration and lateral displacement, or bowing, of the fuel pin was examined. In order to initiate the lateral displacement, the fuel pin was modeled with a very slight imperfection. This is reasonable because the manufacturing process would not produce a perfectly straight fuel pin. The chosen imperfection was a sinusoidal shape with a maximum lateral displacement of 0.01 cm at its axial midpoint.

#### ***3.3.2.5.1 Case 1: One-piece simply supported fuel pin***

This case exhibited the greatest amount of fuel pin lateral displacement. A maximum lateral displacement of 7.8 cm was calculated for the axial midpoint of the fuel pin (Figure 3.11).

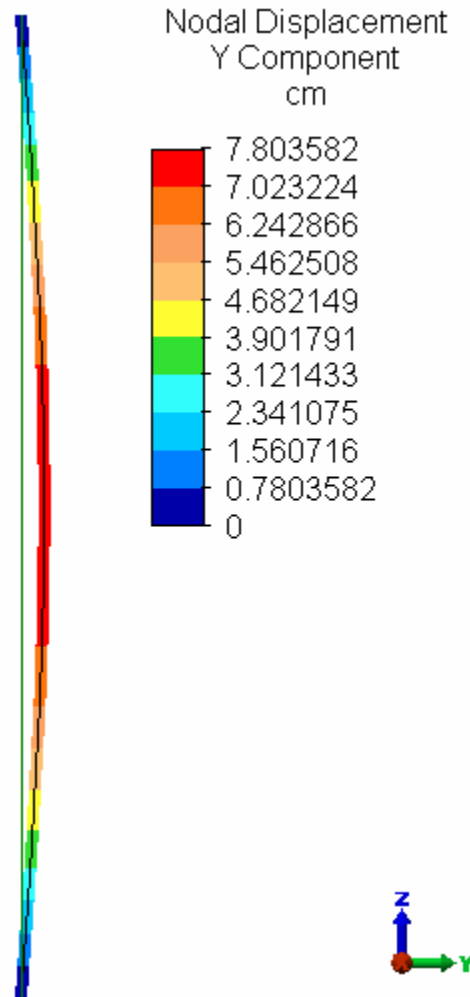


Figure 3.11 Case 1 fuel pin lateral displacement

#### ***3.3.2.5.2 Case 2: Two-piece fuel pin with ends simply supported and center fixed***

The maximum lateral displacement of the fuel pin for Case 2 is approximately 4.5 cm and occurs near the axial midpoint of the upper section of the two-piece fuel pin (Figure 3.12). It should be noted that this behavior agrees with intuition. Since the temperatures are higher in the upper section of the fuel pin, it is expected that the upper section of the fuel pin will expand more than the lower section, and as a result, will experience greater lateral displacement.

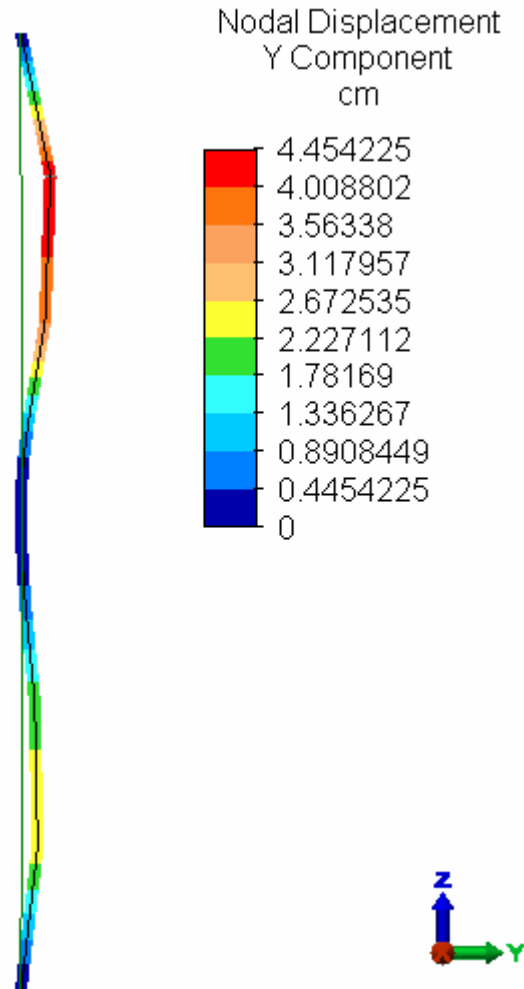


Figure 3.12 Case 2 fuel pin lateral displacement

#### 3.3.2.5.3 Case 3: One-piece fuel pin within hexcan

The lateral displacement of the fuel pin for Case 3 is mitigated due to the effect of the hexcan (Figure 3.13). The hexcan temperatures are not as high as those experienced by the fuel pin, so the hexcan does not lengthen as much due to thermal expansion as the unrestrained fuel pin would. The upper end of the fuel pin is constrained to move with the hexcan. In this configuration, the unrestrained axial midpoint of the fuel pin experiences a maximum lateral displacement of 4.6 cm, an amount 41% less than the 7.8 cm bowing predicted for Case 1, which did not move axially.

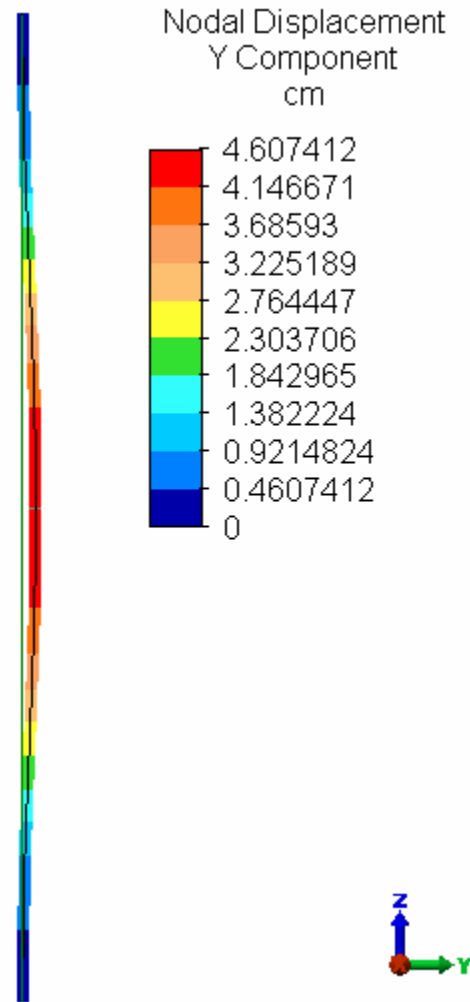


Figure 3.13 Case 3 fuel pin lateral displacement

#### ***3.3.2.5.4 Case 4: One-piece fuel pin and single spacer within hexcan***

The single spacer restricts lateral displacement of the fuel pin at its axial midpoint. The maximum lateral displacement is approximately 2.18 cm and occurs in the upper portion of the fuel pin (Figure 3.14). The maximum lateral displacement in the lower portion of the fuel pin is only slightly less at 2.17 cm.

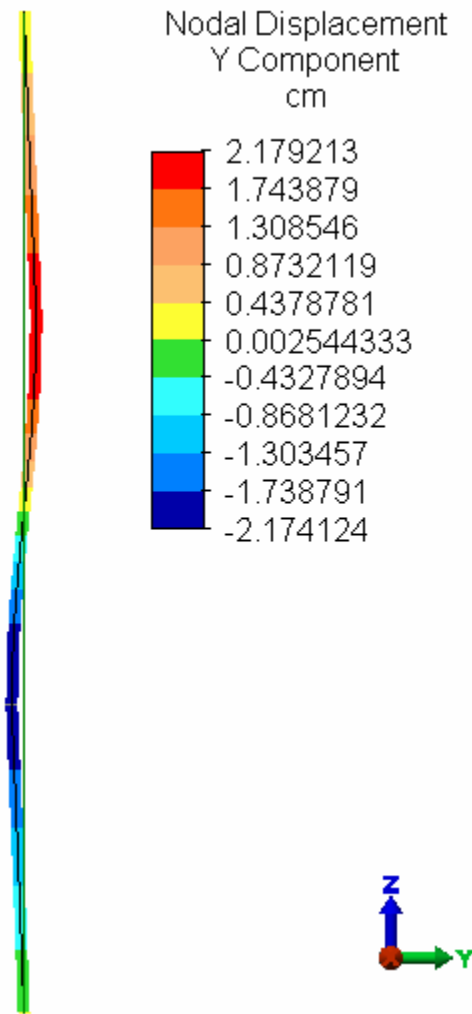


Figure 3.14 Case 4 fuel pin lateral displacement

#### 3.3.2.5.5 Case 5: One-piece fuel pin and three spacers within hexcan

Three spacers restrict lateral displacement of the fuel pin at additional locations. The maximum lateral displacement for Case 5 is approximately 1.0 cm and occurs in the upper portion of the fuel pin in the region above the upper spacer (Figure 3.15). The maximum lateral displacement in the lower portion of the fuel pin below the lower spacer is only slightly less at 0.99 cm.

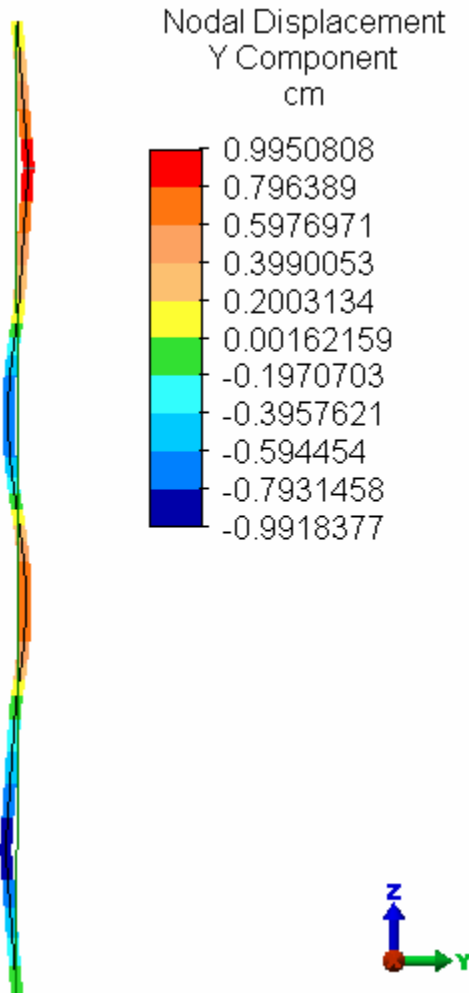


Figure 3.15 Case 5 fuel pin lateral displacement

#### ***3.3.2.5.6 Case 6: Two-piece fuel pin fixed to hexcan at center support grid with ends free to expand axially***

Case 6 exhibits no appreciable lateral displacement. The upper and lower ends of the two-piece fuel pin are free to expand axially, while the middle of the fuel pin is constrained to move with the hexcan. The axial displacement of the fuel pin in this configuration is given in Figure 3.16.

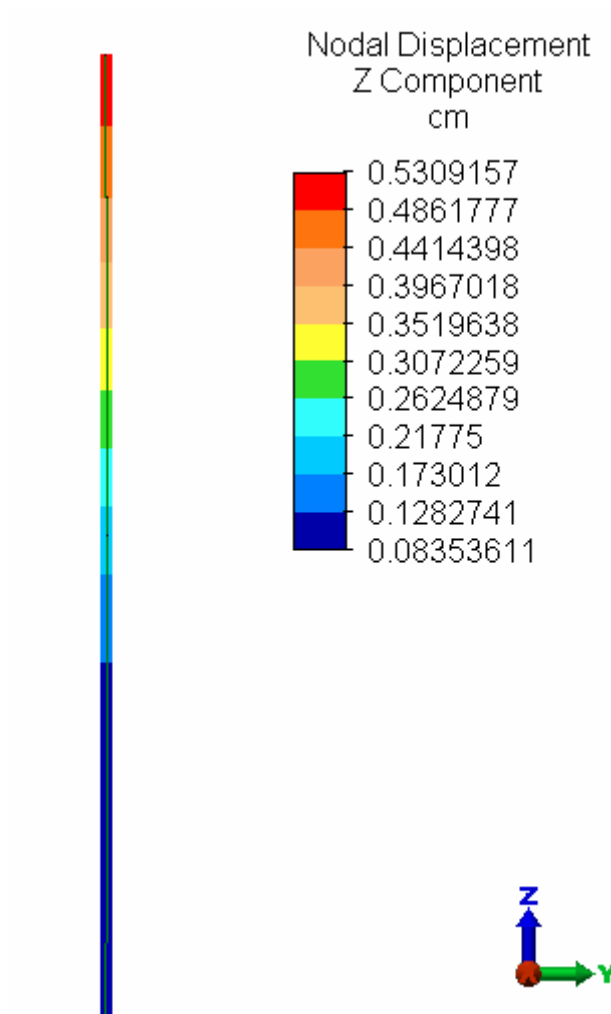


Figure 3.16 Case 6 fuel pin axial displacement

### 3.3.2.6 Fuel Pin Structural Analysis Results Summary

In addition to fuel pin displacements, axial forces and stresses that develop within the fuel pin due to the thermal loading are examined. The axial force developed is compared to the critical buckling force calculated for each case except Case 6. No compressive axial force develops in Case 6 since the ends of the fuel pin are free to expand axially.

The critical buckling load,  $P_{cr}$ , depends on the geometric end conditions of the fuel pin and is calculated using the following equation:

$$P_{cr} = \frac{p^2 EI}{(KL)^2} \quad (2-1)$$



where,  $E$  is the elastic modulus of the material,  $I$  is the moment of inertia of the fuel pin cross section,  $L$  is the length of the fuel pin, and  $K$  is a dimensionless coefficient dependent on the geometric end conditions [Budynas, 1977]. For the configurations of Case 1 and Case 3,  $L = 3.34$  m and  $K = 1.0$ . For the configuration of Case 2,  $L = 1.67$  m and  $K = 0.7$ . In Case 4,  $L = 1.67$  m and  $K = 1.0$ . In Case 5,  $K = 1.0$  and  $L = 0.67$  m.

The fuel pin structural analysis results for all six cases are summarized in Table 3.1.

Table 3.1. Summary of fuel pin structural analyses

Fuel Pin Configuration	Steady State Compressive Axial Force in Fuel Pin (Newtons)	Fuel Pin Critical Buckling Force (Newtons)	Maximum Compressive Stress in Fuel Pin (MPa)	Maximum Tensile Stress in Fuel Pin (MPa)	Fuel Pin Bowing (cm)	Fuel Pin Axial Expansion (cm)
1) Simply Supported Fuel Pin	102.5	102	158	149	7.8	n/a
2) Two Pins fixed at center joint and pinned at ends	930 (both upper and lower pins)	833	36.2 (upper pin) 35.5 (lower pin)	No Tensile Stress: Compressive axial stresses dominate bending tensile stresses	4.45 (upper pin) 2.53 (lower pin)	n/a
3) One Fuel Pin w/ HexCan	422	102	205	173	4.6	0.29
4) One Fuel Pin w/ HexCan and 1 spacer grid	891	408	306	240	2.2	0.29
5) One Fuel Pin w/ HexCan and 3 spacer grids	2890	2540	538	324	1.0	0.29
6) 2 Fuel Pins attached to HexCan center support grid, ends free to expand	n/a	n/a	0.000912 (upper pin) 0.000193 (lower pin)	0.000912 (upper pin) 0.000193 (lower pin)	~0	0.33 (upper pin) 0.12 (lower pin)

### 3.3.2.7 Summary and Conclusions

A scoping study was performed to gain insight into the thermal mechanical behavior of the fuel pin when subjected to axial thermal gradients. No circumferential thermal gradients were considered here. The response of only a single pin was modeled; interactions with adjacent pins will be considered in future work. Some of the models included the thermal mechanical response of the hexcan because the hexcan will see different axial temperature gradients. A potential design for a split fuel pin was

developed that did not develop significant stresses or bowing under only axial temperature gradients.

Six fuel pin configurations were examined to determine their thermal mechanical behavior when subjected to an axial temperature variation.

- Because of the differential thermal expansion between the hexcan and fuel pin, five configurations developed compressive forces that exceed the critical buckling force. However, this is of no consequence because the fuel pin is not a structural element and, thus, would not collapse.
- Four configurations developed tensile stresses that exceed the tensile strength of the material but do not exceed the flexural strength. The compressive strength of the material was far from being reached.
- Five configurations led to measurable lateral displacement, or bowing, of the fuel pin. Constraints imposed by adjacent fuel pins, which were not considered here, would reduce bowing.
- One configuration (Case 6) avoided developing significant forces and stresses in the fuel pin, and did not exhibit appreciable bowing.

It is recommended that the configuration for Case 6 should be considered for further evaluation in the initial design of the Generation IV Advanced Gas Cooled Reactor

#### References

3.1 Budynas R.G., Advanced Strength and Applied Stress Analysis, McGraw-Hill, Inc., New York, 1977.

### **3.3.3 Subassembly Thermal-Hydraulic Design**

The 2400 MWt Gas Fast Reactor (GFR), which is being developed, uses helium at 70 bars as the primary coolant. It is a direct-cycle reactor, which has the turbine included in the primary loop. During normal shutdown conditions, there is a powered shutdown heat removal system to extract the decay heat and maintain safe temperatures within the reactor core. This memo addresses an abnormal (emergency) shutdown condition where it is assumed that there are no available power sources to drive a compressor. For this situation the plant is to have emergency heat exchangers (EHXs) that are connected via piping in series with the reactor core, Figure 4.1. During normal reactor operation, check valves isolate the EHXs from the primary loop. When the EHXs are needed, the check valves open and the core and emergency heat exchangers are part of a closed flow loop. A supply of cold water is used to directly or indirectly cool the secondary side of the EHXs. This heat extraction cools the helium as it passes through the EHXs. Natural circulation drives the helium flow, which is heated as it passes up through the reactor core and cooled as it passes down through the EHXs. An important parameter is the helium pressure in the EHX loop, which will be much less than 70 bars when the EHXs are needed to cool the core. As this pressure decreases, the amount of coolant in the loop decreases along with the ability of the coolant to circulate and extract heat. It is essential that the behavior of this loop and its thermal-hydraulic limitations be well understood. Decay heat removal in the natural circulation in the helium-cooled loop formed with the

reactor core in the hot leg and the emergency heat exchangers in the cold leg, Figure 4.1, is studied. The friction pressure drop and the buoyancy pressure rise are studied separately so that greater insight into the behavior of the system can be obtained. It is observed that a fixed decay power level and system pressure in some instances can result in two possible steady states—one at a relatively high flow rate and low reactor coolant outlet temperature and another at a very low flow rate with very high reactor coolant outlet temperature. It is also observed that when the system pressure is too low, there may be no steady state condition for the system. Hence, a thorough understanding of this thermal-hydraulic behavior is essential in order to develop an effective subassembly thermal-hydraulic design.

### 3.3.3.1 Subassembly Geometry

Table 4.1 shows the current fuel bundle design.

Table 4.1 T-H Characteristics 2400MWt Pin Bundle

<b>2400 MWt Pin Core</b>	
(U,Pu)C	
<b>T-H Parameters</b>	
Reactor power, MWt	2400
Core power density, MW/m <sup>3</sup>	100
Core inlet temperature, C	480
Core outlet temperature, C	850
System pressure, MPa	7
Core pressure drop (excluding acceleration), bar	0.54
Peak Clad temperature, C	1044
Spacer pressure drop, Pa	12170
Friction pressure drop, Pa	38094
Acceleration pressure drop, Pa	3324
Inlet pressure drop, Pa	1691
Outlet pressure drop, Pa	1802
<b>Fuel Assembly Geometry</b>	
Flat-to-flat of hexagonal duct (outside), mm	215
Duct wall thickness, mm	3.7
Interassembly gap,mm	7
Number of pins per core subassembly	271
Number of rings (excluding center one)	9
Number of spacers	3
Hydraulic diameter, mm	8.60
Pin pitch (average), mm	12.6
<b>Fuel Pin Geometry</b>	
Total pin length, m	3.34
Fuel pellet outer diameter, mm	7.37
Fuel pellet inner diameter, mm	3.02
Fuel clad thickness, mm	1.0
Fuel pin diameter, mm	9.57

This bundle design is an evolution from the one detailed in [4.1]. Improvements were made in the modeling of the fuel pin gap conductance that resulted in a need to reduce the gap size. Table 4.1 shows that gap size is now 0.1 mm and there is now a central pellet hole of diameter 3.02 mm. The smeared pellet density remains what it was in Ref. 4.1. Ref. [4.1] discusses some of the fuel performance related issues, but Table 4.1 shows that the fuel and cladding temperatures are not violated. At this stage of the design, the design margins to the various design limits are now beginning to be evaluated. The key is still the focus on the passive safety case for the depressurized decay heat removal accidents with concurrent total loss of a/c power. The major limit on the guard containment design backup pressure margin has essentially been established in the design process on the core pressure drop margin, which is a major pressure loss in the primary coolant circuit. One of the key elements in the core pressure drop loss is due to the pressure drop through the core spacers. The margin on the guard containment backup pressure can be related to the number and design of the spacers utilized in the core to provide rigidity to the pin bundle. To study this aspect of the pin bundle design, section 3.3.2 details the pin thermal bowing performance established by the spacer requirements of the thermal-hydraulic performance of the bundle detailed below.

### 3.3.3.2 Analytical Model

A good understanding of the thermal-hydraulic behavior of the EHX loop can be obtained from relatively simple steady-state models that are easy to solve on a computer spreadsheet. In the modeling it is assumed that primary coolant temperature exiting the EHXs is a known value of either 50 or 100° C. This assumption helps to keep the model simple by avoiding the need to include the secondary-side coolant of the EHXs. Since all of the emergency heat exchangers are in parallel, in the model they are assumed to be combined to form one large heat exchanger. For simplicity, in Figure 4.1 the check valves are not shown. Each fuel pin has a region below the core that includes the lower reflector and a region above the core that includes the upper reflector. The core generates a significant amount of heat, but the regions above and below it do not and are modeled as regions that do not generate heat.

There are two basic equations that must be solved to analyze the primary-side EHX loop. The first, the energy balance equation, mathematically requires that the power generated in the core (which is the same as that extracted by the EHXs) is the product of the core temperature rise, the

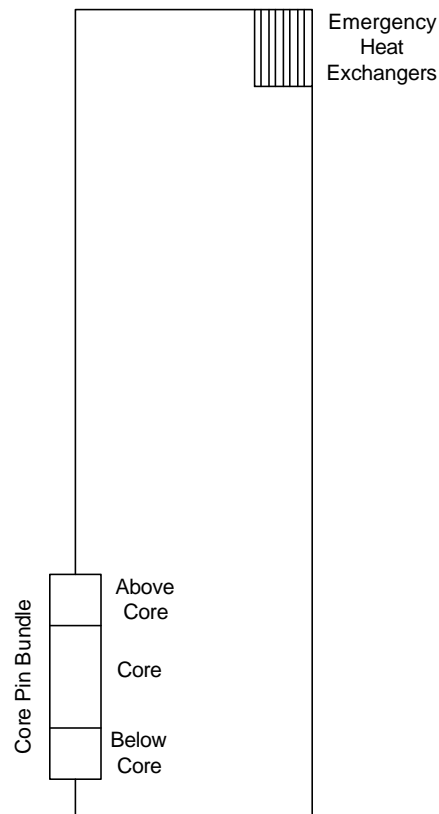


**Fig. 4.1 Emergency Heat Exchanger**

helium flow rate, and the specific heat capacitance of the helium coolant. The second, the momentum balance equation, requires that the friction pressure drop and the buoyancy pressure rise around the loop must be equal. The friction pressure drop is due to hydraulic resistance in the core pin bundle, the parallel EHXs, and connection piping, plena, and valves.

**Table 4.2 Key Parameters**

Length above core, m	1.00
Core length, m	1.34
Length below core, m	1.00
Distance from top of pins to top of EHXs, m	13.45
Pin-bundle hydraulic diameter, cm	0.8604
Pin-bundle flow area, m <sup>2</sup>	7.18
EHX hydraulic diameter, cm	0.3055
EHX length, m	0.30
Combined flow area of EHXs, m <sup>2</sup>	6.011
100% Flow Rate at 2400 MWt, kg/s	1249.4

The hydraulic resistances of the latter three are not modeled. It is assumed that they can be made sufficiently small by making their flow areas sufficiently large. In future analyses these losses can be approximated by increasing the entrance and exit losses of the pin bundle and the EHXs. The buoyancy pressure rise is due to the helium in the downward flow through the EHXs and the piping below it being denser than the upward flow through the core, the pin region above the core, and the reactor regions and the piping above the fuel pins. The greater the vertical separation between the core and the EHXs the greater is the buoyancy pressure rise. Table 4.2 shows some of the key parameters and the values of them that were used in the model.

### 3.3.3.3 Results and Discussion

Figure 4.2 shows the core pin-bundle pressure drop as a function of flow rate with the power held constant at the normal operating power of 2400 MWt. The reactor operating inlet temperature is 480° C and the normal reactor outlet temperature (at 100% power and flow) is 850° C. When the flow rate is at a very small value the reactor outlet temperature, as indicated by the dashed curve in Figure 4.2, is extremely high. The shape of the pressure drop curve between about 10% flow and 200% is what one would expect with pressure drop increasing monotonically with flow. However, a minimum of 2686 Pa is observed at 7.87% flow and the pressure drop rises substantial as much lower flow rates are achieved. In this flow region the flow is laminar and the pressure drop is directly proportion to product of the coolant viscosity and mass flow rate (kg/s) divided by the coolant density. The very high temperatures that result from the low flow rates, cause the viscosity to be relatively high and the density to be relative low. These two together more than compensate for the relatively low flow rate and thereby cause the pressure drop to increase with decreasing flow rate.

This behavior is substantially different from that of liquid flows, where the density is only a weak function of temperature and viscosity increases with decreasing temperature. Thus, for liquids the pressure drop approaches zero as the flow approaches zero. Hence, as Figure 4.2 demonstrates, for the helium gas flow under consideration there is a minimum pressure drop of 2686 Pa at 7.87% flow. All higher pressure drops have two flow solutions, one on each branch of the curve. The temperature at the minimum

pressure drop is denoted as  $T_{\min}$ . Thus, if an experiment were to be performed at temperatures below this value, it is expected that the higher flow solution would be observed and if the experiment were to be performed at temperatures higher than  $T_{\min}$ , the low flow solution would be maintained. Either flow rate, in theory, is stable and maintainable, once achieved. If however the temperature is near  $T_{\min}$  and pressure drop is above, but near the minimum pressure drop, there may be a potential for a perturbation the system to cause an oscillation between the two steady-state operating points.

While the full power behavior of Figure 4.2 has produced some very helpful insights, the region of greatest concern is that at decay power levels. Therefore, many analyses were performed at 0.5% of full power, 12 MWt, or near it. Since the flow rate at full power is 1249.4 kg/s, if the 370° C core temperature rise is to be maintained at 0.5% power, then the corresponding flow rate must be 0.5% of 1249.4 kg/s, or 6.247 kg/s. For convenience, when doing studies at decay heat levels, 6.247 kg/s was defined as 100% flow and 12 MWt was defined as 100% power. Figures 4.3a, 4.3b, and 4.3c employs these new definitions and are

analogous to Figure 4.2, but have much lower pressure drops because of the very low flow range. The reactor inlet temperature was maintained at 480° C. Figures 4.3a, 4.3b, and 4.3c have results for 100% power (12 MWt) and for both 20% above and 20% below 100% power. In both Figures 4.2 and 4.3a the system pressure is 70 bar. The analysis of Figures 4.3a was repeated

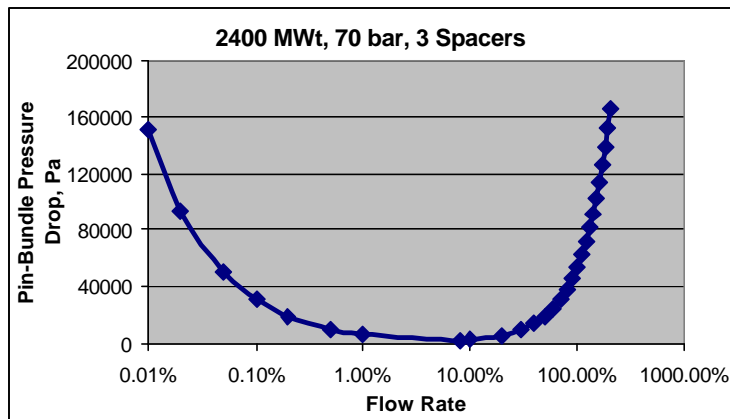


**Figure 4.2 Core Pin-Bundle Pressure Drop  
(Full Power = 2400 MWt)**

for system pressures of 10 and 5 bar, Figures 4.3b and 4.3c, respectively. A comparison of Figures 4.3a, 4.3b, and 4.3c shows that, as expected, the core pin-bundle friction pressure drop is inversely proportional to the system pressure. This is to be expected because the density of the coolant is proportional to the system pressure and the friction pressure drop for laminar flow is inversely proportional to the density of the coolant. Thus, since 5 bar is 1/14<sup>th</sup> of 70 bar, Figure 4.3c can be obtained by using Figure 4.3a and changing the values on the range of the ordinate to 0 to 700 Pa in place of 0 to 50 Pa. In the analyses of Figures 4.3a, 4.3b, and 4.3c, it was assumed that the core pin-bundle had three grid spacers. Since the flow is laminar, the increase in pressure drop due to the spacers is relatively small and several more spacers could be used without a substantial change in the results.

Figures 4.4a, 4.4b, and 4.4c are the buoyancy pressure rise counterparts of Figures 4.3a, 4.3b, and 4.3c, respectively. The outlet temperature of the EHXs, which is the inlet temperature to the reactor, is assumed to be 100° C for these buoyancy pressure rise calculations. Thus, most of the cold leg, which contains the EHXs, is at this relatively

cold temperature and most of the hot leg, which contains the reactor core, is at the reactor outlet temperature. The fluid density in the cold leg is therefore significantly greater than that in the hot leg. The resultant difference in the weights of these two columns of helium produces the buoyancy force that drives the flow around the loop. Figures 4.4a, 4.4b, and 4.4c show that the gravity pressure rise increases with decreasing flow rate and approaches an asymptote as zero flow is approached. This occurs because as the flow rate decreases, the temperatures in the hot leg increase. Since density is inversely proportional to absolute temperature, a very low flow rate results in very high helium temperatures and as the flow rate approaches zero, the density of the reactor outlet coolant asymptotically approaches zero.

A comparison of Figures 4.4a, 4.4b, and 4.4c shows the effect of system pressure. Decreasing the system pressure decreases the density everywhere in the loop proportionally. Since the gravity pressure rise is directly proportional to the density, decreasing the system pressure by a factor of 14 reduces the gravity pressure rise by a factor of 14. Thus, Figure 4.4c can be produced by just changing the scale Figure 4.4a so that its range is 0 to 100 Pa instead to the 0 to 1400 Pa of Figure 4.4c.

The loop flow rate for natural circulation flows is established where the friction pressure drop and the gravity pressure drop are equal. Figures 4.5a, 4.5b, 4.5c, and 4.5d are examples where a core pin-bundle friction pressure drop and its corresponding gravity pressure rise curve are plotted on the same graph so that the points where the two are equal can be observed. Two inconsistencies between the pairs of curves in each of these four figures should be noted. First, the friction pressure drop curves include only the pin pressure drop, but not the rest of the hydraulic resistance around the loop. Second, the reactor inlet temperature is 480° C in the friction pressure drop calculations, rather than the 100° C of the gravity pressure rise ones. In spite of these flaws, which make the precise numerical results inaccurate, Figures 4.5a, 4.5b, 4.5c, and 4.5d are suitable for demonstrating a concept. Figure 4.5a and 4.5c each have two intersection points, while Figure 4.5b and 4.5d have none. Thus, the Figures 4.5a and 4.5c each have two possible flow solutions and Figure 4.5b and 4.5d have none. Increasing the system pressure in Figure 4.5b and 4.5d would lower the friction curve and raise the gravity curve. This could be done in such away as to allow the two curves to meet tangentially at a single point, or if a greater pressure were used there would be two solutions, as in the Figures 4.5a and 4.5c.

Studying the friction and gravity components of natural circulation separately is informative and provides useful insights into the behavior of the EHX loop. However, both components can be included in a single mathematical model that can be used to show the relationship between reactor coolant outlet temperature and system pressure for various decay power levels, Figure 4.6. Figure 4.6 reverts back to defining 100% power to be 2400 MWt. For this analysis the outlet temperature of the EHXs was assumed to be 50°C and the hydraulic resistance of the EHXs was included in the calculations. Key parameters for this calculation are provided in Table 4.2, above. Decay power levels of 0.25, 0.5, 1.0, and 2.0% are considered. The lowest temperature on each curve was arbitrarily selected to be 450°C. For each power level it is observed that as the system pressure is reduced the coolant outlet temperature increases until the point where the

minimum pressure is reached. This point is represented as the highest temperature on shown each curve. As indicated in Figures 4.5a and 4.5c above, for each system pressure there can be two solutions—one with high flow and a low coolant outlet temperature and another with a low flow and a high coolant outlet temperature. Thus, each curve in Figure 4.6 could be extended to higher temperatures by including the high temperature (low flow) solutions. If this were done, for each power level curve there would be two temperatures for each pressure above the minimum. Figure 4.6 also shows that, depending on power level, a reduction of only about 1 to 4 bars in system pressure can cause the outlet coolant temperature to increase by 1000°C or more.



Figure 4.3a  
70 bar

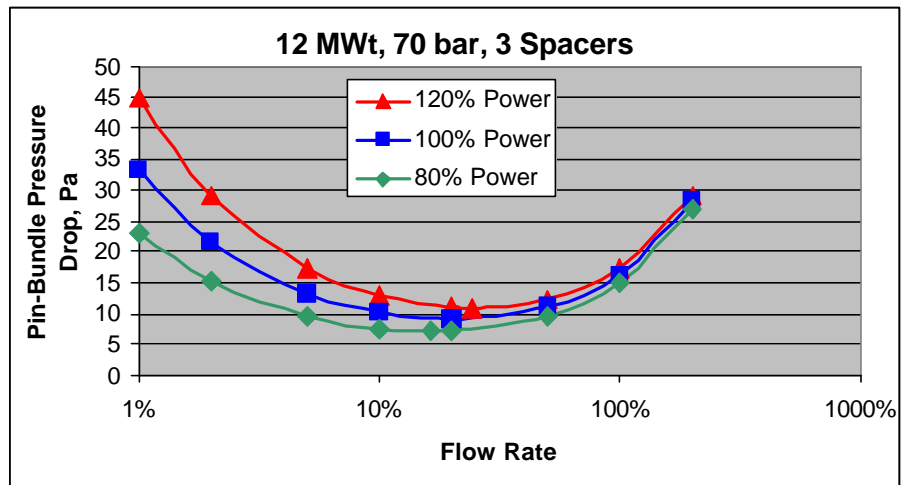


Figure 4.3b  
10 bar

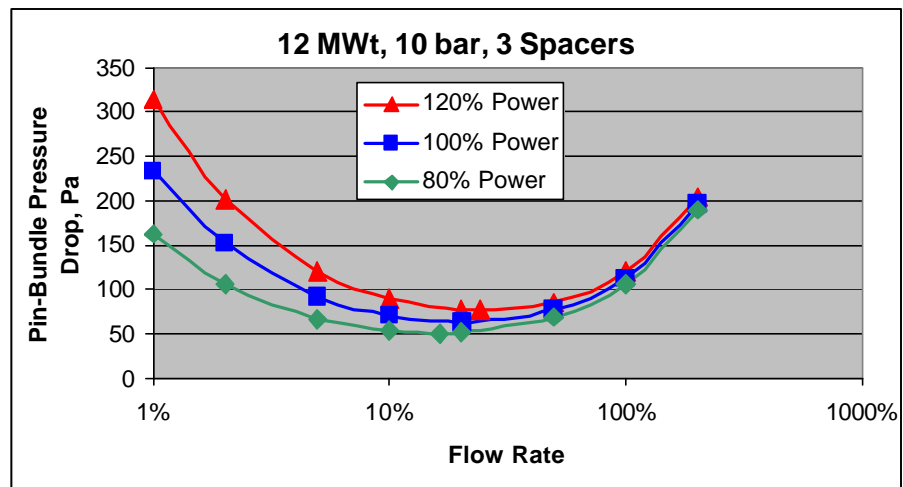
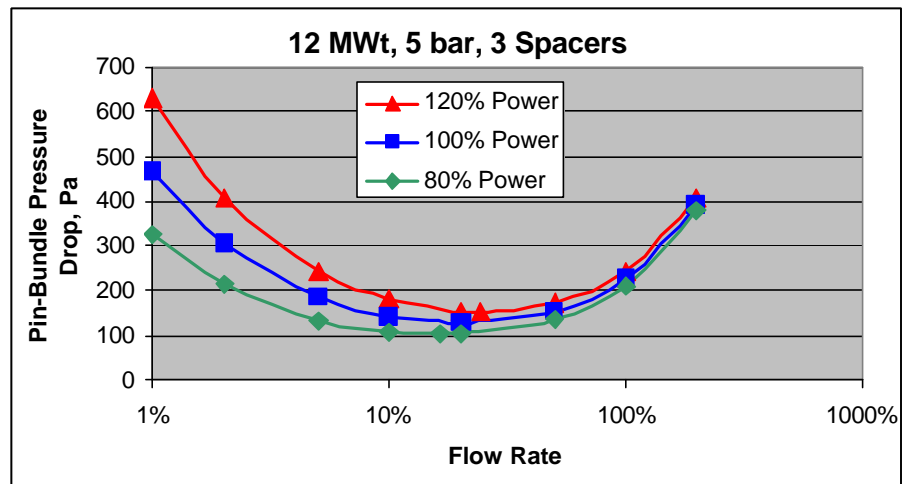
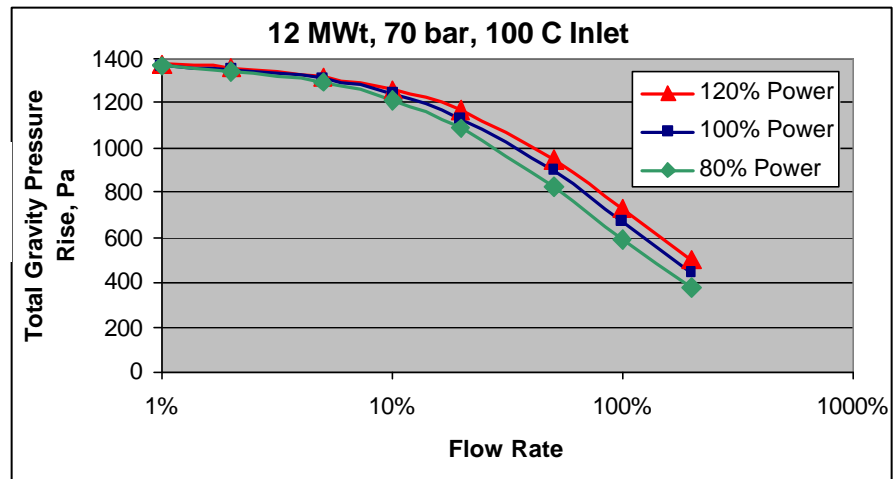


Figure 4.3c  
5 bar



Figures 4.3a, 4.3b, and 4.3c Core Pin-Bundle Pressure Drop (Full Power = 12 MWt)

**Figure 4.4a**  
**70 bar**



**Figure 4.4b**  
**10 bar**

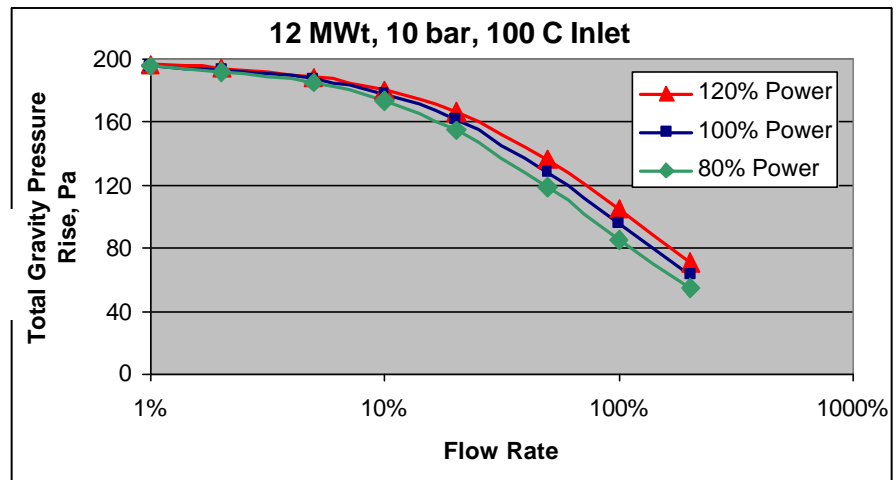
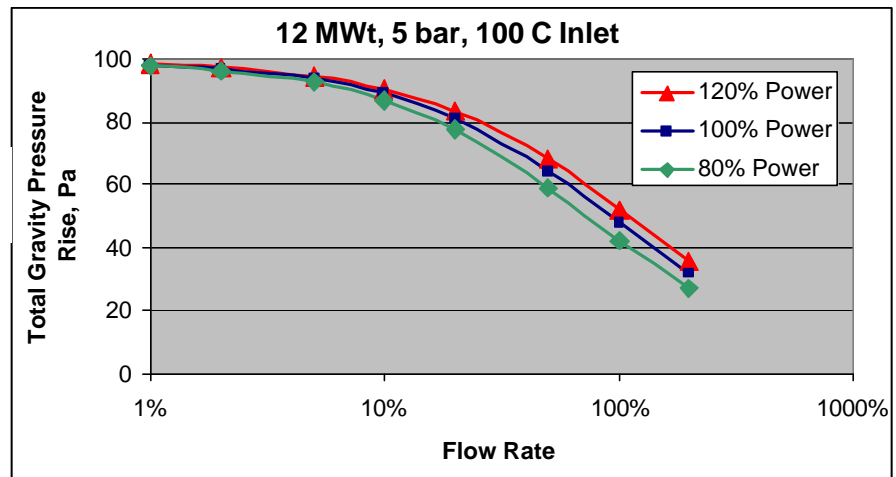


**Figure 4.4c**  
**5 bar**



**Figures 4.4a, 4.4b, and 4.4c EHX-Loop Gravity  
Pressure Rise (Full Power = 12 MWt)**

**Fig. 4.5a**

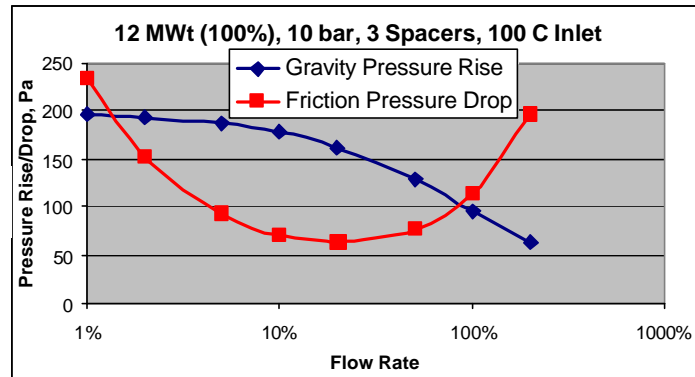


**Fig. 4.5b**

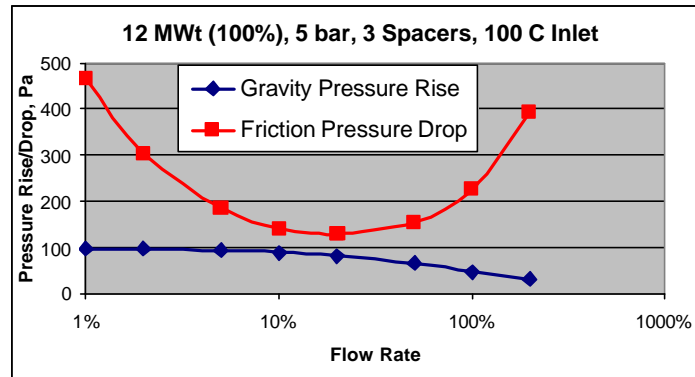


**Fig. 4.5c**

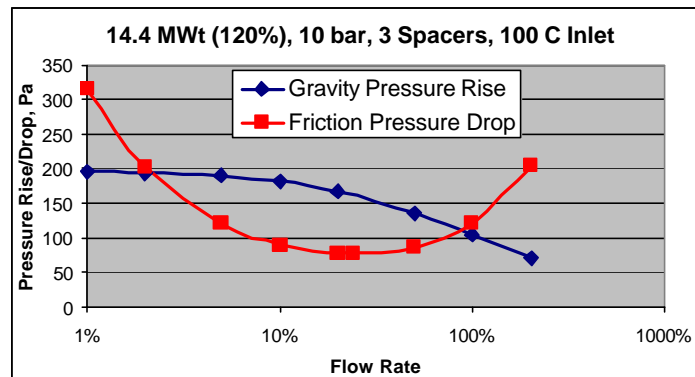
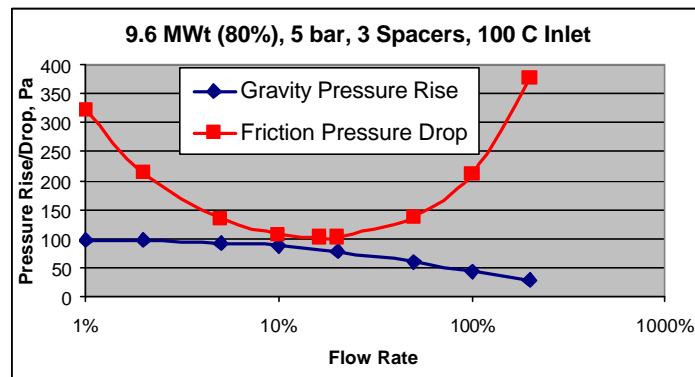


**Fig. 4.5d**



**Figures 4.5a, 4.5b, 4.5c, and 4.5d Equating Friction Pressure Drop with Gravity Pressure Rise (Full Power = 12 MWt)**

### 3.3.3.4 Conclusions

The behavior of natural circulation in gas-cooled system can have some unusual behaviors that are not present in liquid-cooled systems. In particular, low flows can result in *increasing* friction pressure drop with decreasing flow rate. Because of this behavior, a given system pressure drop and system pressure may have two steady-states—one at a relative high flow rate with a relatively low core outlet temperature and another at a relatively low flow rate with a relatively high core outlet temperature. It is also possible that if the system pressure is too low there may be no steady-state condition. Thus, in designing natural circulation decay heat removal systems for GFRs it is important to be able to guarantee that the system pressure in the EHX loop will always be maintained at a sufficiently high value while this system is in use.

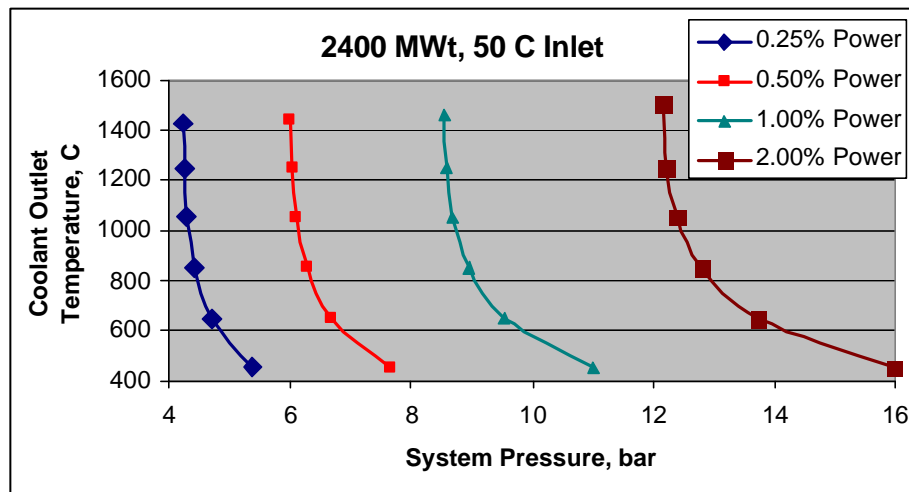


Figure 4.6 Core Coolant Outlet Temperature vs. System Pressure

## 3.4 Guard Containment CFD Analysis

Under the auspices of the CEA Cadarache/ANL-US I-NERI project a comprehensive investigation has been made of improvements to the Gen-IV GFR safety case over that of the GCFR safety case twenty five years ago. In particular, it has been concluded and agreed upon [1] that the GFR safety approach for the passive removal of decay heat in a protected depressurization accident with total loss of electric power needs to be different from that taken for the HTRs. The HTR conduction cooldown to the vessel wall boundary mode for an economically attractive core is not feasible in the case of the GFR because the high power densities (100kW/1 compared to 5 kW/1 for pebble bed thermal reactor) require decay heat fluxes well beyond those achievable by the heat conduction and radiation heat transfer mode. A set of alternative novel design options has been evaluated for potential passive safety mechanisms unique to the GFR. In summary, from a technological risk viewpoint and R&D planning, the option which has been identified is the block/plate-based or a pin-based reactor with a secondary guard containment/vessel around the primary vessel to maintain the primary system pressure at a high enough level

which would allow primary system natural convection removal of core generated decay heat to be effective. Dedicated emergency decay heat exchangers would have to be connected in a “failure-proof” configuration to the primary system and have natural convection capability all the way to the ultimate heat sink.

What has been collaboratively agreed upon and selected for further development is the natural convection option with a block/plate or pin type derated core and a hybrid passive/active approach.[2] The guard containment will be utilized but it will be sized for an LWR containment range backup pressure (5-7 bars) with an initial pressure of 1 bar. The assessment has shown that a significantly higher back pressure is required for total natural convection driven removal of significant decay heat levels at GFR target power densities. The lower back-up pressure, plus whatever natural convection is available at this pressure, will be utilized to significantly reduce the blower power of the active DHR system sized to remove 2-3% decay power. The objective is to be able to have such low power requirements so that power supplies such as batteries without the need for startup, can be utilized. This lower back-up pressure should be sufficient to support natural convection removal of 0.5% decay heat which occurs at ~24 hrs. So there should be no more need for active systems/power supply after the initial period of one day. Furthermore, since there will be a decay of the after-heat from 2-3% to 0.5% in this time period, credit should be taken in probability space for loss of active systems during the 24 hours. The safety approach will then be a probabilistic one. In the future discussions with the regulatory authorities the approach which will then be taken is that this class of decay heat accidents should be treated in combination with the PRA rather than solely through deterministic calculations. Work is now ongoing in the U.S.-France I-NERI GFR project to further evaluate this hybrid passive/active approach to heat removal for depressurized decay heat accidents.

The objective of the analysis documented in this report is to provide information on local and global temperature, pressure and flow distributions in the guard containment, during steady state, and reactor vessel depressurization conditions due to a small break in the reactor vessel bottom control rod drive system. This is for the 2400 MWt plant option. The results should lead to improved guard containment designs and enhanced margin for safety criteria.

### **3.4.1 2400 MWt Plant Layout**

For the 2400MWt GFR core, the Guard Containment (GC) option with a 5bar containment pressure in a pre-stressed concrete containment was selected. The volume and cost analysis described in [2] showed that, at these lower pressures, the GC option has a lower cost than the corresponding pre-stressed concrete reactor vessel (PCRV), which is similar to that used for the FSV reactor, and planned for the GCFR design. This GC option is shown in elevation view in Figure 1. The pre-stressed concrete containment is 36m in diameter and 44m high (other dimensions are also indicated on the figure). The PCU is located outside the Guard Containment, and the GC penetrations for connecting to the PCU and SCS ducts must be separated 4.5m vertically and 1m horizontally to meet ASME code. Use of a smaller spacing leads to a thicker GC wall, and to fabrication problems.

The layout of the 2400MWt direct cycle GC option is given in Figures 1 and 2, which shows the location of the four PCU and four SCS vessels. The overall plant dimensions are driven by the reactor vessel (RV) and PCU requirements. In turn the RV radial dimensions are based upon the core diameter, and the reflector and shielding thicknesses needed. The RV height is based on the SCS height and ducting, the IHX height and location, the core height, the PCU cross vessel location, and refueling reach concerns.

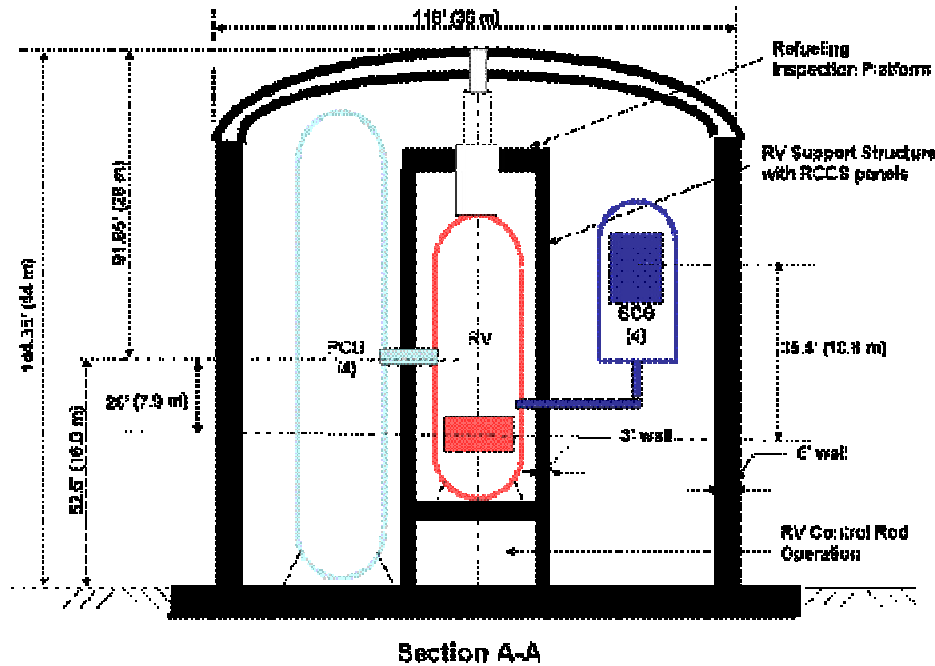
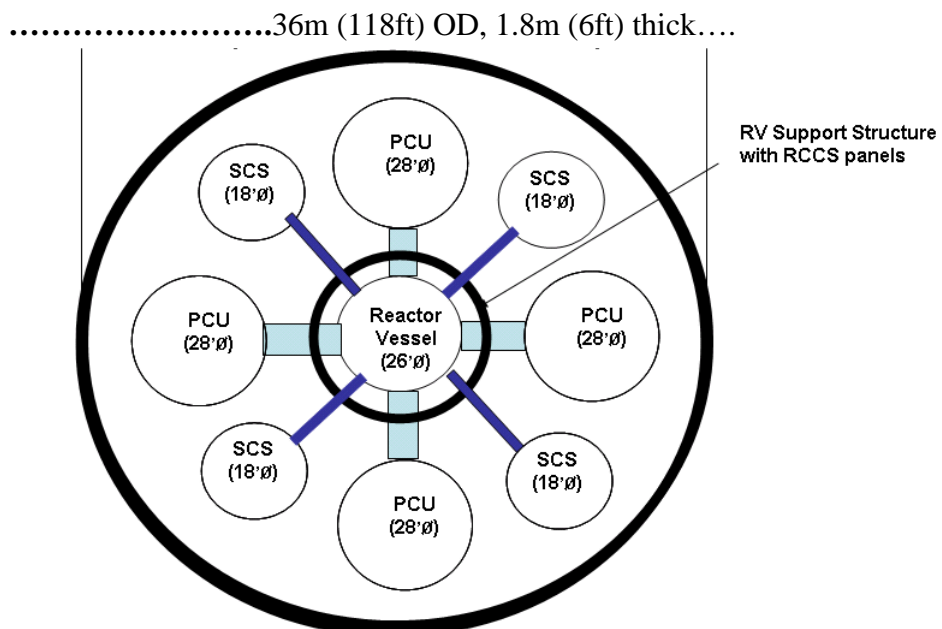


Fig. 1. 2400MWt Guard Containment Elevation View



### 3.4.2 Decay Heat Accidents

A series of transient analysis using the system code RELAP5/ATHENA has been performed [2] to assess decay heat removal by natural circulation cooling under postulated accident conditions. The analysis is for a helium cooled reactor of pin core design with a power density of 100 W/cc and a thermal power of 2400 MW. The objective is to ensure that the maximum fuel temperature remains within acceptable limits ( $< 1600^{\circ}\text{C}$ ) following a depressurization accident with scram and total loss of AC power. The break is a postulated small one inch leak in the primary system boundary.

The removal of decay heat from the core will follow the initiation of the depressurization accident in two steps. Initially, heat will be removed by a combination of flow coastdown due to inertia of the power conversion system and system depressurization caused by coolant flowing out of the break from the primary system. Following this step a self-sustaining method for long-term heat removal of the core will be required. A passive mode of heat removal relying on natural circulation cooling is investigated in this report. An emergency heat exchanger loop outside the reactor vessel will transfer energy from the reactor to an ultimate heat sink located outside the guard containment. By the opening of a check valve inline with the emergency heat exchanger a natural circulation flow path is established through the core and between the upper plenum and downcomer of the reactor vessel. Radiative heat transfer has also been included in the model to account for the exchange of thermal energy between heat structures by radiation. In order for natural circulation cooling to function efficiently the primary system and the containment will need to be pressurized to ensure a sufficiently high coolant density. This is accomplished by having a guard containment structure around the primary system. The main objective of the RELAP5 accident analyses is to evaluate the effects of guard containment back pressure on the effectiveness of natural circulation cooling.

A RELAP5 model of the reactor system has been constructed to address different parametric effects that influence the steady state and transient behavior of the pin core under natural circulation cooling at decay heat power levels. The model consists of two power conversion unit loops, an emergency heat exchanger loop with its heat sink, and a guard containment surrounding the primary system. The actual power plant will be constructed using four power conversion loops. However, in the RELAP model three loops are combined into one large loop (1800 MW), and one loop (600 MW) is isolated in order to correctly model the depressurization dynamics, since the leak flow will emanate from only one of the power conversion loops. Transient history results for break flow mass rate and thermodynamic conditions were obtained with this RELAP5 model for the selected depressurization accident. These histories together with boundary temperatures on the vessel and the DHR were provided to the CFD calculation as forcing functions. The results from the CFD analyses of the guard containment condition and flow distribution patterns will provide insight and guidance for the RELAP5 lumped parameter nodalization of the guard containment. This symbiosis should lead to a better understanding of the system pressure transient.

### 3.4.3 Guard Containment CFD Model

The GFR containment is a very large structure, having a radius of 18 m and a height of 44 m. In addition to the reactor vessel, there are many other components inside the containment. The largest ones are four Power Conversion Units (PCUs), four Shutdown Cooling Systems (SCSs), the Reactor Cavity Cooling System (RCCS), and concrete structures that support the reactor vessel. The CFD simulation of this large system is quite challenging. Especially challenging is the analysis of a reactor vessel depressurization transient. This involves spatial and time scales that vary by many orders of magnitude. To meet the challenge, the problem is simplified by neglecting geometrical features whose impact on the fluid dynamics of the system is small, and by using boundary conditions that remove large variations that occur in small space regions and for a short time. A simplified STAR-CD CFD model of the guard containment was developed based on the gross 1/8 symmetry of the containment space. Figure 3 shows the grid of the in-containment fluid space on a horizontal (x-y) plane at a height where the inner and outer cavities communicate. Figure 4 shows a view of the model from the y+ direction. The yellow color represents the containment walls. The green represents the inner cavity, and the purple the outer cavity. The cylindrical wall is the outer wall of one half of a PCU unit. The inner cavity has a RCCS surrounding the reactor vessel with a number of “windows” about the reactor head to allow communication with the outer cavity. The support structure is a concrete cylinder between the two cavities. Figure 5 shows a view of the model from the y- direction. The cylindrical wall represents the outer wall of one half of an RCCS unit. The figure also shows the communication “window” between the inner and outer cavity. The outer wall of the reactor vessel defines the inner boundary of the inner cavity. Finally, Figs. 6 & 7 show vertical cutaways through the PCU and the DHR cooler. The center lines are through the reactor vessel in both figures. The reactor vessel can be seen in the silhouette outline sitting on top of the control rod room. The lighter outside boundary is the concrete guard containment.

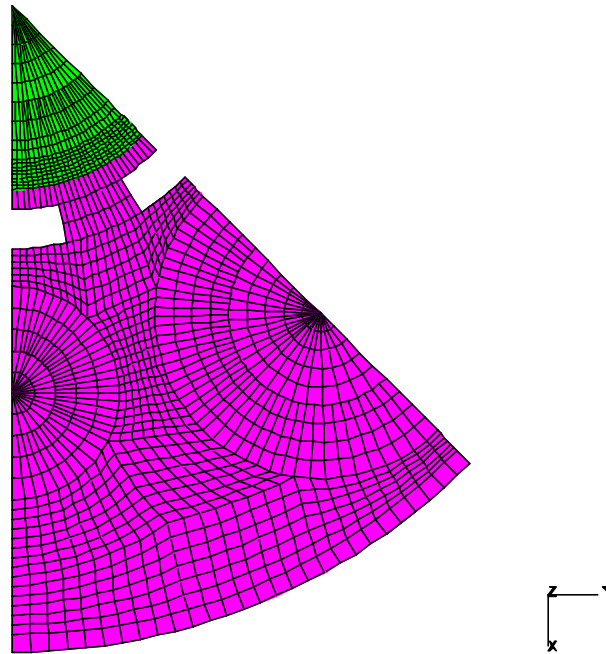


Fig. 3. Grid on A Horizontal Cross-Section



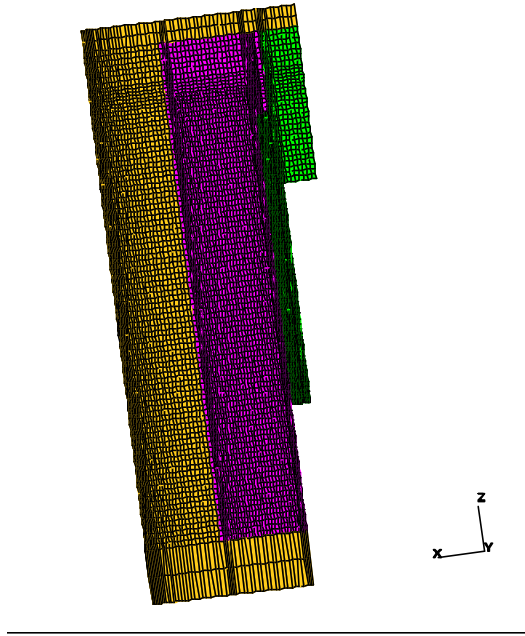


Fig. 4. Grid View from y+

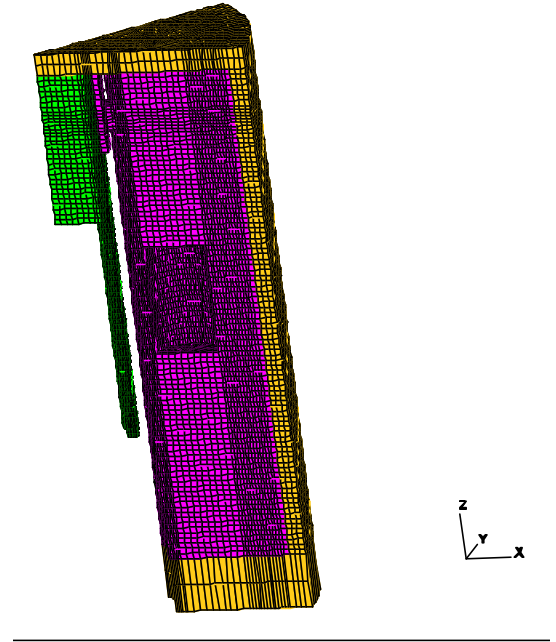


Fig. 5. Grid View from y-

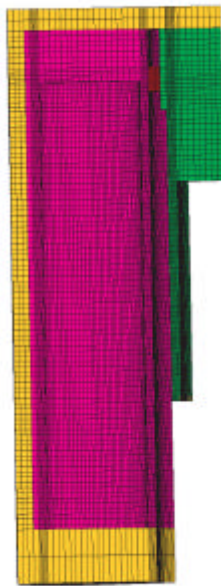


Fig. 6. Vertical Cutaway Though the PCU

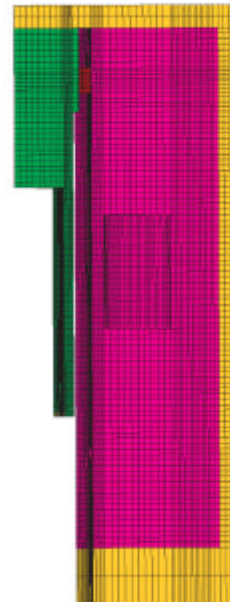


Fig. 7. Vertical Cutaway Through the DHR Cooler

### 3.4.4 Long Term Steady State Analysis

A steady state analysis was performed at the conditions prevailing at the end of the depressurization transient as determined by the RELAP analysis. This is the long term steady state as the accident reaches a quasi-equilibrium. The temperature boundary conditions used for this analysis are: 303 ° K (30 °C) on the outer wall of the containment; 335 ° K (62 °C) on the outer wall of the RCCS unit; 338.6 ° K (65.6 °C) on the outer boundary of the inner cavity, the boundary of the “window”, the inner boundary of the outer cavity, and the bottom boundary of the inner cavity; 490 ° K (217 °C) on the lower 10.6 m of the reactor vessel wall; 520 ° K (247 °C) on the upper section and on the top of the reactor vessel; and an adiabatic condition on the outer wall of the PCU unit. An emissivity of 0.7 was used for all radiating surfaces. The containment atmosphere is composed of a mixture of nitrogen (75% mol fraction) and helium (25% mol fraction) at a pressure of 6 bar which within the range of 5-7 bar.

The model did not converge to a steady state. This may be due to the very weak coupling of the natural convection flows in the inner and outer cavity through the small “window” in the upper part of the containment space.

Figure 8 shows the temperature distribution in the containment fluid (nitrogen-helium mixture). As expected the hotter region is the area around the vertical side of the reactor vessel, which reaches a maximum temperature of 412 ° K (139 °C). Most of the outer cavity has a temperature of about 348 ° K (75 °C). Figure 9 shows the temperature of the containment wall. The maximum temperature occurs on the inner surface above the reactor vessel, which reaches a temperature of 350 ° K (77 °C).

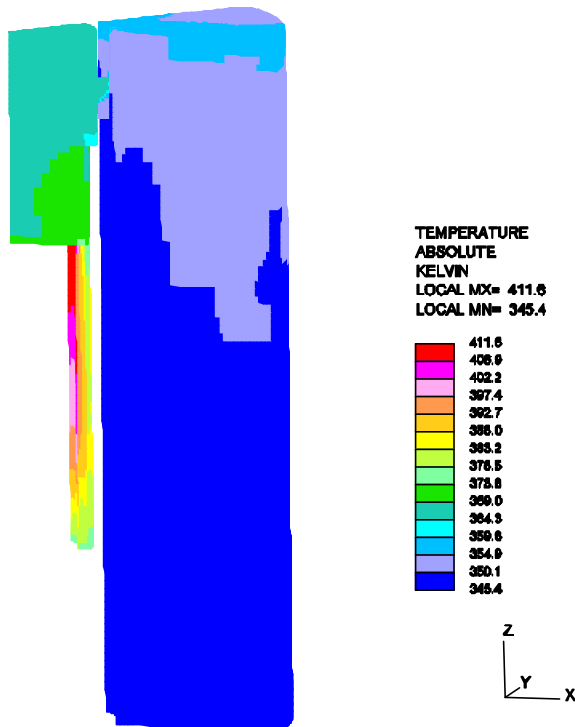


Fig. 8. Fluid Temperature  
Containment

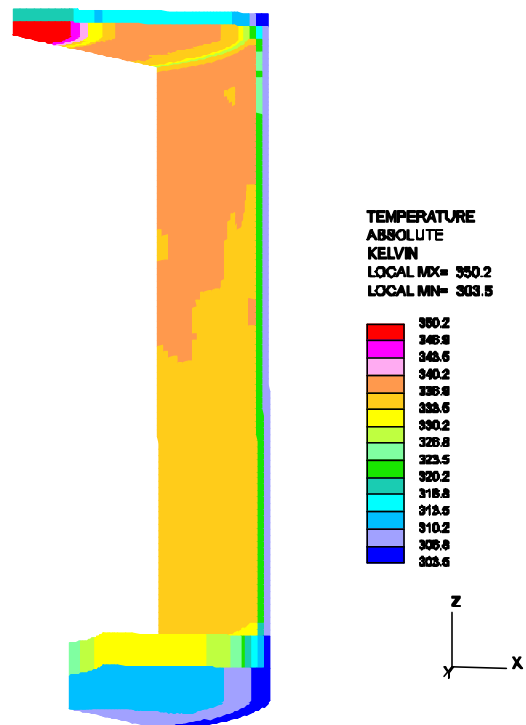


Fig. 9. Temperature of  
Structure

Figures 10 and 11 are the side-by-side mirror reflection of Figures 6 and 7 and they show the flow distribution patterns in these areas at the long term steady state. Figures 12, and 13 show the flow on two vertical planes in the section of the inner cavity above the reactor vessel. Its main feature is two large vortices rotating in opposite directions. As a continuation of Figure 12, Figure 14 shows the main flow pattern in the inner cavity below the top of the reactor vessel: the gas flows up along the hot wall of the reactor vessel and down along the cold outer wall of the inner cavity.

Figure 15 shows the flow through the “window” that provides communication between the inner and outer cavity. Fluid flows from the hot inner cavity to the cold outer cavity in the upper section of the window, while cold gas from the outer cavity flows to the inner cavity through the lower section of the window. The air velocities in the outer cavity are lower than in the inner cavity and the flow patterns are quite complex. Figure 16 shows the flow on a vertical plane passing through the axis of the outer cavity. Figures 17 to 20 show the flow in sections of the outer cavity.



Fig. 10. Flow Distribution in DHR Cutaway

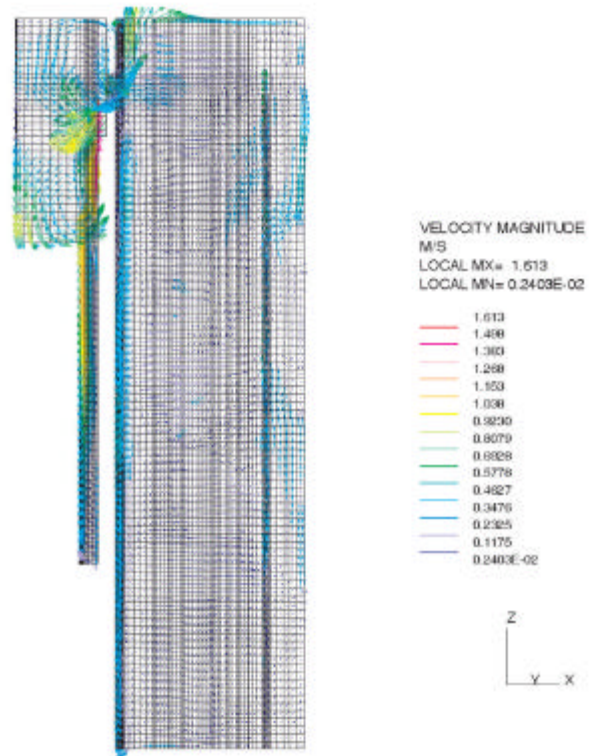


Fig. 11. Flow Distribution in PCU Cutaway

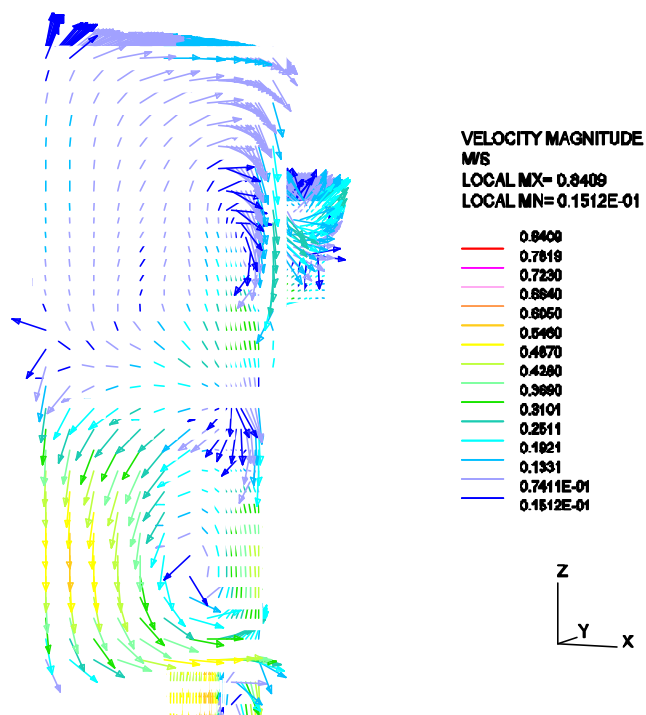


Fig. 12. Flow in the Inner Cavity, Above the Reactor Vessel (Section 1)

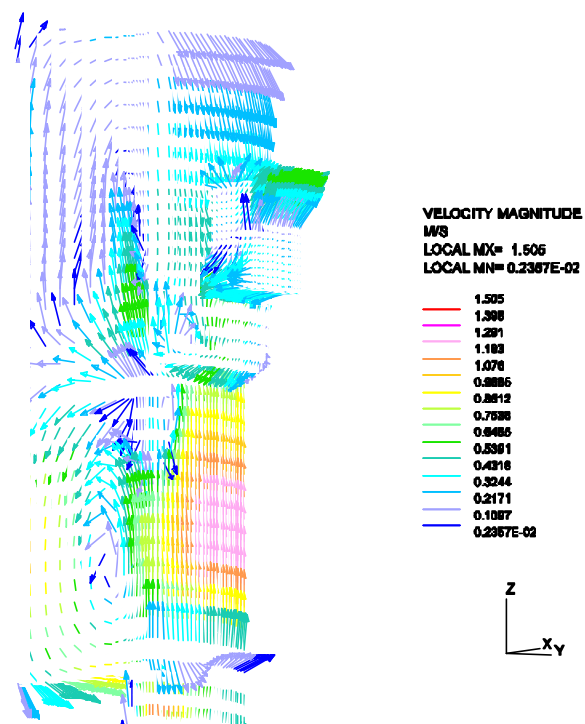


Fig. 13. Flow in Inner Cavity, Above the Reactor Vessel (Section 2)

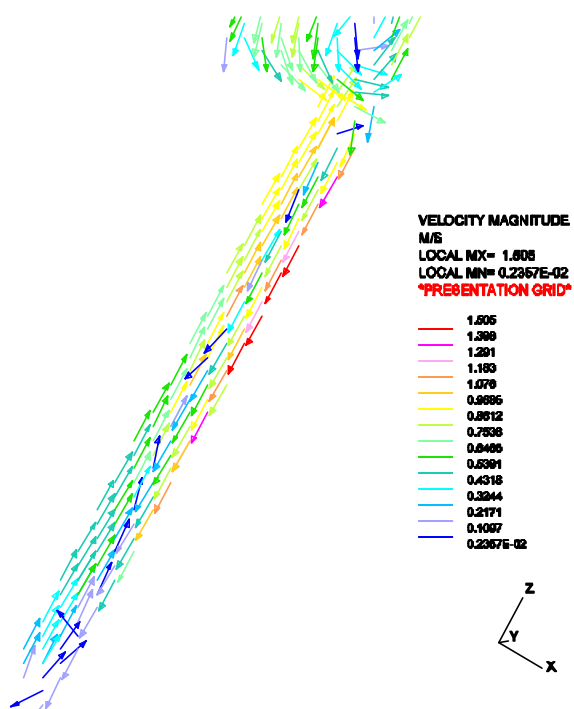


Fig. 14. Flow in The Inner Cavity, Below The Top of the Reactor Vessel

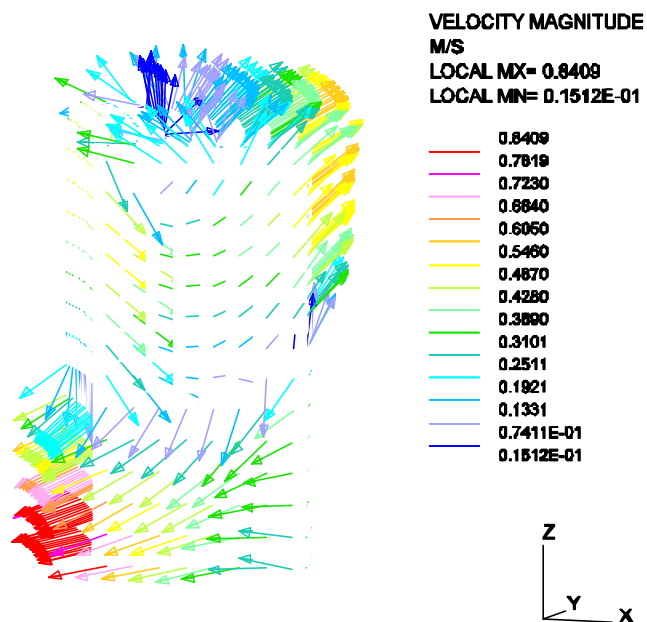


Fig. 15. Flow Through the “window”

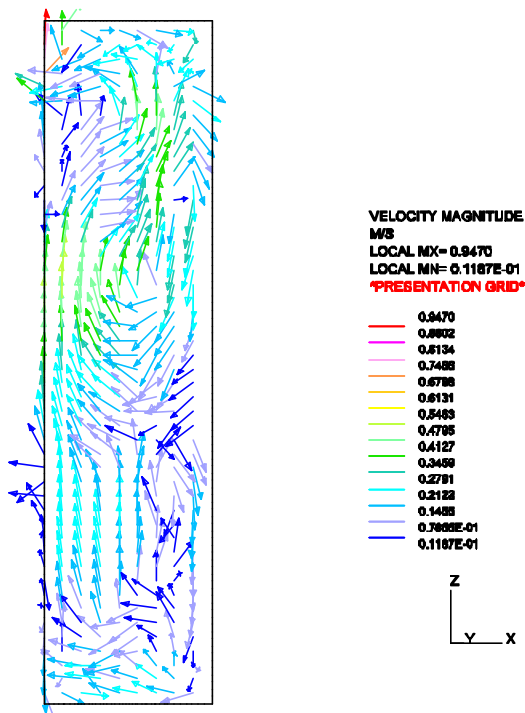


Fig. 16. Flow in the Outer Cavity on A Vertical Plane Passing through the Cavity Axis of Symmetry

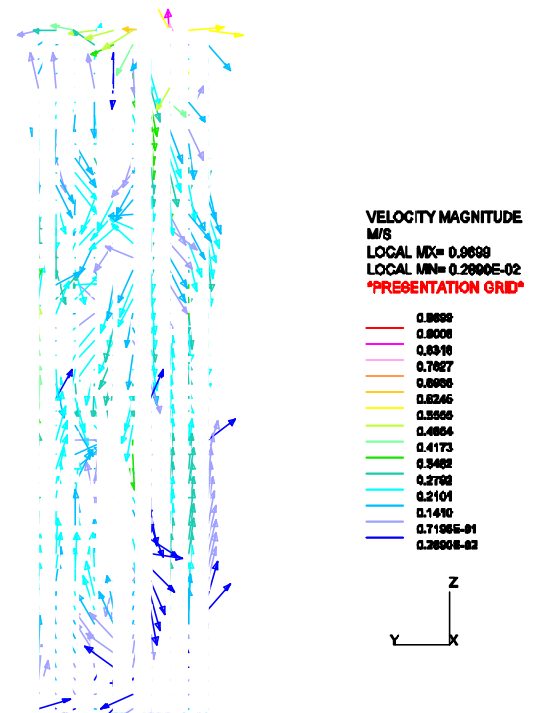


Fig. 17. Flow in the Outer Cavity (view from x-)

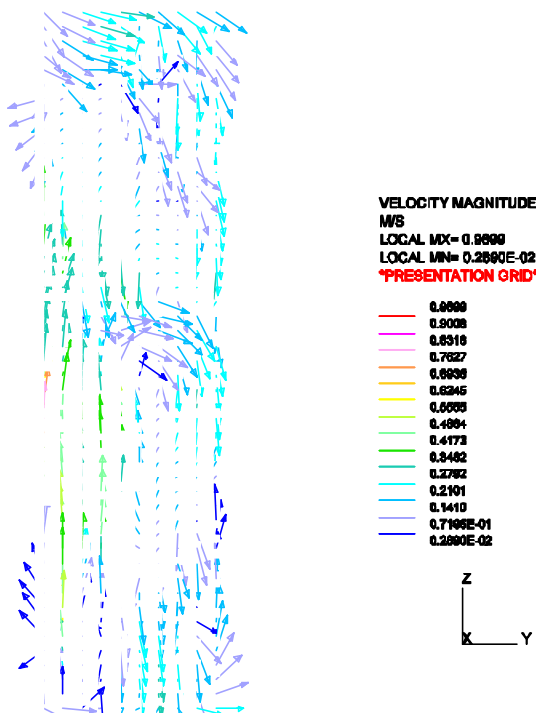


Fig. 18. Flow in the Outer Cavity (view from x+)

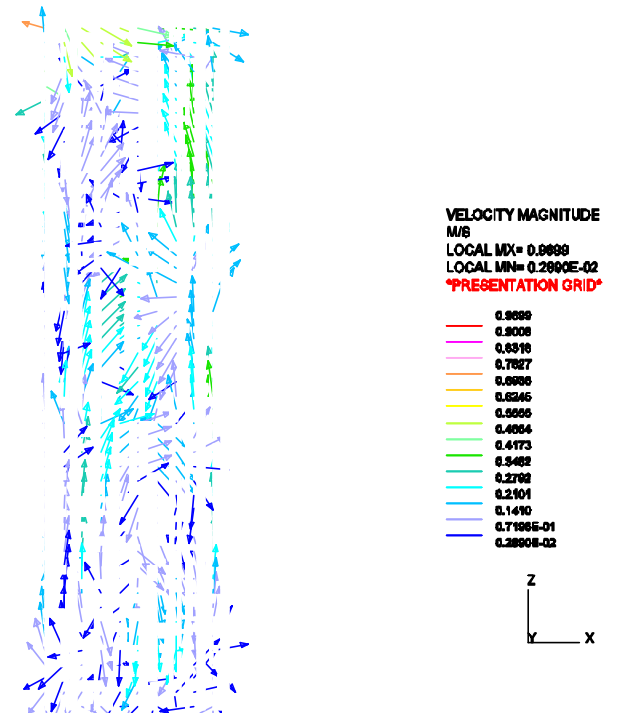


Fig. 19. Flow in the Outer Cavity (view from y-)

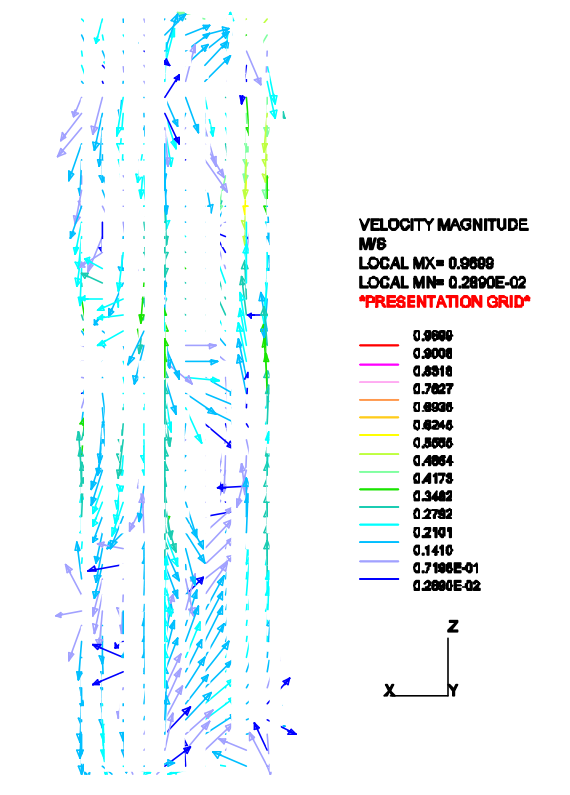


Fig. 20. Flow in the Outer Cavity (flow from y+)

Table 1 gives the convective heat flux for each inner boundary of the system, and Table 2 gives the radiative heat flux for the same boundaries.

Table 1. Average Convective Heat Flux,  $w/m^2$

Boundary Surface	Heat Flux
Reactor vessel – lower vertical wall	1884.30
Reactor vessel – upper vertical wall	3137.00
Reactor vessel top	4444.50
Inner surface of containment top – inner cavity	-32.00
Inner cavity floor	-261.90
Inner cavity vertical outer boundary	-886.00
Inner vertical surface of outer containment wall	-33.29
Inner surface of containment top – outer cavity	-61.10
Containment floor – outer cavity	-18.82
Inner boundary of outer cavity	-107.06
Vertical surface of SCS	-98.12
Top of SCS	-71.45
Bottom SCS	-60.66

Table 2. Radiative Heat Flux, w/m<sup>2</sup>

Boundary Surface	Heat Flux
Reactor vessel – lower vertical wall	1418.70
Reactor vessel – upper vertical wall	1937.90
Reactor vessel top	2232.20
Inner surface of containment top – inner cavity	-22.19
Inner cavity floor	-674.49
Inner cavity vertical outer boundary	-898.39
Inner vertical surface of outer containment wall	-7.50
Inner surface of containment top – outer cavity	24.28
Containment floor – outer cavity	-1.11
Inner boundary of outer cavity	-25.53
Vertical surface of SCS	-40.22
Top of SCS	-60.44
Bottom SCS	-37.10
Window	10.32
PCU top	12.57
PCU side	20.46

### 3.4.5 Transient Analysis

The objective of this analysis is to simulate a reactor vessel depressurization transient driven by a small break in the reactor vessel.

For an isentropic flow,

$$h_v = h + \frac{1}{2}u^2 \quad (1)$$

where

$h_v$  = enthalpy of the gas in the reactor vessel (the subscript v denotes properties of the

gas in the reactor vessel)

$h$  = enthalpy of the gas at the break location

$u$  = gas velocity at the break location

from

$$h = c_p T$$

where  $c_p$  is the specific heat under constant pressure, and  $T$  is the gas temperature, Eq. (1) gives

$$h_v - h = c_p(T_v - T)$$

and

$$u = \sqrt{2c_p(T_v - T)} \quad (2)$$

For an ideal gas,

$$T = \frac{p}{Rr}$$

$$c_p = \frac{gR}{g-1}$$

$$g = \frac{c_p}{c_v}$$

where  $c_v$  is the specific heat under constant volume, and Eq. (2) gives

$$u = \sqrt{\frac{2g}{g-1} \left( \frac{p_v}{r_v} - \frac{p}{r} \right)} \quad (3)$$

where

$p$  = pressure at the break location

$r$  = density at the break location

$R$  = the ideal gas constant

For isentropic flow, the density  $r$  at the break is given by

$$r = r_v \left( \frac{p}{p_v} \right)^{\frac{1}{g}} \quad (4)$$

If the pressure in the containment is lower than the critical pressure  $p_c$ , where

$$p_c = p_v \left( \frac{g+1}{2} \right)^{\frac{g}{1-g}} \quad (5)$$

then the flow is sonic and the pressure  $p$  used in Eqs. (3) and (4) is set equal to  $p_c$ , otherwise  $p$  is the pressure of the containment in the neighborhood of the break. The flow rate,  $w$ , at the break is

$$w = A r u \quad (6)$$

where  $A$  is the area of the break.

Because of the depressurization, the pressure in the reactor vessel changes with time. Conservation of energy in the reactor vessel gives:

$$dE/dt = \text{enthalpy out} + \text{kinetic energy out} \quad (7)$$



where  $E$  is the internal energy of the gas in the reactor vessel. The internal energy  $E$  is

$$E = e\gamma V = c_v T \gamma V$$

where  $e$  is the specific internal energy and  $V$  is the reactor vessel volume. For an ideal gas

$$\gamma = p/RT$$

and

$$E = c_v p V / R = \frac{pV}{g-1}$$

The reactor vessel volume is constant and

$$\frac{dE}{dt} = \frac{V}{g-1} \frac{dp_v}{dt} \quad (8)$$

The enthalpy out is

$$H_{out} = -A\gamma u(e + p/\gamma) = -\gamma u(\gamma e + p) \quad (9)$$

and for

$$e = c_v T, \quad \gamma = p/RT, \quad c_p - c_v = R, \quad \gamma = c_p/c_v$$

Eq. 9 gives

$$H_{out} = -A\gamma p \frac{g}{g-1} \quad (10)$$

Equations 8, 9, and 10 give

$$\frac{V}{g-1} \frac{dp_v}{dt} = -Au \left( \frac{g}{g-1} p + \frac{1}{2} \rho u^2 \right) \quad (11)$$

Conservation of mass in the reactor vessel gives

$$V \frac{d\rho}{dt} = -A\rho u \quad (12)$$

Equations (3), (4), (5), (11), and (12) provide the boundary conditions for the pressurization transient of the containment that is driven by the depressurization of the reactor vessel.

Because coupling of the above equations with STAR-CD requires quite some effort, it was decided to use instead information generated by a RELAP analysis of the same transient. This information includes helium mass flow rate, temperature, pressure and internal energy at the break location. Because in this analysis a detailed simulation of the conditions in the neighborhood of the break is not of interest, and because a combination of such an analysis with the analysis in the very large containment space is computationally very demanding, the helium flow into the containment is simulated as an injection of helium in the bottom layer of computational cells adjacent to the reactor vessel. Because the cross-sectional area of these cells is much larger than the area of the break (one square inch), to simplify the analysis, the temperature and pressure of the injected gas are set equal to their stagnation values,  $T_{in}$  and  $p_{in}$ , respectively, that is:

$$T_{in} = T + \frac{u^2}{2c_p} \quad (13)$$

$$p_{in} = p \left( \frac{T_{in}}{T} \right)^{\frac{g}{(g-1)}} \quad (14)$$

where  $T$ ,  $p$ ,  $u$  and  $c_p$  are the temperature, pressure, velocity and specific heat at the break, and

$$\gamma = c_p/c_v$$

The velocity  $u$  is computed from the mass flow rate and the pressure and temperature at the break provided by the RELAP output.

A user subroutine was written that converts the RELAP output into STAR-CD input, and a STAR transient model was developed.

To start the transient analysis, a steady state analysis was performed with reactor vessel and shutdown cooler temperatures as predicted by RELAP at normal reactor operating conditions, and a guard containment filled with nitrogen at a pressure of one atmosphere. The depressurization accident starts at the normal operating condition of the reactor plant at 100% power. This 100% steady state is therefore at the beginning of the transient whereas the long-term steady state of section 3.6.6 is at the end of the transient when a long term quasi equilibrium has been reached. These temperatures are 744 °K (471 °C) for the upper section of the reactor vessel, 752 °K (479 °C) for the lower section of the reactor vessel and 753 °K (480 °C) for the shutdown cooler (SCS). It should be noted that the steady state analysis reported earlier was based on steady state temperatures of the

boundary surfaces, guard containment pressure (6 bar) and a helium concentration (mol fraction of 25 %) at the end of the transient.

Figure 21 shows the predicted temperature distribution for the guard containment walls. This distribution peaks to a value of 567 °K (294 °C) opposite to the shutdown cooler. This temperature is greatly above the concrete limiting temperature below (373 °K) 100 °C and it is due to radiation from the hot outer walls of the shutdown cooler. At normal reactor operating conditions these walls have a much higher temperature than at the end of the depressurization transient. Insulation of the outer surface of the shutdown cooler would cut the heat transfer from the SCS to the guard containment.

Another steady state analysis was performed with the shutdown cooler insulated (adiabatic boundary condition). As Figure 22 shows, the temperature of the wall of the guard containment opposite to the cooler is drastically reduced to well below 100 °C (373 °K). However, the temperature of the guard containment above the reactor vessel remains at 131 °C, well above the concrete limiting temperature. Because this temperature is not greatly higher than the limiting temperature, it was decided to use this steady state analysis as the initial state of the depressurization transient. This transient analysis is in progress.

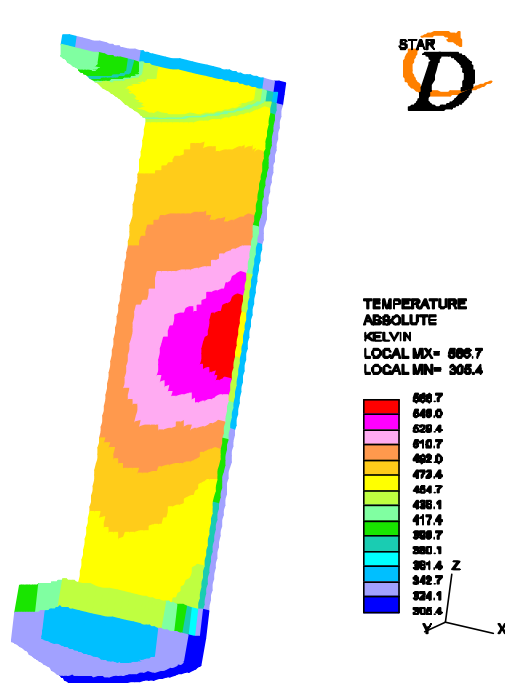


Fig. 21. Guard Containment Temperature Distribution at Initial Steady State Conditions

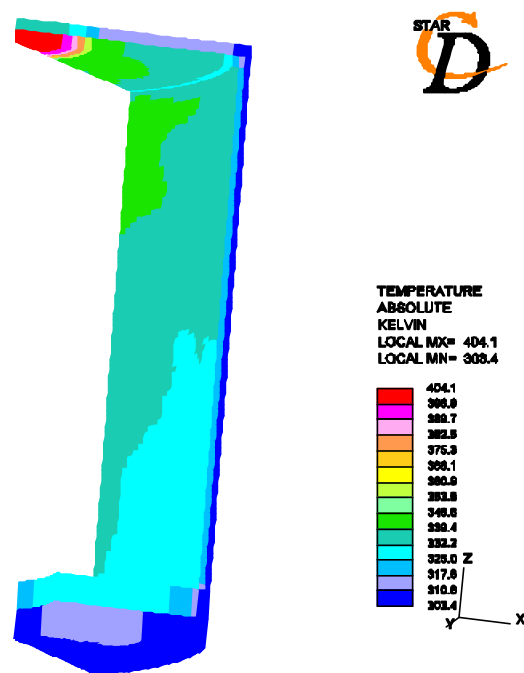


Fig. 22. Guard Containment Temperature Distribution Conditions (Insulated Shutdown Cooler.)

## References

1. J. Rouault and T. Y. C. Wei, "Selection of the Concept for Point Design", I-NERI Project #2001-002-F, Report GFR 021, May 2004.
2. I-NERI Project Staff, "System Design Report", I-NERI Project #2001-002-F, Report GFR 023, February 2005.

### **3.5 System Integration**

The Generation IV GFR R&D program is managed in the U.S. by the GFR System Integration Manager (SIM). The activities for the GFR SIM during FY05 include:

- Revision of the international R&D plan. One revision was issued, and answers to the comments/questions given by the GIF Expert were completed.
- Attendance at Steering Committee meetings, held in Germany (January 2005), and France (September 2005).
- Integration of Generation IV GFR activities with Advanced Fuel Cycle Initiative (AFCI) work, including attendance at the semi-annual meetings, and the periodic meetings of the Fuel Development Working Group.
- Coordination of other GFR related R&D currently funded by other sources.
- Promotion of the GFR at technical meetings, conferences, seminars, and special workshops.
- Reporting to DOE-NE on the technical progress and budget for GFR activities, and development/maintenance of the GFR R&D plan.

## 4. GFR Materials for Moderate to High Temperature Use

### 4.1 ODS Joining Studies

#### 4.1.1 Torsional Resistance Pressure Welding

As indicated in previous reports, an axial motion was initially used in resistance pressure welding for convenience because that was the loading mode of the existing Gleeble configuration. One limitation of the axial welds was the limited travel (a few mm), which limits the fresh material that can be brought into contact during the welding process. It also necessitates some diametrical change in the cladding to assure intimate contact, though this could probably be minimized with proper design and fixturing.

In January 2005, a torsional Gleeble load unit was purchased, which permits hydraulically controlled motion in both axial and torsional directions, and this opened an opportunity for another kind of resistance pressure weld. Fixtures were made which adapted this unit, which is designed for multiple-turn, high-strain and high strain rate torsion testing, as shown in Figure 1. This type of welding addresses the shortcomings of axial welding. Because the workpieces can be rotated many times with respect to one another more complete surface oxide removal is possible and the welding can be accomplished at lower axial loads, hence requiring less massive machinery.

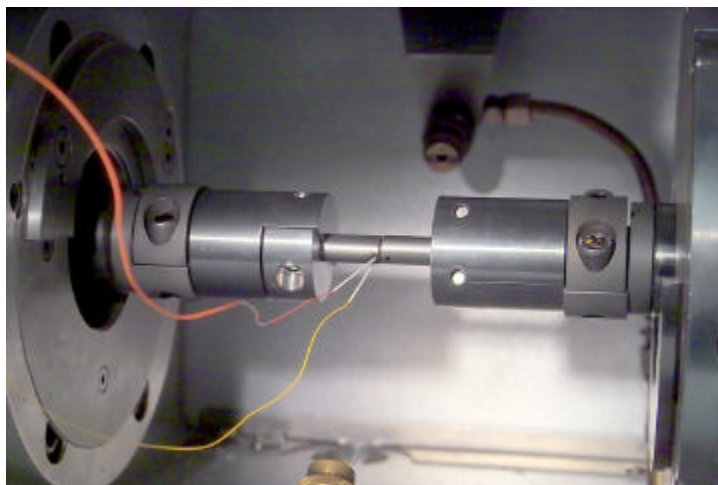


Figure 1. Simulated fuel cladding (left) and end cap (right) prior to welding.

There were some unanticipated alignment problems with the fixtures: as can be seen in Figure 1, the parts do not quite align. There was also excessive runout in the rotating side (right side in the figure), sometimes amounting to approximately the wall thickness of the parts (10 mm diameter, 1.0 mm wall, approximating a nominal cladding dimension). The fixtures holding the parts were not designed to compensate for this, and in a complete rotation it was found that the combination of axial force and runout led to gross deformation of the weld zone. This was remedied in later welds by reducing the axial force and using a torsion program that moved 60° several times rather than a full turn in one direction. An example of the better, later specimens is shown in Figure 2, where misalignment is nonetheless apparent. A cross section of a weld similar to that shown in Figure 2 is shown in Figure 3, and at higher magnification in Figure 4.



Figure 2. Typical torsional mode weld, illustrating results of fixture misalignment. Axial load 300 N (~67 lbf), torsional motion +30°, -60°, +30° over 2 s, temperature 850°C.

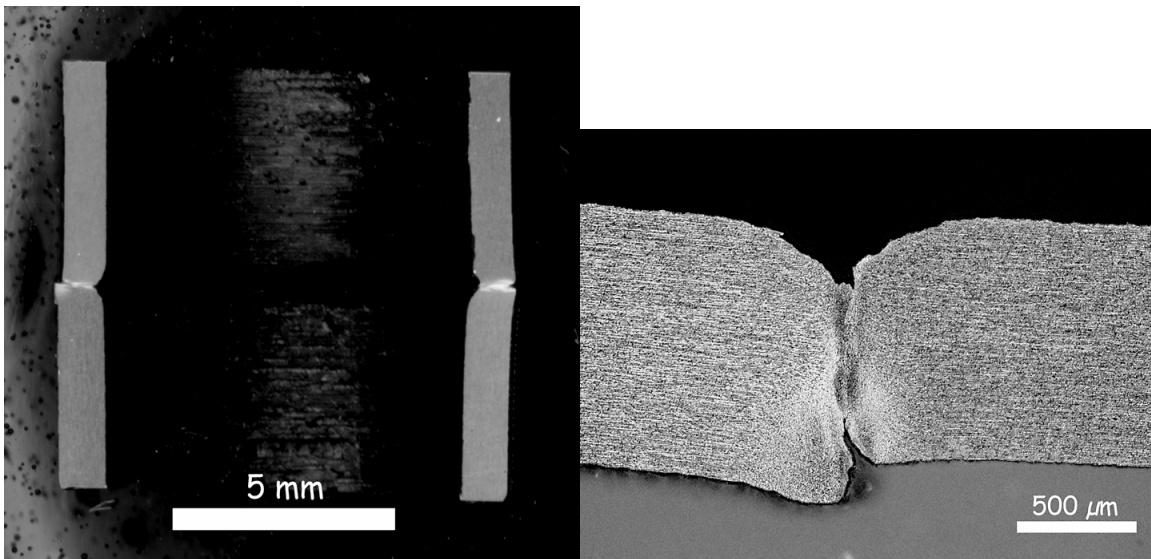


Figure 3. Cross section of torsional mode weld, axial load 100 N (~22 lbf), torsional motion +30°, -60°, +60°, -60°, +30° over 4 s, temperature 850°C.

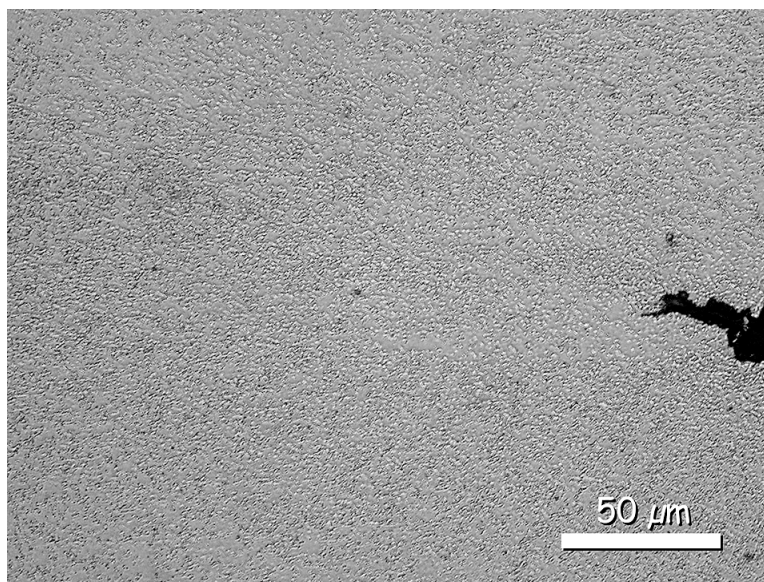


Figure 4. Weld area at higher magnification, showing complete bonding and fine grain size.

#### **4.1.1.1 Resistance Pressure Welding Conclusions**

Based on the present work, the torsional joint seems the most promising, although the axial joint could probably be made to work. A fully optimized joint was not attempted in these trials for several reasons. In the case of the torsional joint, the misalignment and runout of the rotary fixtures and an unintentional chamfer on the simulated tube ends.

The metallurgical processes seem sound, however, and should be easily achievable in a system custom-designed for the production welding of fuel rod end caps. Such a system, which requires relatively low loads and heating capacities, would be much smaller than the multi-purpose Gleeble and be relatively inexpensive. Design features of such a system would include:

- Precision fixtures, tooling, and workpiece specifications yielding close axial and joint face alignment;
- Well controlled actuators, probably electrical rather than hydraulic based on the low loads required;
- A power supply for resistance heating of the joining surface, probably transformer/SCR based;
- PC-based control and data acquisition.

Since the critical welding time for these designs is several seconds long, it should be possible to develop correlations between the various resulting forces and displacements to assure weld quality in these difficult-to-inspect welds. Further work needs to be done in the metallurgical characterization of the joints, including the capacity to grow the desirable large grains across the interface if ODS materials are chosen for reactor applications. The basic process, however, should be adaptable to the joining of any metals.

#### **4.1.2 Transient Liquid Phase Bonding of Ferritic ODS Alloys**

##### **4.1.2.1 Substrate and Interlayer Materials**

Transient liquid phase (TLP) bonding and solid-state diffusion bonding experiments were continued and this work has transitioned from MA956 to PM2000. Pure boron interlayers (1  $\mu\text{m}$  in thickness) were prepared using electron beam physical vapor deposition (EBPVD). Substrates were joined with the faying surface cut along (longitudinal-longitudinal, L-L) and perpendicular (transverse-transverse, T-T) to the working direction. [1]

##### **4.1.2.2 Bonding Trials and Post-Bond Heat-Treatment**

###### ***4.1.2.2.1 Transient Liquid Phase Bonding***

Bonding was conducted in the Gleeble 1500 thermomechanical processing system at 1250 °C for up to 6 minutes, followed by recrystallization post bond heat treatment (PBHT) at 1385 °C for 2 hours, to induce grain growth in the bulk substrate and across the bondline. Boron interlayers resulted in well wetted bonds in both L-L and T-T orientations, as shown in figures 1 (a) and (b). PBHT resulted in the recrystallization of the substrates. However, a large amount of porosity has also been observed in the substrates (figures 1 (c) and (d)). Porosity has also been observed in the unbonded bulk material. A microstructural survey of the bar was conducted and a significant variation in the porosity and composition of the recrystallized material along the length of the bar

was observed and has been described in detail in an interim report [2]. Porosity in the material was confirmed by conducting metallography on some of the same samples at INL. This has been attributed to the release of trapped shielding gases used during mechanical alloying [3,4]. A thick layer of fine grains extending up to 100 – 200  $\mu\text{m}$  were observed at the bondline when substrates were joined using a 1  $\mu\text{m}$  boron interlayer followed by recrystallization heat treatment (figure 1 (e)). This formation of recrystallized fine grains at the bondline might be due to boron induced secondary recrystallization [5]. Unwanted fine grain formation was also occasionally observed in the core and at the edges of the unbonded bulk material (figure 1 (f)).

#### ***4.1.2.2.2 Solid-state Diffusion Bonding***

To study the effect of substrate orientation on bond microstructural development, diffusion bonding of PM2000 was performed in the fine grain condition both in the transverse to transverse (T-T) orientation and longitudinal to longitudinal (L-L) orientation. Bonding occurred in both these orientations, at low pressures 1 – 5 MPa, and for bonding times of up to 6 – 8 minutes (figures 2 (a) and (b)), although occasional unbonded regions have been observed at the bond interface in the transverse orientation. Such rapid bonding, at very low applied stresses, might perhaps be attributed to a significant contribution from grain boundary diffusion in the fine grain condition [6,7]. Recrystallization PBHT resulted in porosity in the diffusion bonds similar to the recrystallized heat treated TLP bonds (figures 2 (c) and (d)). Hence, the porosity developed during heat treatment in the as-received bulk PM2000 appears to be limiting the integrity of the bonds. It is important to reduce the porosity in the bulk material in order to achieve both higher bulk and bond strengths.

#### ***4.1.2.2.3 Room Temperature Mechanical Testing***

Shear testing has been conducted on PM2000 diffusion bonds fabricated using unrecrystallized, fine-grained substrates in both longitudinal-longitudinal and transverse-transverse orientations.



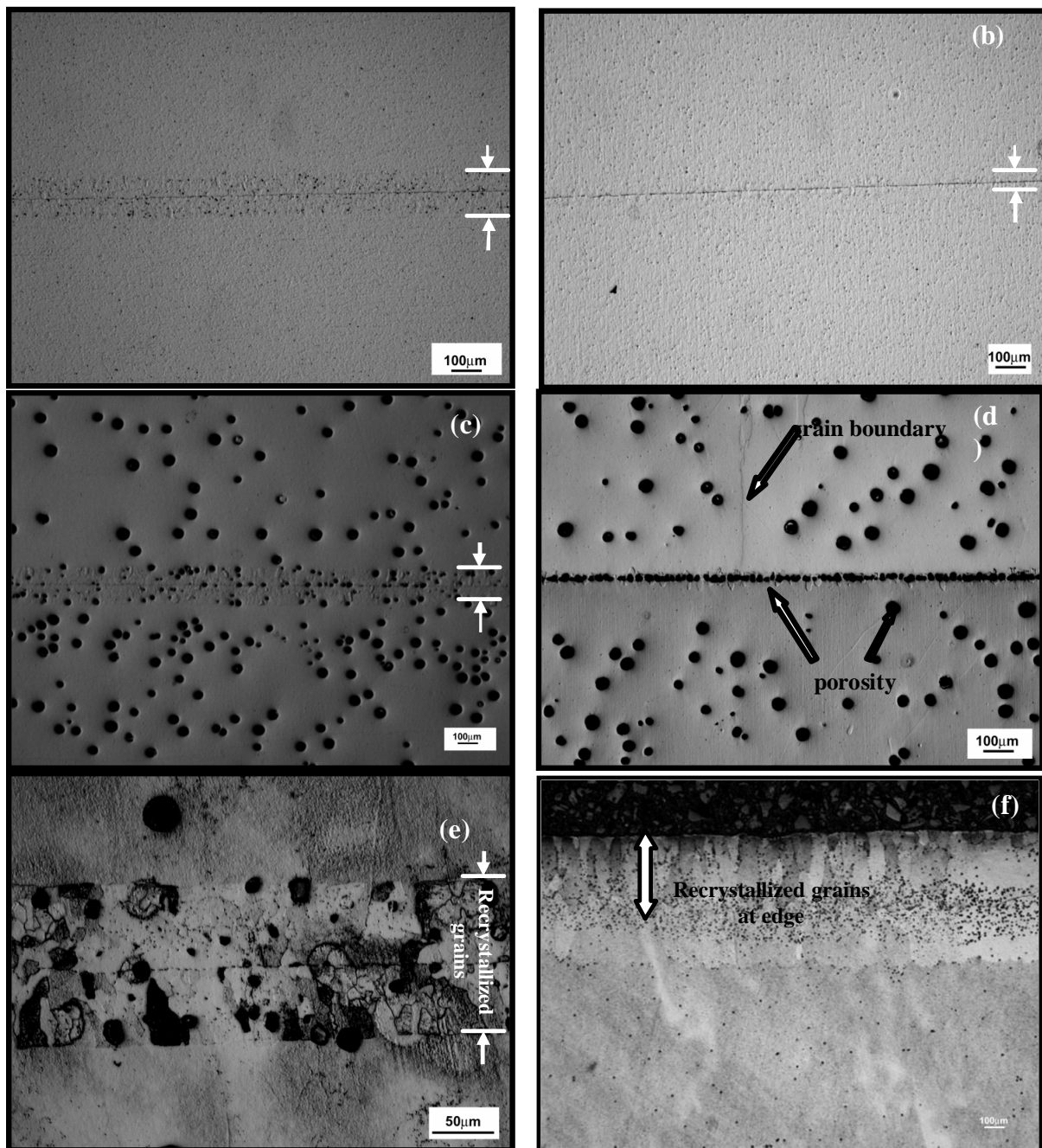


**Figure 1.** PM2000 fine grain –fine grain bonds using 1 μm B interlayer (a) unetched, 310 s, 1250 °C, L-L orientation (b) 300 s, 1250 °C, T-T orientation (c) and (d) same bonds as in (a) and (b), respectively, after 2 h, 1385 °C. Notice the porosity developed in the bonds during PBHT. (e) etched same as in (c). The region within the two white arrows represents a secondary recrystallized region. (f) anomalous grains at the edge.

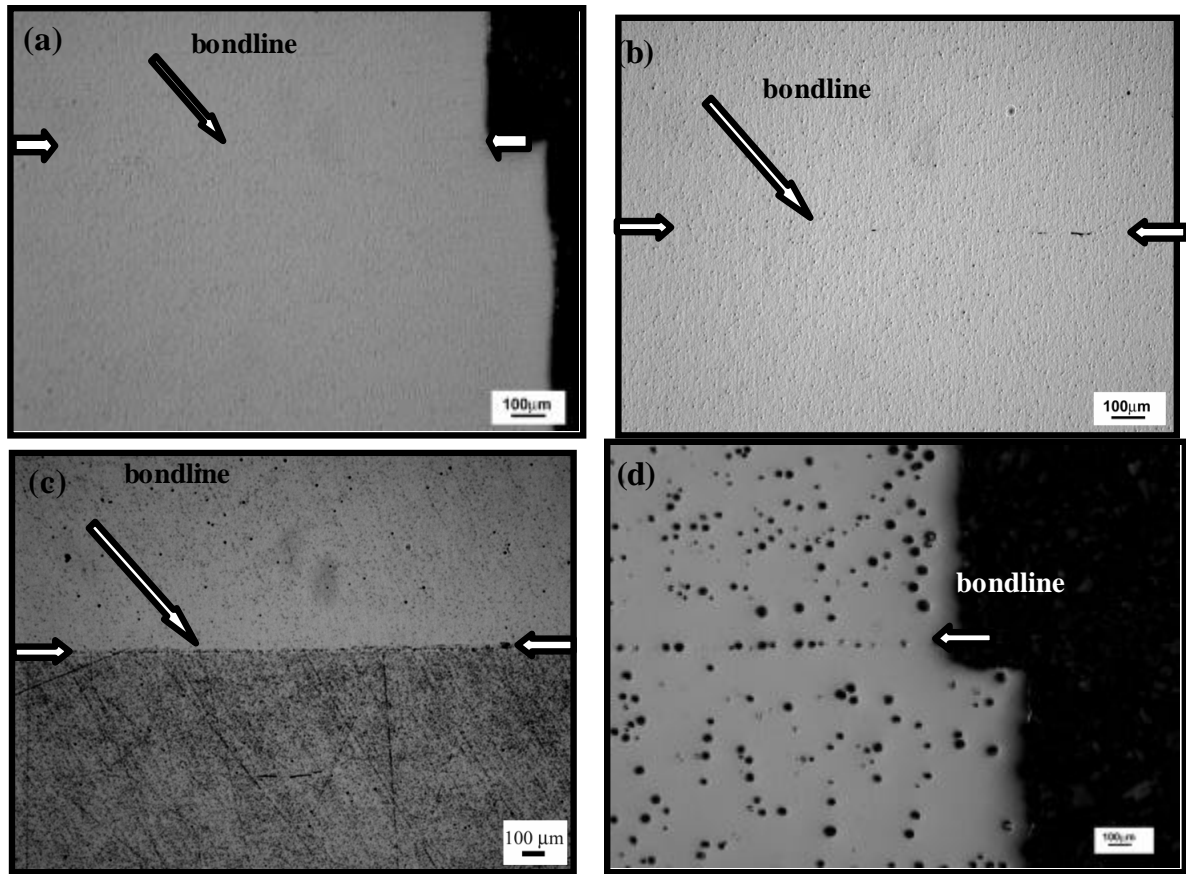


**Figure 2. PM2000 fine grain diffusion bonds (a) unetched 310 s, 1250 °C L-L orientation, (b) unetched 300 s, 1250 °C T-T orientation. Bonding occurred in both the orientations, however, occasional porosity can be observed in (b). (c) 380s, 1250 °C + PBHT 2 h, 1385 °C L-L orientation and (d) same bond as in (a) after 2 h, 1385 °C. Notice the porosity developed in the bonds during PBHT.**

Bonding was followed by PBHT for 2 hours at 1385°C. For comparison, shear tests were conducted on bulk material in both the fine-grained condition and after recrystallization annealing. The peak shear stress values of the tests in both orientations are shown in figure 3. The peak shear stress of the recrystallized bulk material is lower than the as-received, unrecrystallized bulk material, a result expected due to the high grain boundary density in the fine-grained material. The transverse orientation showed higher peak shear stress as compared with the longitudinal orientation in the bulk material. Average peak shear strengths of the PBHT bonds in the T-T and L-L orientations were on the order of 70% and 80% of that of the bulk recrystallized material, respectively.

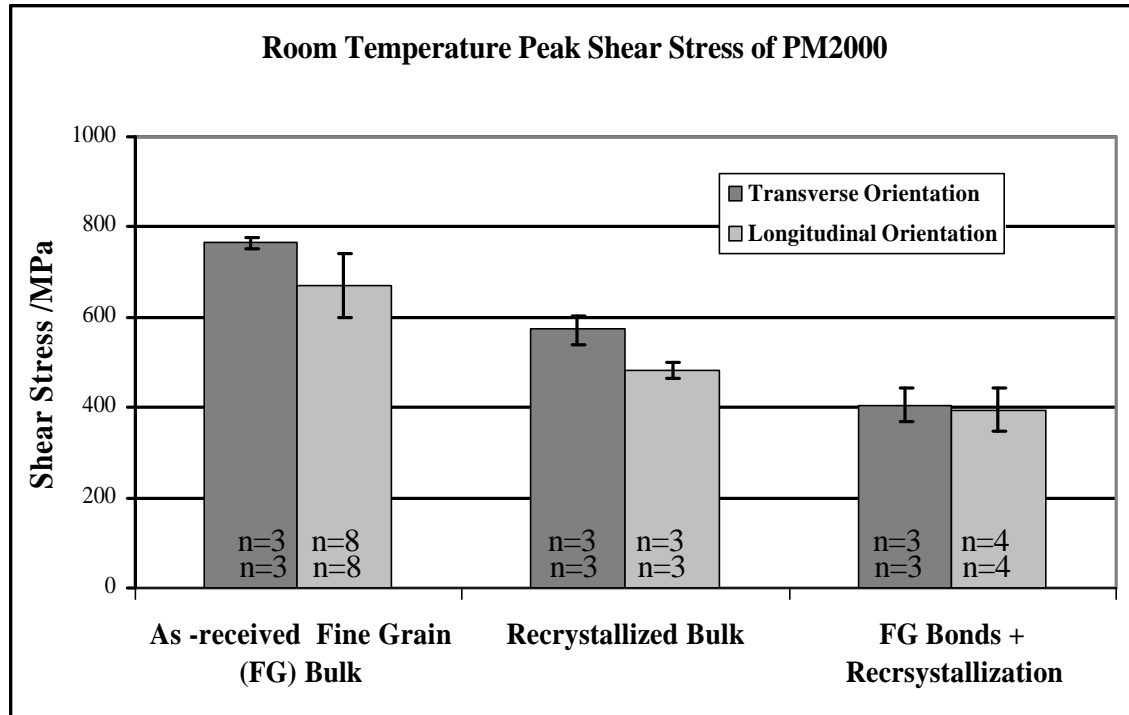


**Figure 3. Room temperature shear tests of PM2000 in the as-received fine grain condition, recrystallized condition and bonded + recrystallized condition in both transverse and longitudinal orientations. Note the error bars represent standard deviation of the test results and n represents the number of tests conducted.**

Fractography was conducted using the JEOL-840 scanning electron microscope (SEM). Fracture surfaces of the bonds and the bulk exhibited planar shear and secondary cracking. In general, bonds which failed at the bondline showed planar shear (figure 4 (a-b)), and those which failed in the bulk showed mixed planar shear and secondary cracking, (figure 4 (c-d)). The former failed at a lower peak stress (71% of the peak shear stress of recrystallized bulk PM2000) as compared with the latter (78% of the peak shear stress of recrystallized bulk PM2000).

Tensile testing was conducted on diffusion bonds prepared using fine grain PM2000 in the L-L orientation. For comparison, tests were also done on samples of the bulk material. The bonds were tested both in the as-bonded condition and after PBHT for two different times: (a) 5 s and (b) 300 s at the bonding temperature (1250 °C). In the unrecrystallized (fine grain) condition, the 5 s bond, 300 s bond and bulk material showed average strengths of 800 MPa, 833 MPa and 1 GPa, respectively (figure 5). In the unrecrystallized condition, a maximum bond strength of about 83% compared with that of the bulk material was obtained in the 300 s bond. In the recrystallized (coarse grain) condition, the 5 s bond, 300 s bond and bulk material showed average strengths of 577 MPa, 499 MPa and 522 MPa, respectively. In the recrystallized condition, a maximum bond strength of about 110% compared with that of the bulk material was obtained in the 5 s bond. An increase in the tensile strength was also observed with increasing bonding time.

The strength of the as-bonded samples increased from 800 MPa to 833 MPa as the bonding time increased from 5 s to 300 s, which may be related to the increasing bond area with increasing

bonding time. However, a decrease in the bond strength was observed in the recrystallized condition, from 577 MPa to 499 MPa, as the bonding time increased from 5 s to 300 s. This decrease in the bond strength may be due to the variation in the porosity developed during the PBHT in the bonds. Some variation in the material's response to heat treatment has already been noted earlier in this study, (figures 2 (c) and (d)). The unrecrystallized bonds showed a flat fracture surface, and failure occurred at the bondline. PBHT bonds showed some elongation and failed near the bond region at a lower stress than the as-bonded samples, showing a 45 ° inclination to the gage length. This might be due to the deformation of the large recrystallized grains near the bondline. The fracture surfaces revealed a large number of voids under light microscopy, mainly due to the porosity developed in the material during PBHT. The increase in grain size also resulted in a decrease in the peak stress.

#### ***4.1.2.2.4 Porosity Reduction***

Porosity has been observed both in the unbonded and bonded PM2000, which degrades the mechanical properties of the material. This porosity has been attributed to the release of entrapped shielding gases, such as, hydrogen or argon, which were used during mechanical alloying. A dual-stage heat treatment employed by Chen et al. [8] was useful in reducing porosity in the material; however, it has not been successful in eliminating porosity completely. Work is in progress in order to reduce porosity in this material. A low temperature anneal of either 30 minutes at 1250 °C or 12 hours at 700 °C, followed by 2 hours at 1385 °C is being investigated at Auburn.

#### **4.1.2.3 Plans for the Next Phase of the Project**

TLP and diffusion bonds shall be conducted after the dual-stage heat treatment experiments to reduce porosity have been completed. The room temperature mechanical testing of the bonds will be continued. A limited number of bonds will be creep tested at 1000 °C and the crept samples will be studied using optical microscopy and scanning electron microscopy.

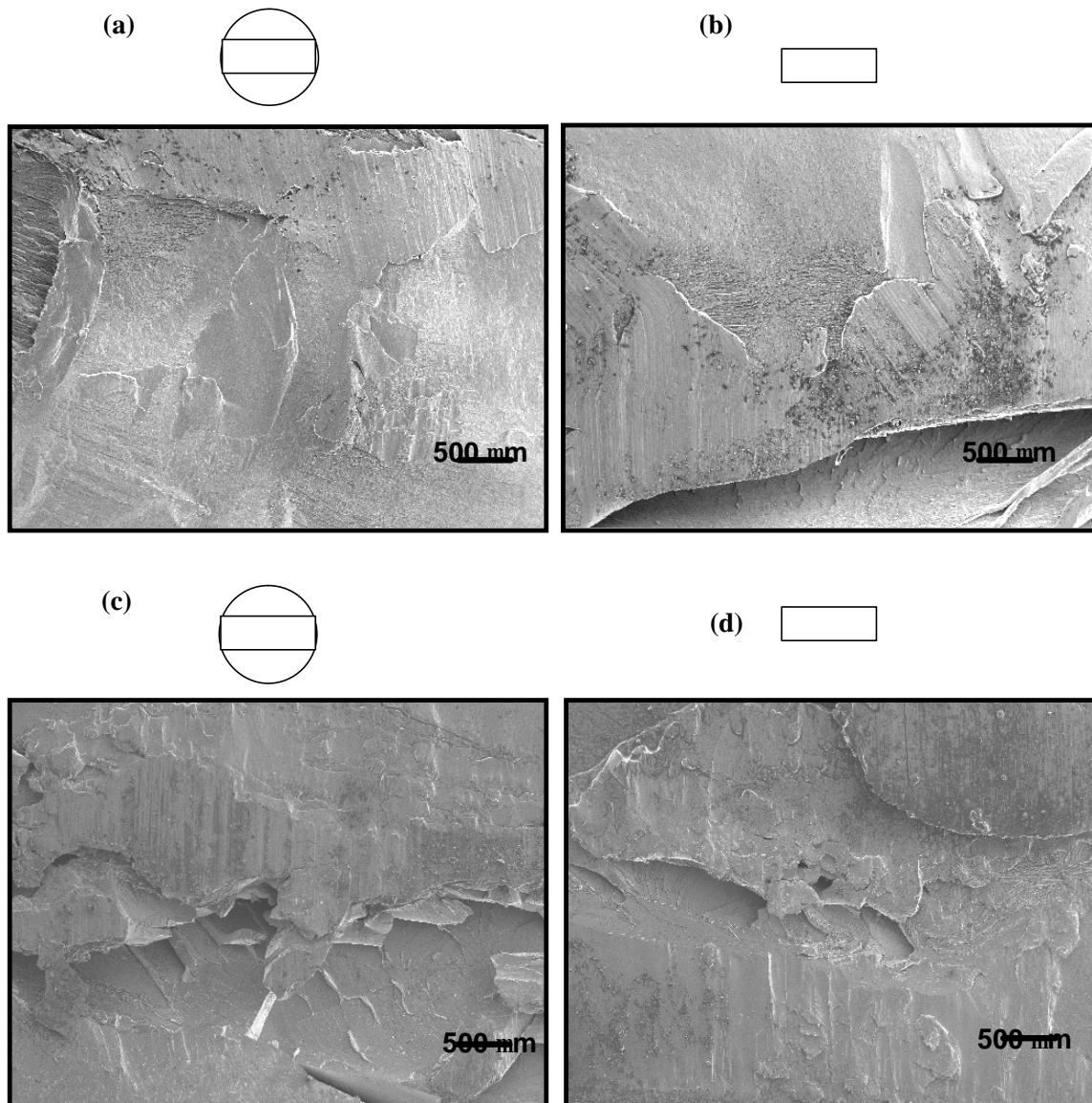


**Figure 4 Shear test fracture surfaces of PM2000 transverse-transverse bonds. Schematics of the fracture specimens from which the fractographs were extracted are shown above each figure: (a) and (b) 300 s, 1250 °C + PBHT 2 h, 1385 °C, mostly planar shear cracking, and (c) and (d) 309 s, 1250 °C + PBHT 2 h, 1385 °C, secondary + planar shear (mixed) cracking.**

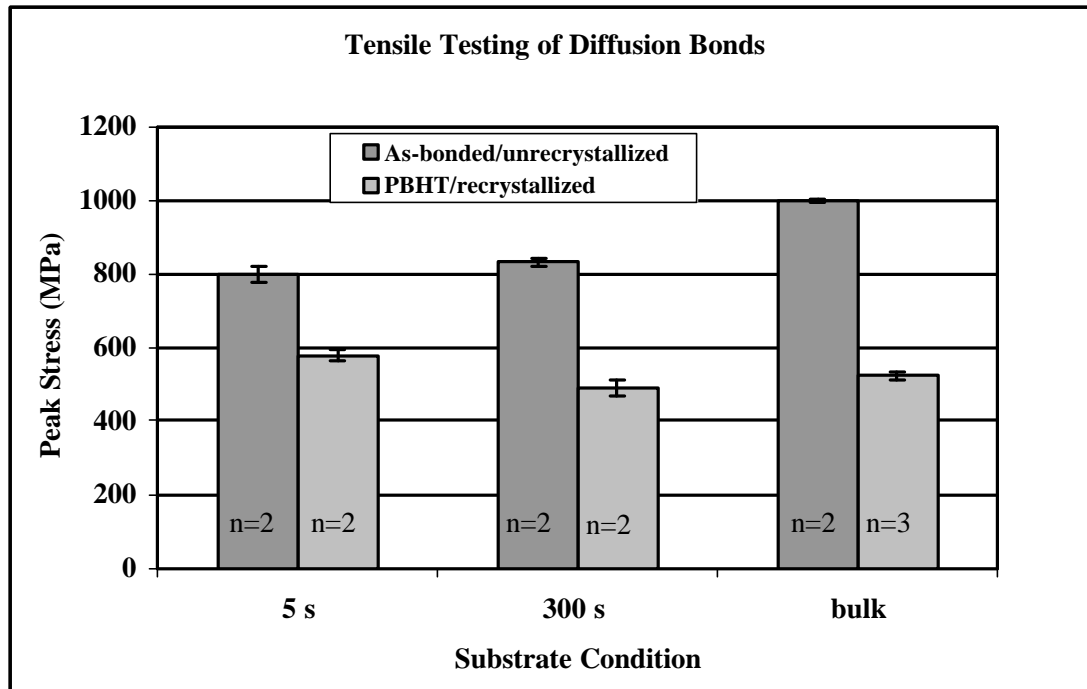


**Figure 5** Room temperature tensile tests of PM2000 material 5 s bond, 300 s bond and bulk in the as-received fine grain (■) and recrystallized (□) conditions. Note the error bars represent standard deviation of the test results and n represents the number of samples tested.

#### References

1. V. G. Krishnardula, D. E. Clark and T. C. Totemeier, "Joining Techniques for Ferritic ODS Alloys", INL Report, June 2005, under Contract DE-AC07-05ID14517.
2. V.G. Krishnardula, Interim report to INL, "Survey of PM2000 1 inch and 2 inch Bar Material", March 2005.
3. M. Turker, J. Mater. Sci. 40 (2005) 1201.
4. Y.L. Chen, A.R. Jones, and U. Miller, Metall. Mater. Trans. A 33A (2002) 2713.
5. A. J. Markham, Ph.D. Thesis, University of Cambridge: Cambridge, UK (1988).
6. A. Hill, E.R. Wallach, Acta Metall. 37 (1989) 2425.
7. N. Orhan, M. Aksoyand, M. Eroglu, Mater. Sci. Eng. A271 (1999) 458.
8. Y.L. Chen, A.R. Jones, Metall. Mater. Trans. A 32A (2001) 2077.

## 4.2 Ion Irradiation Study on Microstructure Stability of GFR Ceramics: ZrC, ZrN, TiC, TiN and SiC

Refractory ceramics have been considered for the gas cooled fast reactor (GFR). The fuel for the GFR requires both a high heavy metal loading and the ability to withstand temperatures of approximately 1200°C under normal operation and up to 1600°C during a loss of coolant accident. Current gas reactor fuel technology is not adaptable to a gas-cooled fast reactor. The categories of fuel with the highest potential for success are carbide and nitride-based composite-type fuels. These fuels consist of a fissile phase dispersed within a refractory matrix. Potential fuel matrix materials are limited to those with low neutron absorption (thus excluding refractory metals), high melting temperatures (> 2000°C), and tolerance to high dose irradiation damage

from neutrons. Refractory ceramics of ZrC, ZrN, TiC, TiN and SiC are candidates for matrix materials for dispersion type fuel due to their neutronic performance, thermal properties, chemical behavior, crystal structure, and physical properties. The transition metal carbides and nitrides (ZrC, ZrN, TiC and TiN) have a NaCl type FCC structure. The 6H-SiC is a common form of SiC that has a hexagonal structure. The high dose radiation effects on the microstructure of these ceramics have not been explored previously.

A comprehensive review of radiation effects in ceramics can be found in the reference [1]. A limited number of ZrC TRISO-type fuel particles have been irradiated with neutrons at 900°C to a low burnup (~1.6 dpa) [2]. Optical examination of the cross section of the irradiated fuel particles did not reveal any mechanical failure of ZrC coating (~70  $\mu\text{m}$  thick) although no detailed postirradiation microstructural analysis of the ZrC was performed. Data for ZrC has been generated under a limited range of irradiation conditions [3,4]. These studies showed a ZrC lattice parameter increase at neutron fluences of  $\sim 1.5 \times 10^{20} \text{ n/cm}^2$  (~0.2 dpa) at 50, 150 and 1100°C with lattice increases of 0.26%, 0.46% and 0.13%, respectively. The work by Keilholtz et al [5] on ZrC irradiated with neutrons at 300-700°C suggests the mechanism of lattice expansion is defect agglomeration. They reported a measured volume increase of approximately 3% at doses of ~ 3 dpa and remained saturated up to a dose of 8 dpa. Their calculated volume increase from ~0.5% lattice expansion was about 50% of the measured volume increase at doses of 3~8 dpa. There is no microstructural characterization for neutron irradiated ZrC reported in the open literature.

The work by Dyslin, et al. on ZrC and TiC irradiated in the Engineering Test Reactor (ETR) at temperature of 130-355°C to a dose of ~7.5 dpa showed a volume increase of 2.5% and 2.0% for ZrC and TiC, respectively [6]. Their thermal annealing studies of the irradiated ceramics indicated a greater shrinkage effect on TiC than on ZrC, suggesting a larger fraction of single defects in TiC. The smaller volume change in TiC was attributed to the smaller fraction of defect clusters compared to ZrC. The single defects are believed to cause less volume increase than clusters and are relatively easier to be annealed out.

SiC is one of the special materials that has attracted a lot interest due to its electronic properties, thermal stability, extreme hardness and chemical inertness. The work by Weber, et al., [7] on single crystal 6H-SiC irradiated in-situ along the [0001] orientation with 1.5 MeV Xe ions at low temperatures (20k~475k) revealed that the material becomes completely amorphous at a dose of 0.25 dpa at T=20k. They found the critical temperature above which amorphization does not occur is 485k. Persson et al., reported their work on 4H-SiC implanted with 180 KeV Al ions at 600°C to doses of  $1.3 \sim 7.8 \times 10^{14} \text{ cm}^{-2}$ . They found loops at doses above  $2.6 \times 10^{14} \text{ ions/cm}^2$  and the loops reside on (0001) basal plan with average size of approximately 50 nm [8]. They also reported that the loops in 4H-SiC consist of C or Si self-interstitials, or both [9].

This work investigated the microstructural response of ZrC, ZrN, TiC, TiN and SiC irradiated with 1.0 MeV Kr ions to doses of 10 and 70 dpa at 800°C with a damage rate of approximately  $3.0 \times 10^{-3} \text{ dpa/s}$ . Considering the need to increase the temperature for the high dose rate to produce effective damage, the temperature used for heavy ion irradiation may not be representative of the same temperature in neutron irradiation. The large ratio of surface to volume has always been a concern for irradiation of thin foil using TEM disc samples.

Nevertheless, heavy ion irradiation in an electron microscope using TEM samples offers the opportunity to perform low-cost irradiation studies on a wide range of materials that simulate some important aspects of the fission neutron environment. The result for a specific material from heavy ion irradiation of a TEM sample is not expected to be the same for neutron irradiation. However, a comparison of the microstructural response for materials under the same irradiation conditions using this technique should provide valuable information on relative performance of the materials.

#### 4.2.1 Experiments

Commercially produced ZrC, ZrN, TiC, TiN and  $\alpha$ -SiC samples, by vacuum hot pressing of powders then machining to form rods, were used in this work. The ceramics were received as 20 mm long rods with a diameter of 3 mm. Their chemical composition is listed in Table 1. The densities of ceramic rods were measured using both dimension and immersion methods. Porosity in the microstructure was examined using scanning electron microscopy (SEM). The 3 mm diameter discs with a thickness of 200  $\mu$ m were cut using a low speed diamond saw. These disc samples were then wet-polished down to a thickness of  $\sim$ 100  $\mu$ m. The discs were then mechanically dimpled from both sides to a thickness approximately 10~20  $\mu$ m in the middle, followed by precision ion milling with 5.0 KeV argon ions at an incident angle of 5~7 degree.

Table 1. Chemical composition of the refractory ceramics (wt%)

	Zr	Ti	Si	Hf	Zn	W	C	N	O	Others	Ratio*
ZrC	<b>84.8</b>	0.19	<0.001	1.91	<0.02	<0.1	<b>11.3</b>	0.61	0.21	<0.1	1.01
ZrN	<b>87.6</b>	0.095	0.007	<0.02	<0.02	0.19	0.76	<b>11.4</b>	1.43	<0.1	0.85
TiC	<0.02	<b>80.2</b>	0.007	<0.02	0.17	<0.05	<b>19.4</b>	0.057	0.51	<0.02	0.97
TiN	<0.02	<b>78.9</b>	0.001	<0.02	<0.02	<0.05	0.58	<b>22.0</b>	0.46	<0.02	0.95
SiC	<0.005	<0.1	<b>62.08</b>	<0.005	<0.001	<0.05	<b>29.6</b>	0.35	0.58	Al_1.44 Fe_0.65	1.11

\* The atomic ratio of the major element C or N to Zr, Ti or Si.

The irradiation was conducted with 1.0 MeV Kr ions using an intermediate voltage electron microscope (IVEM) equipped with a Tandem accelerator at Argonne National Laboratory. TEM disc samples were irradiated at 800°C to 10 and 70 dpa except for TiN that was only irradiated to 70 dpa. Beam diameter for Kr ions was approximately 2 mm. Irradiation dose was calculated using TRIM program [10]. Dose rate is approximately  $3.0 \times 10^{-3}$  dpa/s with a pressure of less than  $7 \times 10^{-8}$  torr. During the irradiation, the electron microscope was operated at 300 kV. The microstructural evolution was monitored on a TV screen and recorded on videotape.

Post-irradiation microstructure characterization was conducted at INL using a JEOL2010 transmission electron microscope operated at 200 kV. The features of irradiated microstructure such as loops, dislocation network, cavities and precipitates were examined. Diffraction patterns at zone [011] or [001] were used to determine the changes in lattice constant for material with FCC structure. Two beam diffraction at  $g=(200)$  is used for bright field imaging of dislocations and loops while rel-rod dark filed imaging is used to examine if faulted loops were present. For the hexagonal 6H-SiC, the diffraction patterns at zone [1,-2,1,0] and [0,2,-2,-1] are used to determine the possible lattice expansion while the diffraction of (0,0,6) or (2,-1,6) near zone [0,-1,1,0] are used for the loops. The high resolution images for 6H-SiC basal plane projection are



obtained at zone [1,-2,1,0] either without objective aperture or using the largest objective aperture.

## 4.2.2 Results

Results of density measurement are listed in Table 2 along with the theoretic density of these ceramics for comparison [11,12]. The Hf (~2 wt.%) in ZrC and the porosity in TiN, Figure1, is responsible for the unexpected high relative-density for ZrC and low relative-density for TiN, respectively. General features of the unirradiated microstructure for all 4 refractory ceramics are the uniformly distributed small defect clusters caused by ion milling damage during sample preparation. Bubbles at a size of approximately ~ 1 nm were found in the unirradiated samples. Although the number density of bubble decreased and a slight size increase was observed, voids were not found in the irradiated ZrC, ZrN and TiN. A general observation for radiation-induced microstructural changes was an increase in the lattice constant and the lack of faulted loops at 70 dpa. The following sections provide the microstructure analysis for these ceramics before and after irradiation with Kr ions at 800°C.

Table 2. Results of density measurement for as-received ceramics (g/cm<sup>3</sup>)

Ceramics	By dimension	By immersion	Theoretic	Imm./Theoretic (%)
ZrC	6.59	6.58	6.48	101.5
ZrN	7.06	7.06	7.30	96.7
TiC	4.84	4.84	4.90	98.8
TiN	4.43	4.92	5.39	91.3
SiC	3.18	3.19	3.22	99.1

### 4.2.2.1 ZrC

The microstructure of the unirradiated ZrC is dominated by a large number of small black dots due to ion milling with 5 KeV Ar ions, Figure 2. Rel-rod dark field images did not reveal any faulted loops in the unirradiated ZrC. Bubbles approximately ~1 nanometer in diameter were identified using overfocus (shown as black dots) and underfocus (shown as white dots) imaging technique. These small bubbles are believed to be due to damage caused by ion milling with argon ions. No precipitates were found in the unirradiated ZrC. The ZrC before irradiation has a FCC structure with a measured lattice constant of 0.471 nm, consistent with the data of 0.473 nm in literature [12]. The Kikuchi line patterns due to the inelastic scattering of electrons from atomic planes are clearly visible under convergent beam diffraction. A few scattered voids and line dislocations were found at low magnification. No ring pattern was identified under select aperture diffraction (SAD).

For the ZrC sample irradiated at 800°C to 10 dpa, a ring pattern developed in the diffraction pattern, Figure 3(a). The measurement from the diffraction spots from zone [011] revealed a 0.6% increase in lattice constant. No voids or faulted loops are identified in the 10-dpa sample. The irradiated microstructure of ZrC at a dose of 70 dpa is shown in Figure 3(b). The visibility of the ring pattern increases while the visibility of Kikuchi pattern drops to nearly zero. However, the diffraction spots are still well defined when a small select-area aperture is used (~250 nm). The weak beam dark field image using the diffraction from ring indicated the ring pattern formed due to clusters approximately 50 nm in size. EDS measurement of these clusters shows similar chemical composition to ZrC. No voids, faulted loops or amorphization were

identified. However, few cracks along the grain boundaries were identified. The measurement of lattice constant from the diffraction pattern at zone [011] indicated an approximately  $\sim 7\%$  increase compared to the unirradiated ZrC, Figure 4. The spot shape of the diffracted beam in the diffraction is severely deformed comparing to the unirradiated or low dose samples.

#### 4.2.2.2 ZrN

The microstructure of the unirradiated ZrN is shown in Figure 5 (left) with clear evidence of ion milling damage. There are a few areas with precipitates, scattered voids and dislocation lines, shown in Figure 5 (right). EDS revealed the circular shaped precipitates (typically  $< 200$  nm) are rich in Zr and O and believed to be  $\text{ZrO}_2$ . A few large polygon shaped precipitates (typically  $> 1$   $\mu\text{m}$ ) at grain boundaries are also observed. These precipitates are rich in Al and O with an atomic ratio near 2:3 and are likely  $\text{Al}_2\text{O}_3$ . The diffraction pattern and Kikuchi line pattern for the unirradiated ZrN is clear despite the defects caused by ion milling damage.

The microstructure of ZrN irradiated to 10 and 70 dpa at  $800^\circ\text{C}$  is shown in Figure 6. No dislocation loops (faulted or perfect) were identified. Moiré fringes were found in many areas of the sample, Figure 6 (a) and (b). EDS measurements indicate the areas with Moiré fringes are rich in Zr, N and O. Bubbles are clearly visible in the under or over focus imaging condition shown in Figure 6 (a). Diffraction pattern from the large  $\text{Al}_2\text{O}_3$  precipitates indicate the precipitates became fully amorphous at 70 dpa. No amorphization in ZrN was found. Similar to the 70 dpa ZrC sample, the visibility of Kikuchi pattern drops to zero. However, the select area diffraction at major zones still shows clear FCC diffraction spots with high index spots elongated at a large aperture size ( $\sim 1.25$   $\mu\text{m}$ ). Comparison of the diffraction pattern from major zone [011] and [001] is shown in Figure 7. The change in the lattice constant is clearly visible with an increase of approximately  $\sim 9\%$ . Different from ZrC, there are extra spots shown in both diffraction patterns at zone [011] and [001], suggesting an ordered FCC structure may be formed by irradiation.

#### 4.2.2.3 TiC

Similar to ZrC, the microstructure of the unirradiated TiC shows uniformly distributed small defect clusters, shown in Figure 8. The microstructure appeared relatively clean, no evidence of precipitates or line dislocations was observed in contrast to the unirradiated ZrC and ZrN. Diffraction spots and Kikuchi patterns are clearly visible showing a well defined FCC structure. There were a few areas showing scattered cavities. At a dose of 10 dpa, small dislocation loops and dislocation segments are observed, shown in Figure 9. For the TiC irradiated to 70 dpa at  $800^\circ\text{C}$ , the microstructure consists of dislocations, loops and voids, shown in Figure 10. Weak beam dark field images (Figure 10, center) give a better view of dislocation loops and dislocation network. These loops appear to be perfect loops with a Burgers vector of the  $(a_0/2)[011]$  type. No faulted loops were identified at 70 dpa. Voids were measured with an average size of 5.5 nm at a density of  $1.1 \times 10^{15} \text{ cm}^{-3}$ . The calculated void swelling at 70 dpa is approximately 0.01%.

No evidence of radiation induced precipitates or amorphization in TiC matrix are found. There are no noticeable changes in the Kikuchi patterns after irradiation up to 70 dpa. A comparison of diffraction spots from the major zone [001] and [011] between the unirradiated and the 70-dpa samples is shown in Figure 11, indicating only a minor change in the spacing of the diffraction

spots. The measurement on the diffraction spots indicates a lattice increase by approximately ~ 2% in the TiC irradiated to 70 dpa at 800°C.

#### 4.2.2.4 TiN

The unirradiated microstructure of TiN is shown in Figure 12. Both images were taken with  $\langle 200 \rangle$  diffraction, showing defect clusters with a few scattered line dislocations. No evidence of precipitates, amorphous phase, cavities and faulted loops was found. Kikuchi patterns were clear in the areas with right foil thickness.

There is no 10-dpa irradiation condition for TiN. The irradiated microstructure for 70 dpa TiN is dominated by dislocation lines and loops. The defect clusters shown in the unirradiated sample are almost completely wiped out. Figure 13 shows dislocations from the same area under different imaging condition, the  $\langle 200 \rangle$  diffraction at bright field (left), weak beam dark field at  $\langle 200 \rangle$  diffraction (middle), and  $\langle 0-22 \rangle$  diffraction (right). Similar to TiC, these loops are perfect loops with a Burgers vector of the  $(a_0/2)[011]$  type. The estimated loop size and density is 17 nm and  $3 \times 10^{15} \text{ cm}^{-3}$ , respectively. Evidence of radiation induced precipitates, voids, faulted loops, and amorphization are not found. Similar to TiC, the Kikuchi patterns in the irradiated sample are clear even at 70 dpa. The comparison of diffraction patterns before and after irradiation to 70 dpa is similar to TiC shown in Figure 11. The measured lattice increase for TiN at 70 dpa is approximately ~ 2%.

#### 4.2.2.5 SiC

For the hexagonal SiC there are many possible configurations due to the variation in its stacking sequence along  $[0001]$  crystal direction. The microstructural analysis for the unirradiated SiC indicates the SiC in this work is a 6H-SiC. Figure 14 provides the information on atomic configuration for 6H-SiC. The unirradiated microstructure for SiC is shown in Figure 15. Most of the areas on the sample show a uniform matrix with little evidence of ion milling damage from sample preparation in contrast to the unirradiated ZrC, ZrN, TiC and TiN. Dislocations and stacking faults are the main features can be found in the unirradiated SiC (See Figure 15, pictures on the top). Due to large lattice constant ( $c=1.5117 \text{ nm}$ ), the projection of basal planes at edge-on condition is clearly visible when imaged at zone  $[1,-2,1,0]$  without using the objective aperture, shown in Figure 15. A close look at stacking faults reveals the spacing variation between the fringes due to stacking faults on basal plane, Figure 16.

Although the JEOL2010 microscope with a  $\text{LaB}_6$  filament is not set for high resolution TEM to reveal the atomic configuration, it still can be used to provide fine details of the 6H-SiC on its atomic layers along  $[0001]$  direction. This is evidenced by the fine details present in Figure 17, where the fine line structure inside the major fringe corresponds to the 6 layers in 6H-SiC. If no stacking fault involved, there should be 6 fine lines between any two neighboring major fringes formed due to basal planes.

For the SiC irradiated to 10 dpa at 800°C, no evidence of radiation induced microstructural changes can be identified. Both diffraction and Kikuchi patterns look no different compared to the unirradiated SiC. Similar to the unirradiated case, stacking faults are still the main defect features present in the SiC matrix in the 10 dpa SiC, shown in Figure 18 (top). A close look at a

crack at grain boundary triple junction is shown in Figure 18 (bottom). The matrix does not show any visible evidence of the radiation damage.

At the dose of 70 dpa, the irradiated SiC shows well developed dislocation loops, shown in Figure 19. These loops are imaged with a two-beam condition at diffraction of  $g=[2,-1,6]$  near zone  $[0,-1,1,0]$ . The picture on the right is a closer look of the same area shown on the left. The average loop size and loop density are measured to be  $8.5 \pm 2.7$  nm and  $4.7 \times 10^{15} \text{ cm}^{-3}$ , respectively. The loop size distribution is shown in Figure 20 where the largest loops have sizes up to 22 nm. The comparison of the diffraction patterns from major zones are shown in Figure 21. No noticeable degradation and spacing changes can be identified. There are small bubbles identified in both 10 dpa and 70 dpa samples, with the latter one having a higher number density, shown in Figure 22. The quantitative characterization for the small bubbles is not attempted due to the small size ( $< 2$  nm) and high density.

### 4.2.3 Discussion

#### 4.2.3.1 ZrC

The sample irradiated at 800°C to 70 dpa resulted in a significant increase of 7% in lattice constant comparing to the unirradiated ZrC matrix. It is difficult to believe the 7% increase in lattice constant resulted from point defect agglomeration. One assumption is that there were two parallel processes occurring during irradiation. One was radiation induced defect accumulation leading to a small increase in lattice expansion and the other was radiation-induced precipitation resulting in a fcc ZrC with a lattice constant approximately 7% greater than the unirradiated ZrC matrix. The binary phase diagram shows ZrC at 800°C or below will precipitate out  $\alpha$ -Zr phase when C is below 38at% and precipitate out C when C is greater than 50at% [13]. It appears the original ZrC grain ( $> 5 \mu\text{m}$ ), after irradiation to 70 dpa, consisted many small ZrC clusters ( $< 50$  nm) with crystal orientation deviated slightly from each other, shown in Figure 3. That suggests the precipitation could be the major contribution to the 7% increase in lattice expansion. The visibility of Kikuchi may be used as a signature to qualitatively evaluate the damage on crystal structure. The lack of Kikuchi lines in convergent beam diffraction at the proper foil thickness indicates a severe distortion of atomic planes.

An increase of 7% in lattice constant could result in a significant increase in volume and internal stress thus setting the condition for cracking along grain boundaries in thin areas. This could be part of the reason for grain boundary cracking although thermal stresses in the thin TEM foil may also contribute to grain boundary cracking. Due to severe displacement damage at 70 dpa, the fraction of defects occupying the interstitial sites may be significant. Unfortunately the measurement of volumetric change due to Kr ion irradiation was not feasible. The large ratio of surface area to volume in TEM foil may allow a large lattice expansion than in the bulk material by irradiation to a high dose.

The bubbles in the ZrC caused by ion milling did not grow into micro voids. The lack of micro voids in the irradiated ZrC suggests the material is resistant to void swelling. The lack of faulted loops indicates that ZrC responded differently to radiation than fcc metals. Irradiation produces point defects and defect clusters in the material. The evolution of these defects and clusters under radiation-enhanced diffusion, plus the interactions of these defects with various sinks,

determines the irradiated microstructure. Unlike the fcc metals, the crystal structure of ZrC can be envisioned as an fcc lattice of Zr with C filling in the octahedral interstitial sites. According to the work by Li [14] on the inter atomic potential of ZrC, the properties of ZrC are dominated by the strong covalent bonds and the weak ionic bonds (Zr-C) and the original metallic bonds (Zr-Zr) can be neglected. The strong covalent bonding between Zr and C, plus the occupying of the octahedral interstitial sites in fcc Zr by C atoms, make the ZrC respond differently to irradiation than a typical fcc metals. It is possible that this unique structure and strong chemical bonding may significantly slow down the diffusion and increase the formation energy for both voids and faulted loops.

#### 4.2.3.2 ZrN

The irradiated microstructure for ZrN is quite different from ZrC, for example the presence of Moiré fringes, the ordered structure, and the lack of ring patterns in diffraction. Moiré fringes were found on many areas of the irradiated ZrN even at 10 dpa. It is well known that Moiré fringes are due to the overlap of two crystals. Since area with Moiré fringes measured rich in Zr, N and O, it is assumed ZrO<sub>2</sub> film was formed during irradiation. The oxygen to form ZrO<sub>2</sub> may come from large polygon shaped Al<sub>2</sub>O<sub>3</sub> precipitates found in the ZrN. Due to the wide spread of Moiré fringes, it is difficult to believe that the ZrO<sub>2</sub> precipitates pre-existed in the matrix produce the fringes. The amorphization of Al<sub>2</sub>O<sub>3</sub> by irradiation indicates ZrN is much more stable under irradiation than Al<sub>2</sub>O<sub>3</sub>.

The diffraction patterns from zone [001] and [011] of the 70-dpa ZrN revealed a structure typically seen in an ordered fcc structure (L1<sub>2</sub>). Structure L1<sub>2</sub> is a stable ordered fcc structure normally observed for a binary system like B<sub>3</sub>A, such as Gu<sub>3</sub>Au [15]. However, that arrangement requires atom A and B to share a common fcc structure. In the case of ZrN, it is a NaCl type structure with two sets of fcc structure overlapping, one from Zr atoms and the other from N atoms. The atomic ratio between two atoms in B<sub>3</sub>A is also significantly different than that in ZrN. Therefore, the L1<sub>2</sub> ordered structure could not be used to explain the extra diffraction spots in ZrN irradiated to 70 dpa. It is assumed that the observed structure ordering is caused by the Zr atoms since its atomic scattering factor for electron is approximately 4 times of that for N atoms. Another possibility is that the ordered structure may be due to ordering of interstitial or vacancy Zr atoms in the irradiated ZrN. The exact cause for the observed diffraction patterns in the 70 dpa ZrN can not be confirmed. The details and the mechanism of ordering for Zr atoms in ZrN under Kr irradiation are beyond the scope of this work.

Similar to ZrC, a large increase of approximately ~ 9% in the lattice constant was observed, shown in Figure 7. It may be assumed that a significant fraction of Zr atoms are in interstitial sites. The lack of Kikuchi patterns at 70 dpa indicates a severe distortion of the atomic planes. The lack of bubble growth and void formation may be partially due to the large fraction of interstitial Zr atoms that increase the internal stress in compression and the energy required for cavity development.

#### 4.2.3.3 TiC & TiN

Microstructure changes due to Kr ion irradiation at 800°C for titanium carbide and nitride are relatively simpler than zirconium carbide and nitride. The obvious difference is the evolution of the dislocation loops by irradiation. Although TiN has significant fraction of porosity as

revealed by SEM, observation in TEM indicated no cavity or voids in the matrix. The fraction of porosity in TiN shown in Figure 1 should have no effect on the microstructure evolution under Kr ion irradiation. Network dislocations and dislocation loops are observed in the irradiated TiC and TiN, but not in ZrC and ZrN. At a dose of 70 dpa, the change on the visibility of Kikuchi patterns is not obvious, indicating the radiation damage on atomic planes is minor.

The diffraction patterns of the unirradiated and the irradiated TiC and TiN to 70 dpa remained nearly the same. No radiation induced precipitates, ordering or amorphization are identified at a dose of 70 dpa. It appears that the development of dislocations and loops is beneficial for TiC and TiN leading to more stable microstructures under Kr ion irradiation than ZrC and ZrN. Since the dislocation loops are identified as perfect loops, their contribution to mechanical property degradation at high temperature is expected to be minor. Also these loops and dislocations could be beneficial at high temperature by improving the ductility due to the presence of mobile dislocations. Although voids are present in the irradiated TiC, its contribution on swelling is negligible ( $\sim 0.01\%$  at 70 dpa). Besides the radiation induced dislocation network and loops, the main damage from irradiation is still an increase in lattice spacing of approximately  $\sim 2\%$  for TiC and TiN.

#### 4.2.3.4 SiC

The microstructure characterization for both unirradiated and irradiated 6H-SiC suggests that SiC has the least radiation damage than the other 4 ceramics that are all in fcc structure. The lack of evidence from ion milling damage for the unirradiated sample is not expected since the other 4 ceramics all suffer certain degree of ion milling damage during sample preparation. SiC has the largest unit volume ( $0.1242 \text{ nm}^3$ ) lowest molecular weight (40.1) among the 5 ceramics and the smallest atomic size for Si comparing to Ti and Zr. These differences may be partially responsible for its good resistance to the ion milling damage.

Since SiC is a very hard material, the dislocations in the unirradiated SiC are believed to be introduced during material fabrication. The stacking faults in 6H-SiC are a common feature in microstructure for this material. Although some details of the projection of atomic layers along [0001] direction are revealed, Figure 17, the high quality high resolution image with much more details on atomic arrangement can only be obtained using the high-resolution TEM microscope. Nevertheless, the fine details in Figure 16 and 17 still provide useful information such as the spacing variation caused by stacking faults.

The lack of irradiation induced microstructural changes in the 10-dpa SiC indicates the material is not just resistant to the ion milling damage with Ar ions, but also resistant to high energy heavy ions up to a dose of 10 dpa. At high dose of 70 dpa, the loops are well developed. The threshold dose for loop formation must be greater than 10 dpa. This is different from TiC where loops are identified at 10 dpa. The average loop size for SiC at 70 dpa is roughly half of the loop size in TiN at 70 dpa. According to the work by Persson [9], these loops are most likely interstitial loops residing on (0001) planes. From the picture in Figure 19, the loops appear all in the shape of circular discs. A detailed study on the loop evolution as a function of irradiation dose and temperature is required to fully understand its role on microstructural evolution in 6H-SiC. The role of the loops in 6H-SiC on the mechanical and thermal stability needs further investigation. Although loops developed in SiC, the lack of degradation in Kikuchi pattern in the

convergent beam diffraction pattern indicates that the radiation damage on microstructure in SiC at 70 dpa is much less than in Zr and ZrN.

#### 4.2.4 Summary and Conclusions

To summarize this work: Refractory ceramics of ZrC, ZrN, TiC and TiN were irradiated with 1 MeV Kr ions at 800°C to 70 dpa. Zirconium carbide and nitride developed severe microstructure damage evidenced by the disappearance of Kikuchi patterns and a significant increase in lattice constant (7- 9%). An ordered microstructure was developed in ZrN at 70 dpa. No voids were found in the irradiated ZrC, ZrN and TiN. The microstructure stability under Kr ion irradiation for SiC, TiC and TiN is significantly better than ZrC and ZrN as evidenced by no obvious degradation in Kikuchi and diffraction patterns before and after irradiation and a smaller increase in lattice constant (~ 2%). Voids were only found in the irradiated TiC and the corresponding swelling is negligible (~0.01%). Dislocation networks and perfect loops were found in the irradiated TiC and TiN and are believed to be beneficial for microstructural stability under heavy ion irradiation. Dislocation loops are well developed in SiC at 70 dpa. Radiation-induced secondary-phase precipitates, amorphization are not found in the matrix of the carbides and nitrides. The cubic structure ceramics investigated in this work retain their fcc crystal structure at a dose of 70 dpa. 6H-SiC has been identified as the best on microstructural stability among 5 ceramics under Kr ion irradiation at 800°C.

6H-SiC was identified to be the best among 5 ceramics on microstructure stability under Kr ion irradiation at 800°C. The radiation induced increase in lattice spacing in TiC and TiN is approximately ~ 4 times smaller than in ZrC and ZrN. It appears that among the 5 ceramics, the one with lighter molecular weight performs better on the microstructure stability under heavy ion irradiation at 800°C. Si or Ti atom is smaller and lighter than Zr atom, leading to a difference in the strength of the covalent bonds between SiC, TiC (or TiN) and ZrC (or ZrN) that may affect the recovery of radiation induced defects. The better microstructural performance of TiC over ZrC under Kr ion irradiation is consistent with the work on neutron irradiated TiC and ZrC at a low temperature and dose [6].

A follow-on neutron irradiation at 800°C using the advanced test reactor at the Idaho National Laboratory have been planned, but at a much lower dose level ( ~ 1 dpa at 800°C). However, a high dose neutron irradiation at high temperature will be needed to verify the results from this work. The FUTURIX-MI irradiation program between DOE and CEA will provide critical neutron irradiation data to the GFR materials program.

Note that heavy ion irradiation of TEM disc samples has its limits when simulating neutron irradiation effect in bulk materials. Care has to be taken when applying these results to evaluate the material microstructural changes under neutron irradiation in reactors. Before high dose data of fast flux neutron irradiation at high temperature become available, a follow on study on using proton irradiation for the same set of ceramics is recommended. This will provide an opportunity to verify the results in this work while offer a limited mechanical test capability to evaluate the radiation effects on the materials mechanical property changes.

## References

---

- 1 L. W. Hobbs, F. W. Clinard, Jr., S. J. Zinkle and R. C. Ewing, J. Nucl. Mater., 216 (1994) 291
- 2 Minato, K., et al., 1997, J. Nucl. Mater. Vol. 249, pp 142-149.
- 3 Andrievskii, R., et al., 1978, Izv. Akad. Nauk SSSR, Neorg. Mater. Vol. 14, pp 680-83.
- 4 Kovalchenko, M., Rogovoi, Y., 1973, Izv. Akad. Nauk SSSR, Neorg. Mater. Vol. 9, pp 321-22
- 5 G.W. Keilholtz, R.E. Moore, and M.F. Osborne, Nuclear Application, 4 (1968) 330
- 6 D. A. Dyslin, R. E. Moore and H. E. Robertson, ORNL-4480 (1969) p245
- 7 W. J. Weber, L. M. Wang and N. Yu, Nucl. Instr. Methods in Phys. Research B., 116 (1996) 322
- 8 P. O. A. Persson, L. Hultman, M.S. janson and A. Hallen, R. Yakimova,, Journal of Applied Physics, V. 93, #5, (2003) 9395
- 9 P. O. A. Persson, L. Hultman, M.S. janson and A. Hallen, R. Yakimova, D. Panknin and W. Skorupa., Journal of Applied Physics, V. 92, #5, (2002) 2501
- 10 J. F. Ziegler, J. P. Biersack and U. Littmark, TRIM97 program, IBM Corp., Yorktown, New York, 1997
- 11 W. Lengauer, S. Binder, K. Aigner, P. Ettmayer, A. Guillou, J. Debuigne & G. Groboth, J. Alloys Compds., 217 (1995) 137-1
- 12 K. Aigner , W. Lengauer, D. Rafaja & P. Ettmayer, J. Alloys Compds., 215 (1994) 121-1
- 13 Binary Alloy Phase Diagrams, 2<sup>nd</sup> Ed., Editor: T. B. Massalaski, H. Okamoto, P. R. Subramanian and L. Kacprzak, ASM International
- 14 J. Li, J. Appl. Phys., Vol. 93, No. 11 (2003) 9072
- 15 A. Chakrabarti and A. Mookerjee, J. Phys: Condensed matter, 13 (2001) 10149



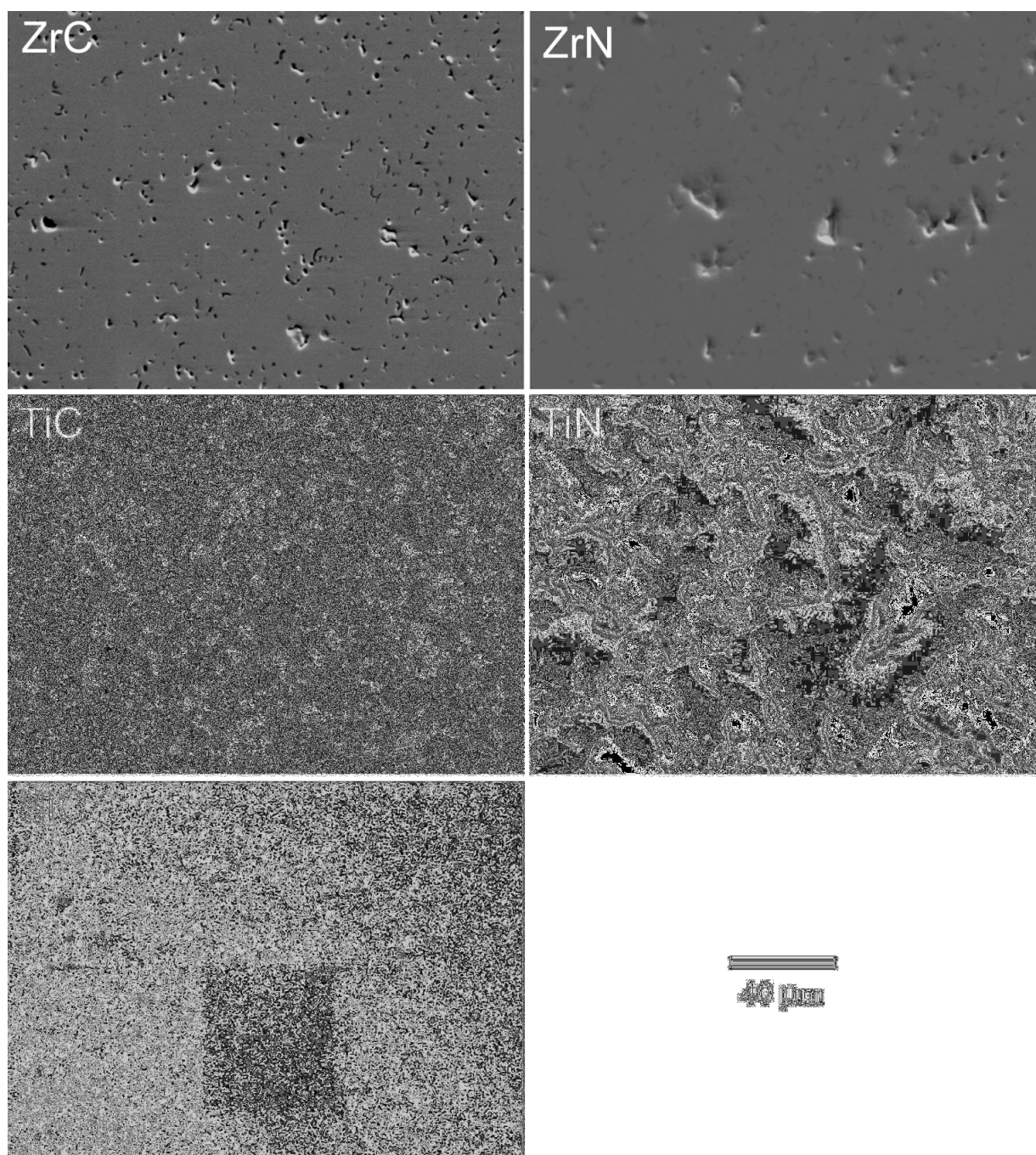


Figure 1. SEM images of the as-received ZrC, ZrN, TiC, TiN and SiC. The large fraction of porosity in TiN is consistent with its low relative density approximately 91% of the theoretic density.

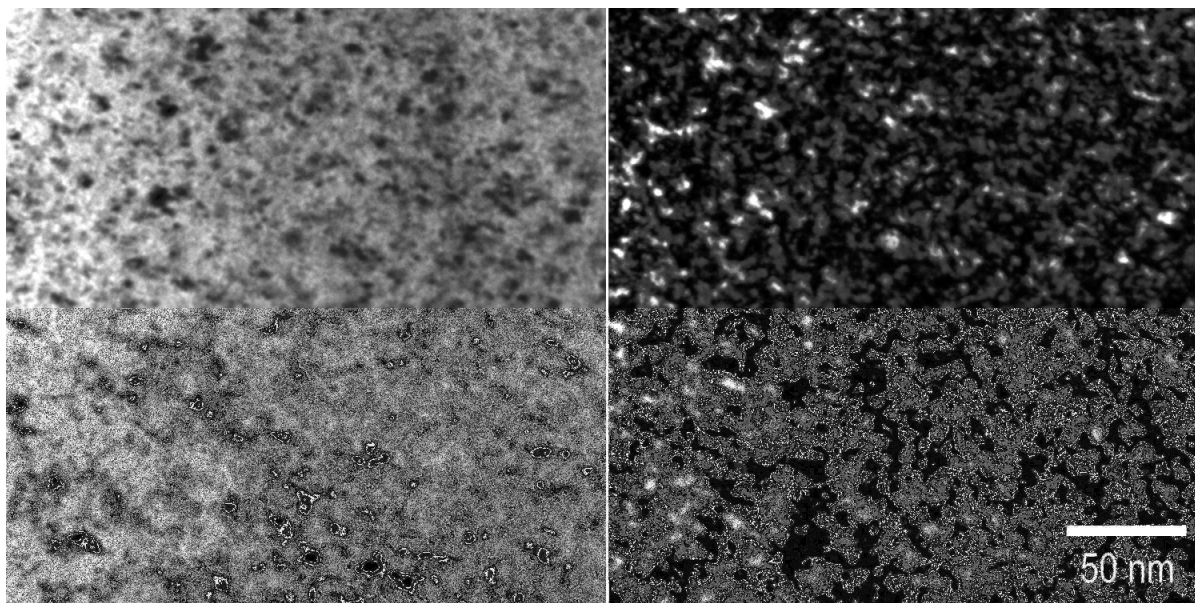


Figure 2. Microstructure of unirradiated ZrC imaged with  $g=200$  near zone  $[011]$ . The left is bright field image and the right is weak beam dark field image pair showing black dot damage from ion milling.

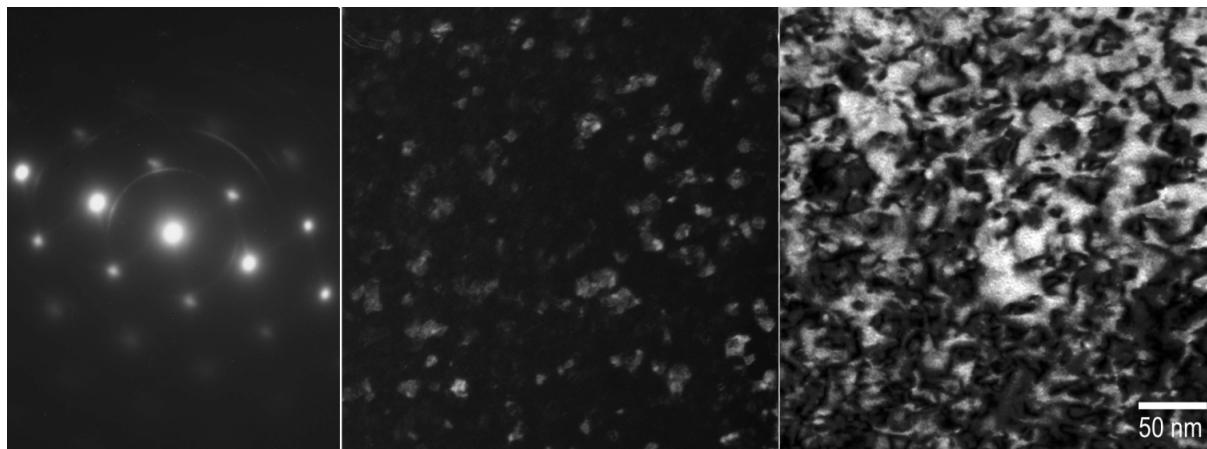


Figure 3a. ZrC irradiated at 800 °C to 10 dpa, showing a ring pattern (left), the dark field image using the 1<sup>st</sup> ring in diffraction (middle) and a  $g=200$  bright field image showing dislocations (right).

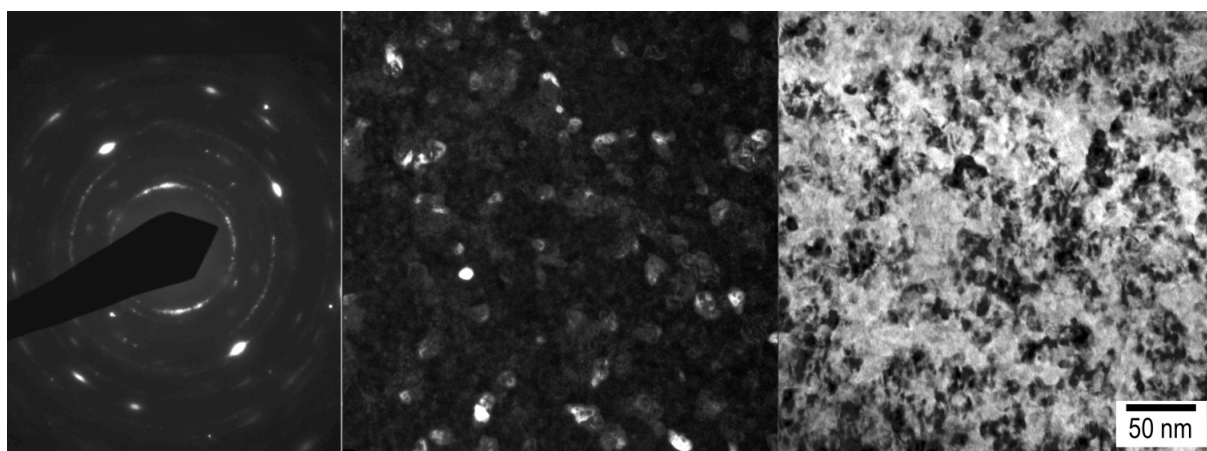


Figure 3b. ZrC irradiated at 800 °C to 70 dpa, showing ring pattern (left), the dark field image of precipitates using  $\langle 111 \rangle$  diffraction from the 1<sup>st</sup> ring (middle) and a  $g=200$  bright field image showing dislocations (right).

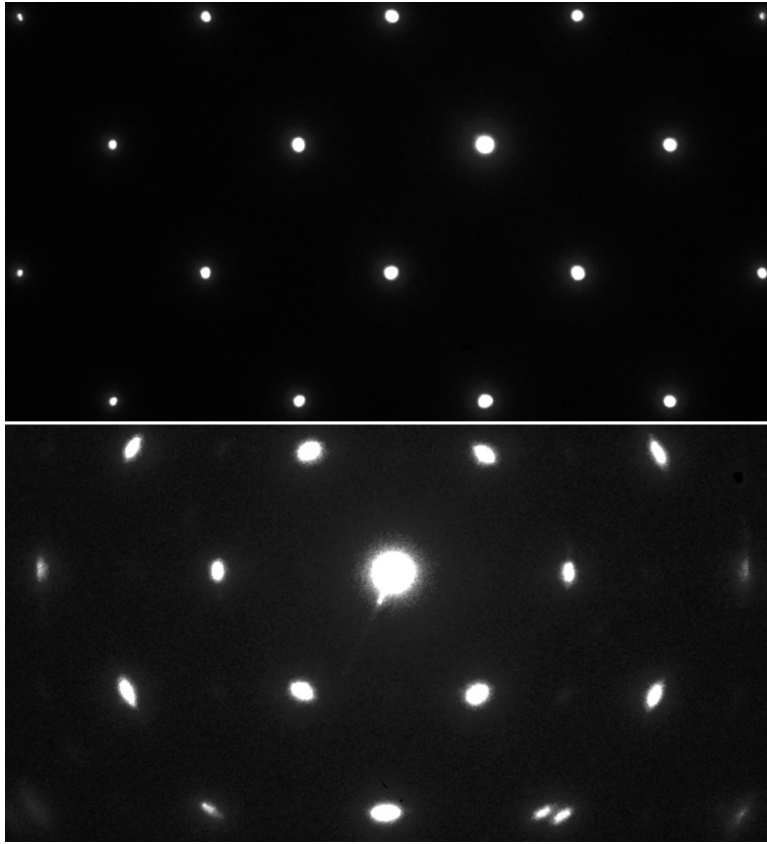


Figure 4. Selected area diffraction at zone [011] for ZrC, the unirradiated (top) and the irradiated to 70 dpa at 800°C (bottom) showing approximately 7% increase in lattice constant. Note that a shrink in the diffraction pattern spacing corresponds to an expansion in the real lattice space.

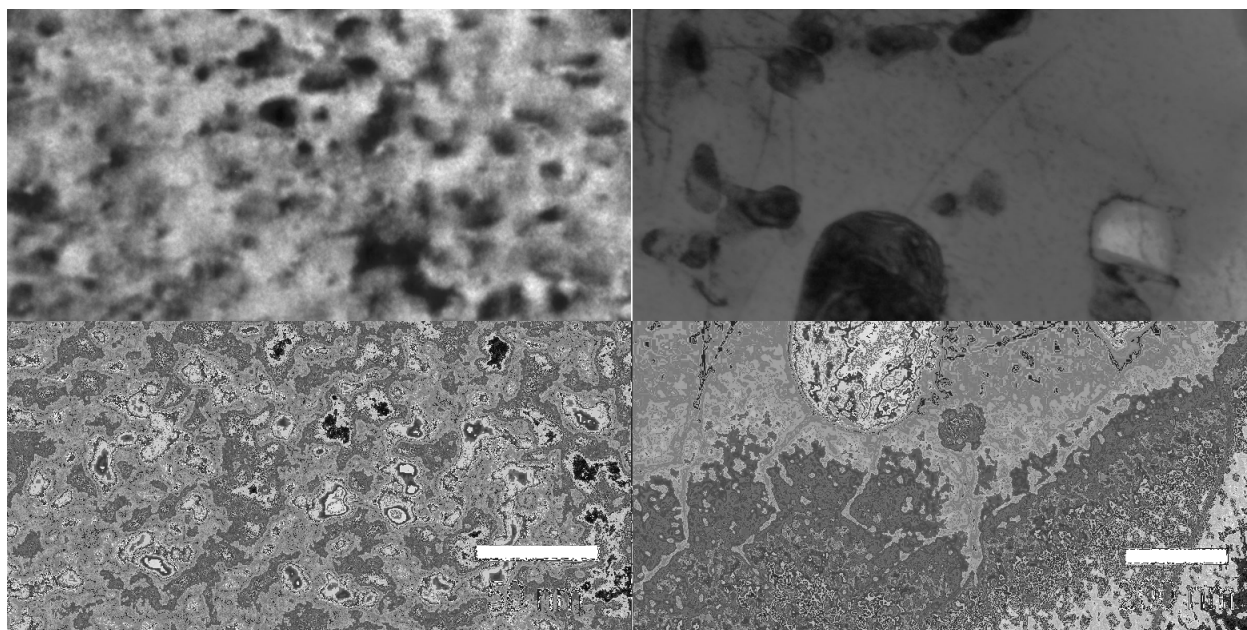


Figure 5. Microstructure of unirradiated ZrN imaged with  $g=200$  near zone  $[011]$  (left) showing damage from ion milling. The low magnification on the right shows an area with dislocations, voids, Zr-O precipitates (dark precipitates) and the fine defect clusters.

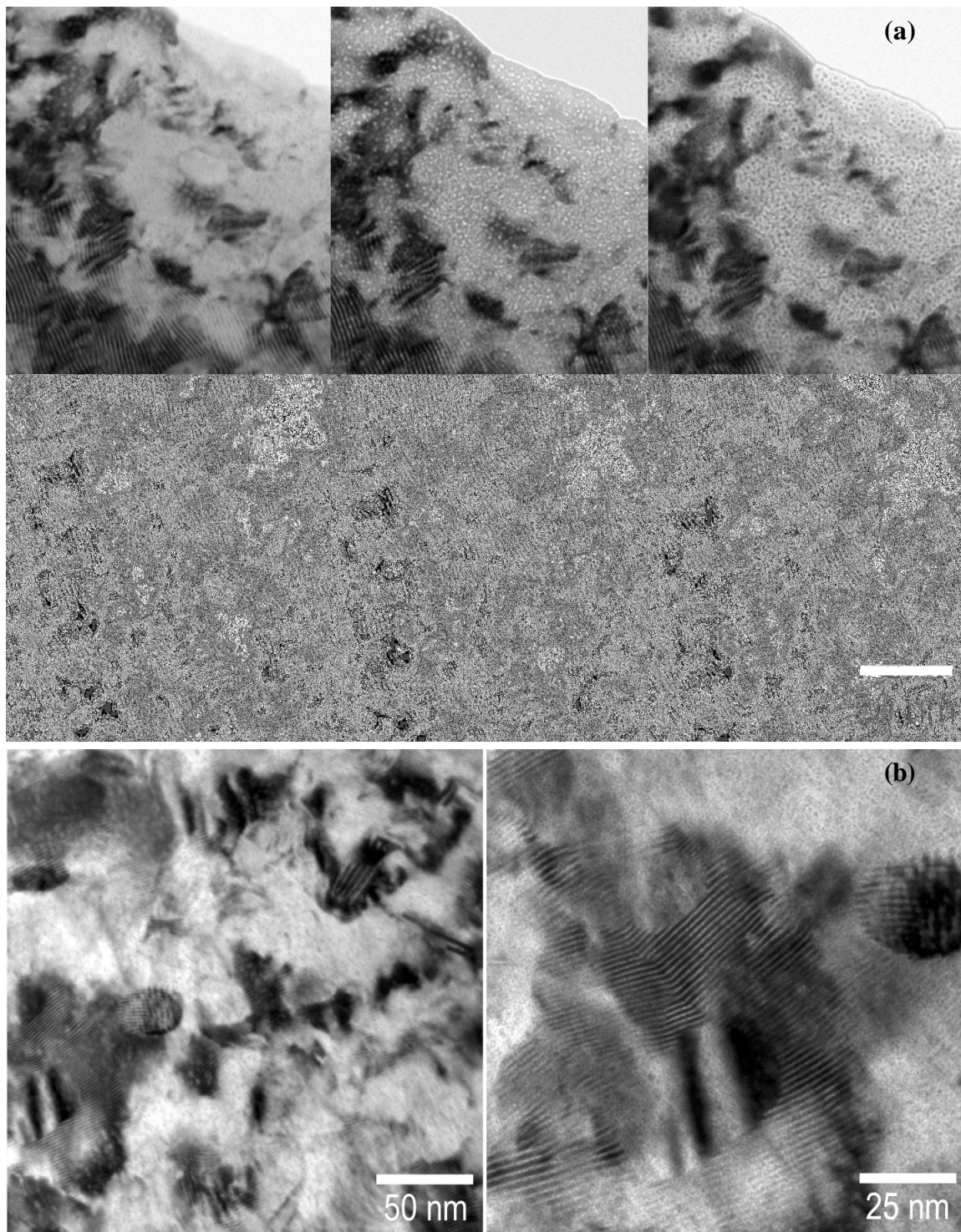


Figure 6. Microstructure of ZrN irradiated with 1 MeV Kr ions at 800°C to (a) 10 dpa (top) and (b) 70 dpa (bottom) imaged with  $g=200$  near zone [011] showing defect clusters with Moiré patterns. The images on top (10 dpa) also reveal the bubbles in the under-focus (middle) and over-focus (right) imaging condition.



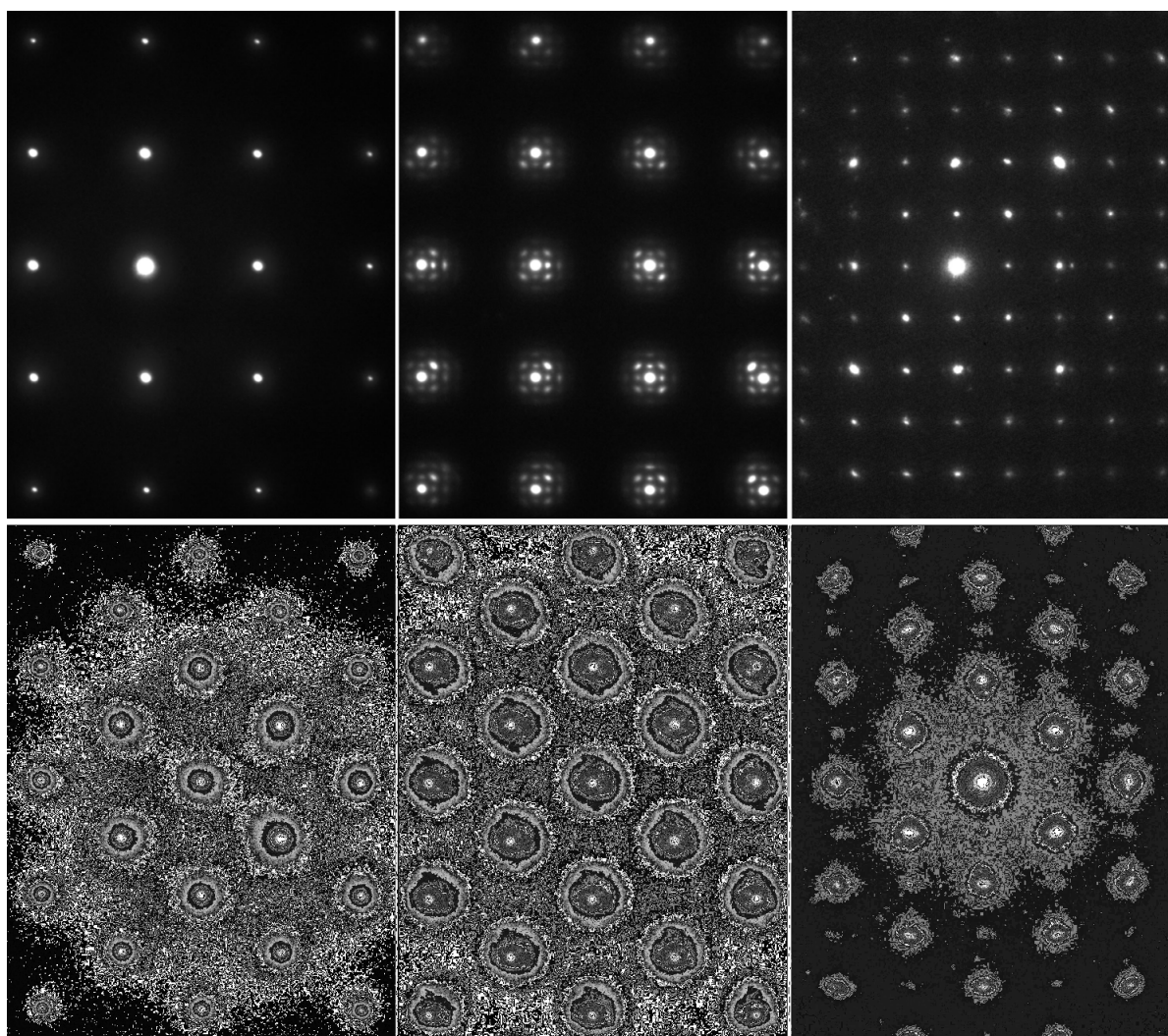


Figure 7. Comparison of diffraction patterns for ZrN at zone [011] (left) and [001] (right) between the unirradiated (top) and the irradiated (bottom) showing an ordered FCC ( $LI_2$ ) structure and a lattice increase of  $\sim 9\%$  due to irradiation.

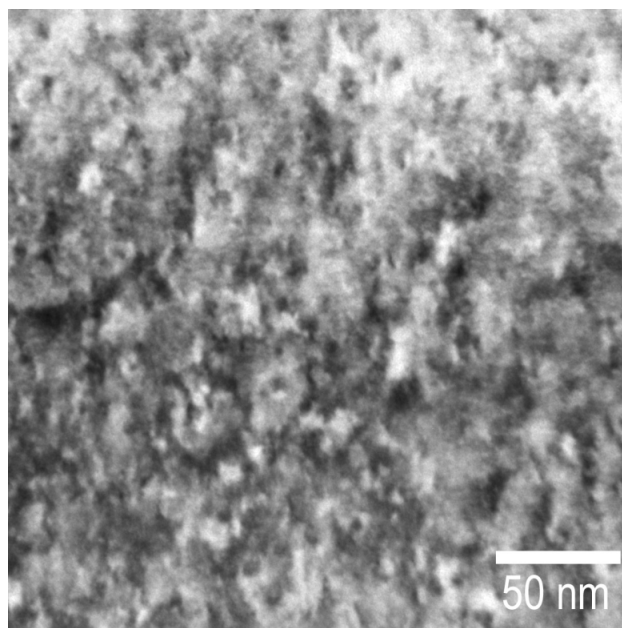


Figure 8. Microstructure of the unirradiated TiC imaged with  $g=200$  showing defect clusters due to ion milling damage.

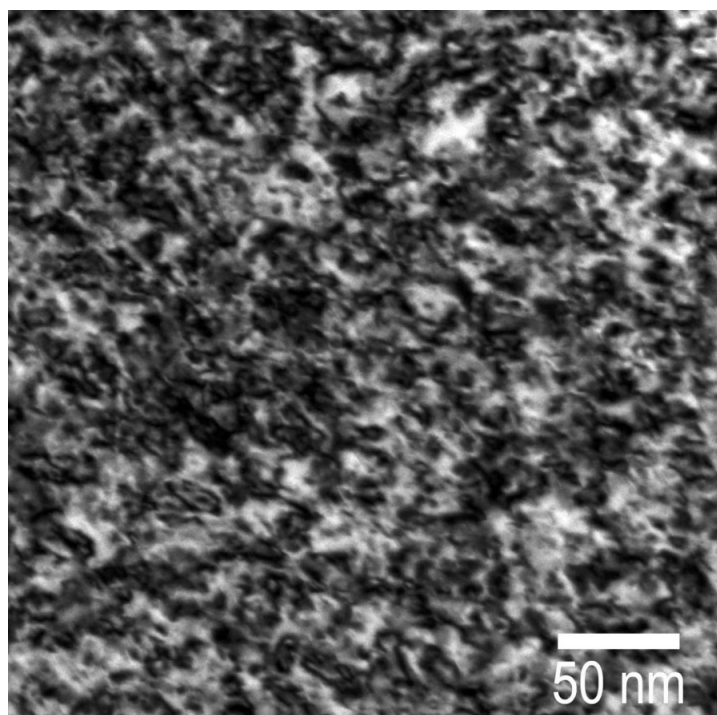


Figure 9. Microstructure of the 10-dpa irradiated TiC imaged with  $g=200$  showing dislocation loops.



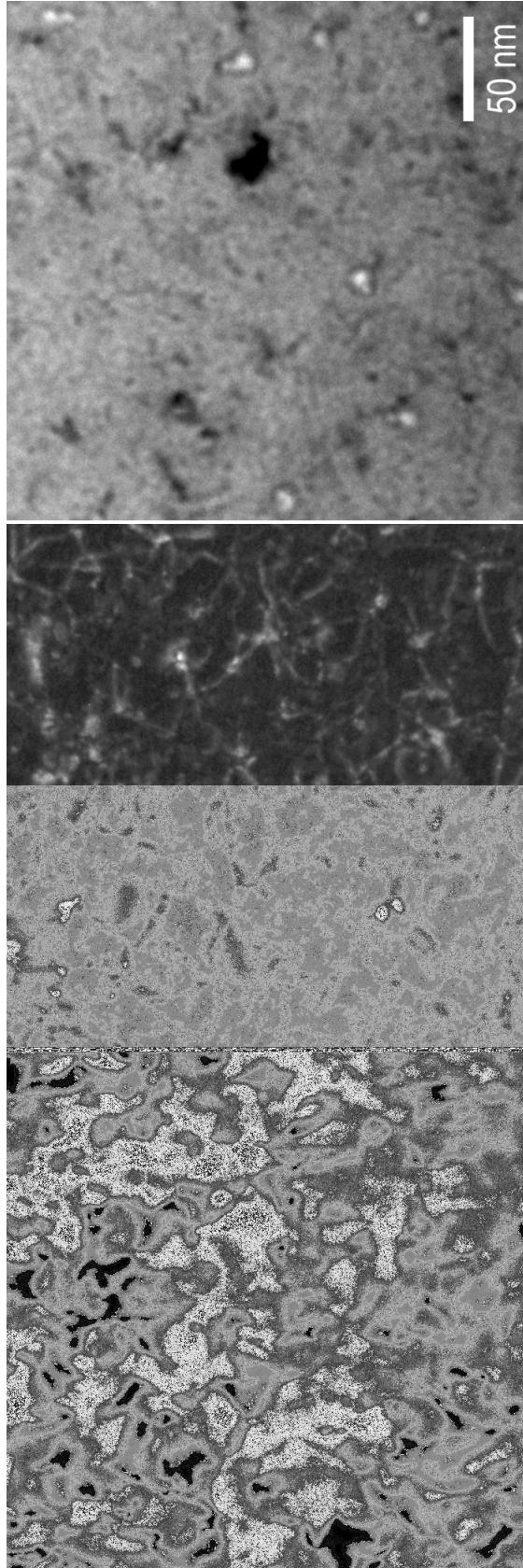


Figure 10. Microstructure of TiC irradiated with Kr ions to 70 dpa at 800°C (imaged with  $g=220$ ) showing dislocations in bright field (left), weak beam dark field ( $3g$ ) (middle) and voids (right).

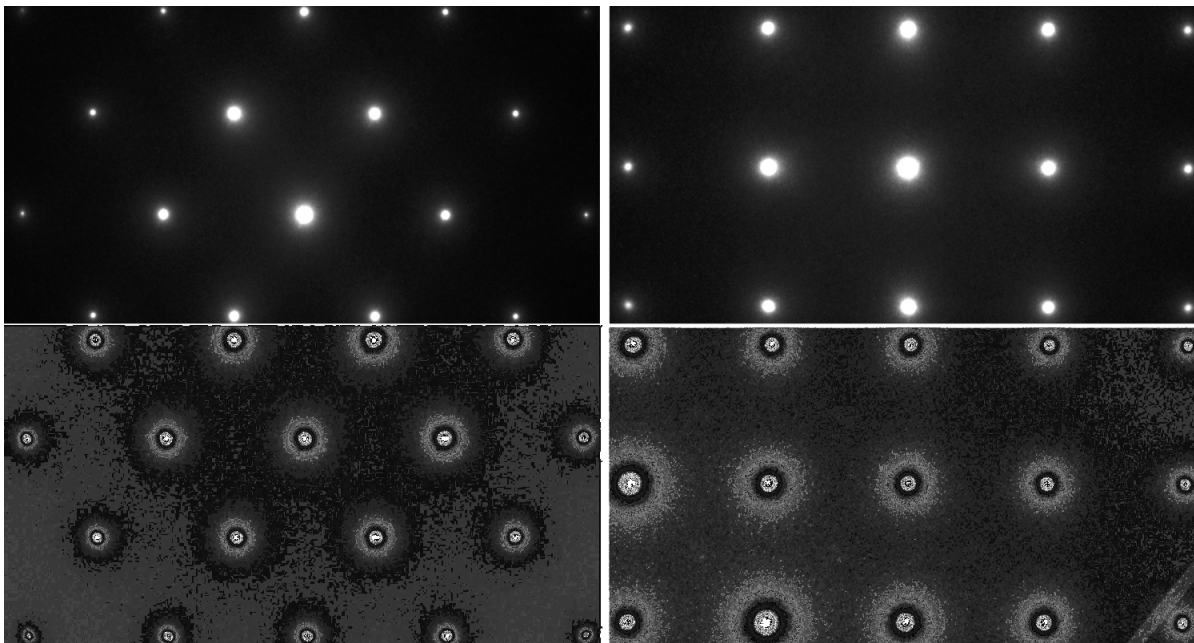


Figure 11. Comparison of diffraction patterns for TiC at zone [011] (left) and [001] (right) between the unirradiated (top) and the irradiated to 70 dpa at 800°C (bottom) showing a lattice increase of  $\sim 2.4\%$  due to irradiation.

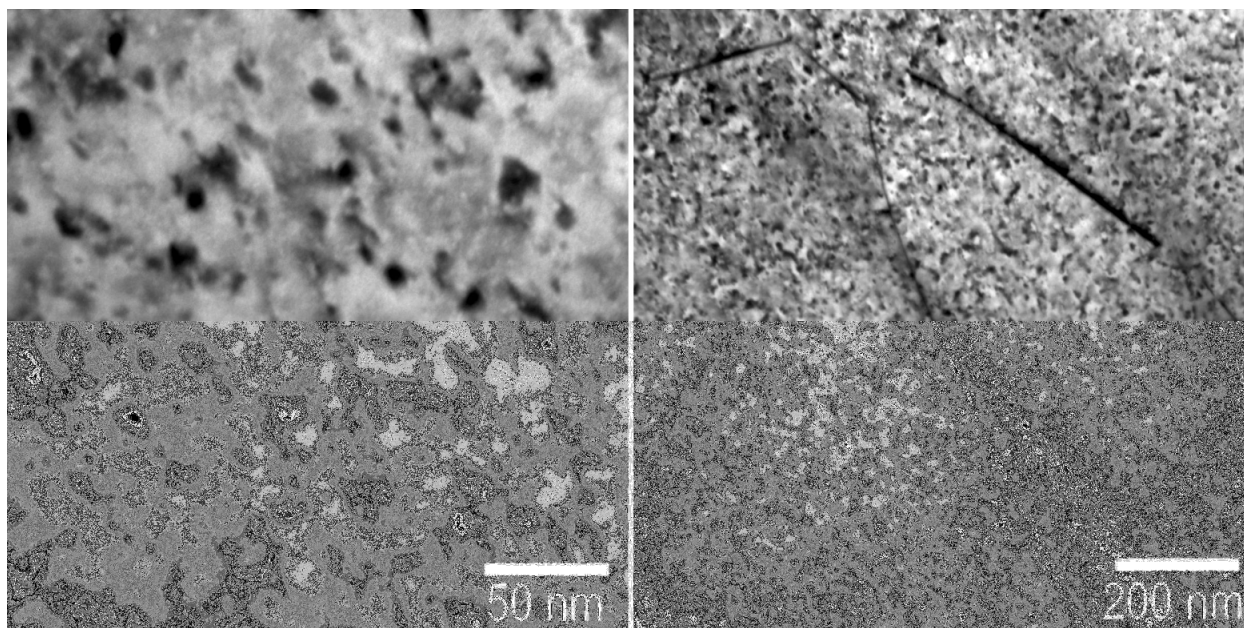


Figure 12. Microstructure of the unirradiated TiN imaged with  $g=200$  showing defect clusters from ion milling damage (left) and dislocations at low magnification (right).

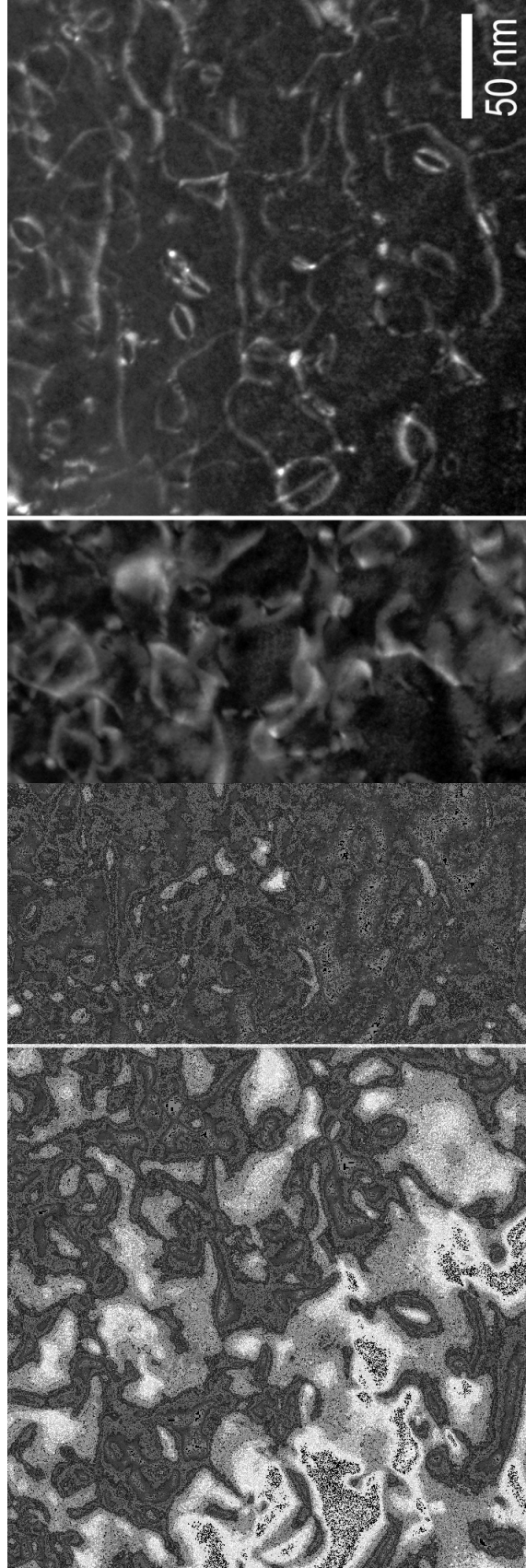


Figure 13. Microstructure of TiN irradiated with Kr ions to 70 dpa at 800°C showing dislocations in the same area imaged with  $\mathbf{g}=200$  bright field (left), weak beam dark field (middle) and with  $\mathbf{g}=0-22$  (right). The loops were identified with a Burgers vector of type  $0.5a_0[011]$ .

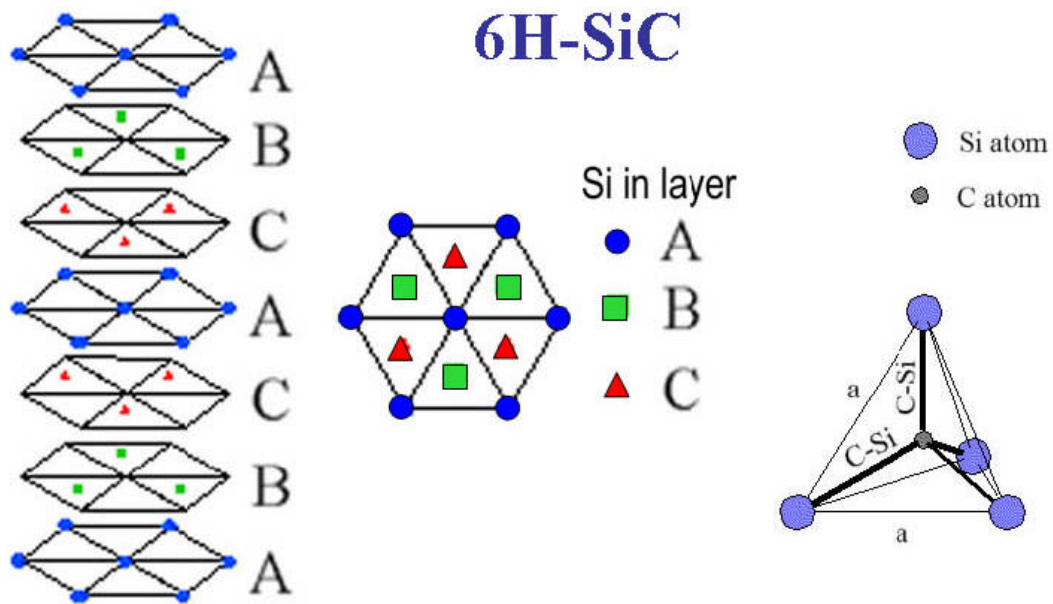


Figure 14. Crystal structure for 6H-SiC. It is a hexagonal with  $a = 0.30806$  nm and  $c = 1.51173$  nm. The stacking sequence repeats itself after every 6 layers of Si along the  $[0001]$  direction.

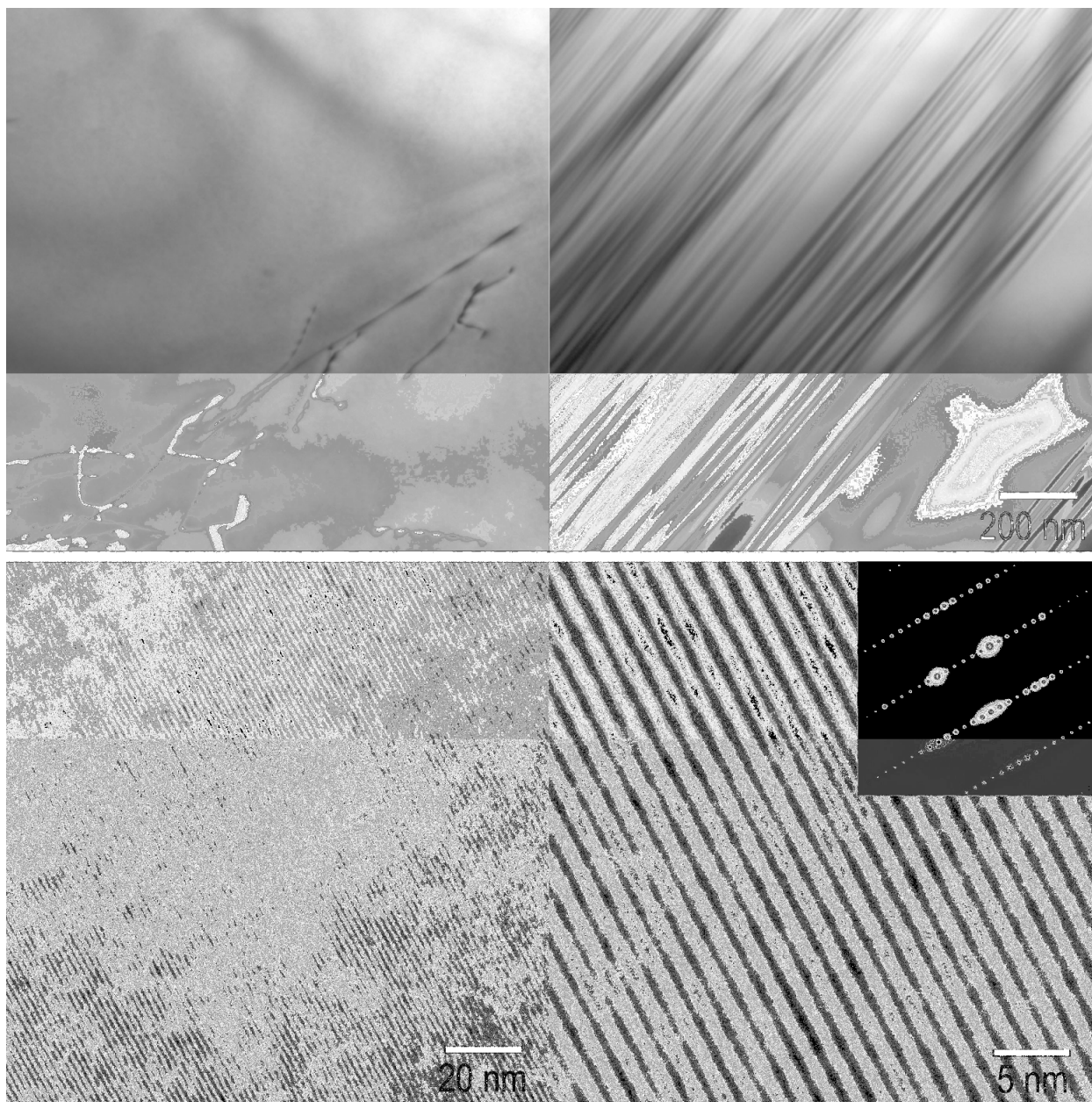


Figure 15. Microstructure of the unirradiated SiC. It shows scattered dislocations (top-left) and a group of stacking faults (top-right). The high resolution images (bottom) reveal the projection of basal planes at edge-on condition. The insert shows the diffraction at zone  $[hkil]=[1,-2,1,0]$  which is used to form the high resolution images.



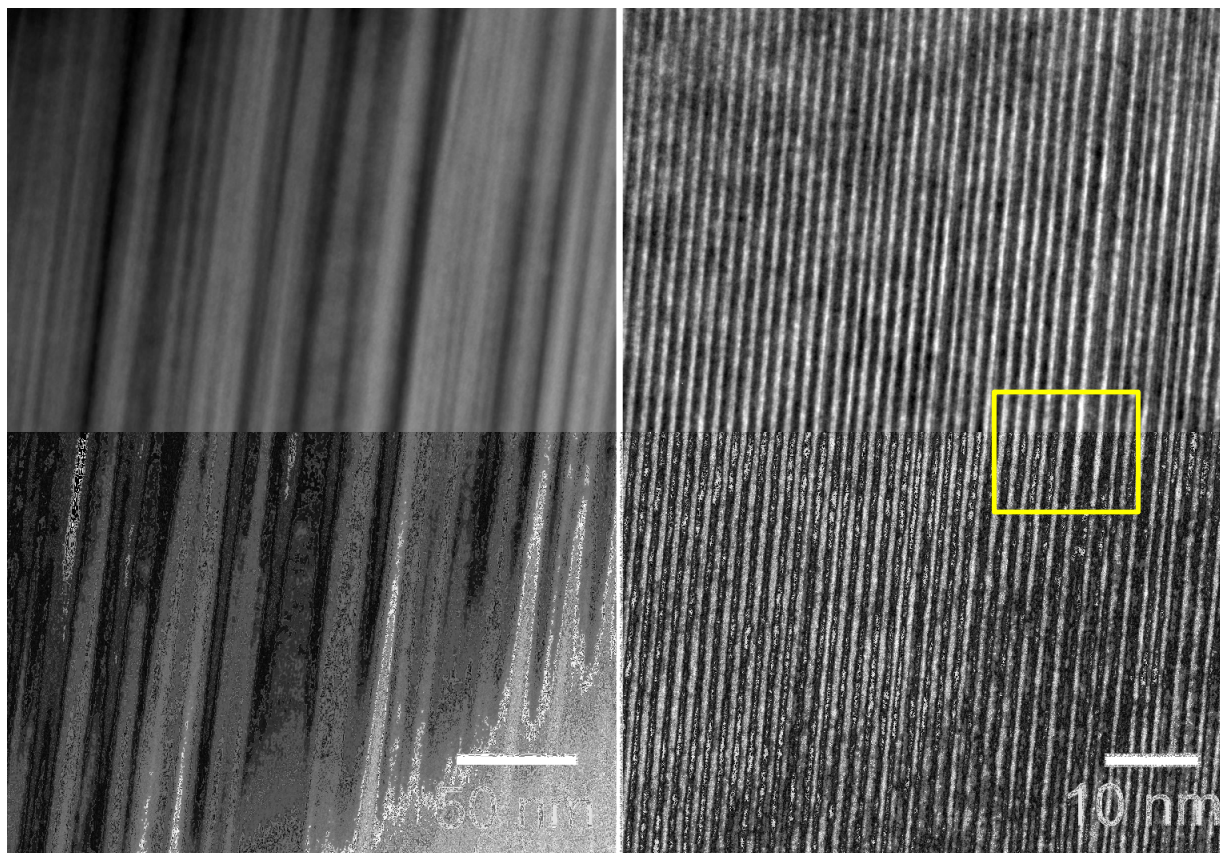


Figure 16. A close look at the details of the stacking faults. Note the spacing variation between the lines (projection of the basal planes) in the high resolution image (right) which reveals the stacking faults on basal planes.

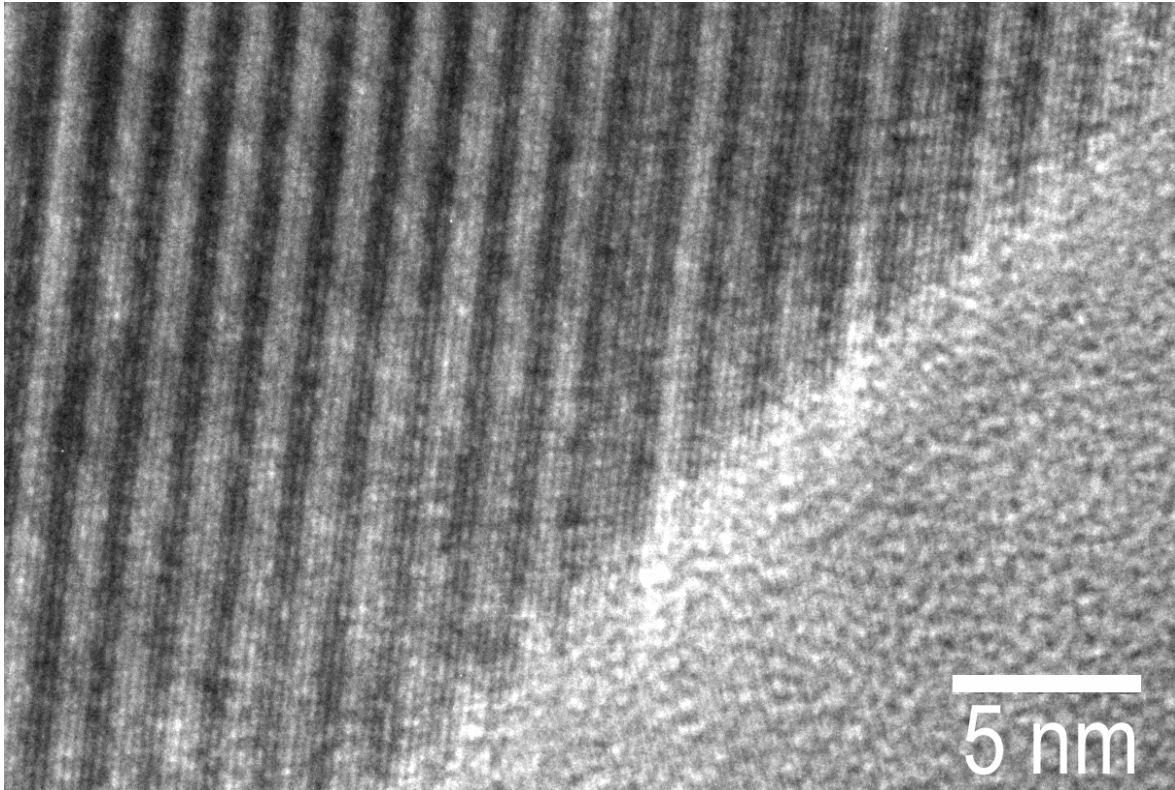


Figure 17. The details of the fine lines inside the major fringes in the picture correspond to 6 atomic layers in 6H-SiC. There are 6 fine lines between any two neighboring major fringes. The picture also shows a grain boundary.



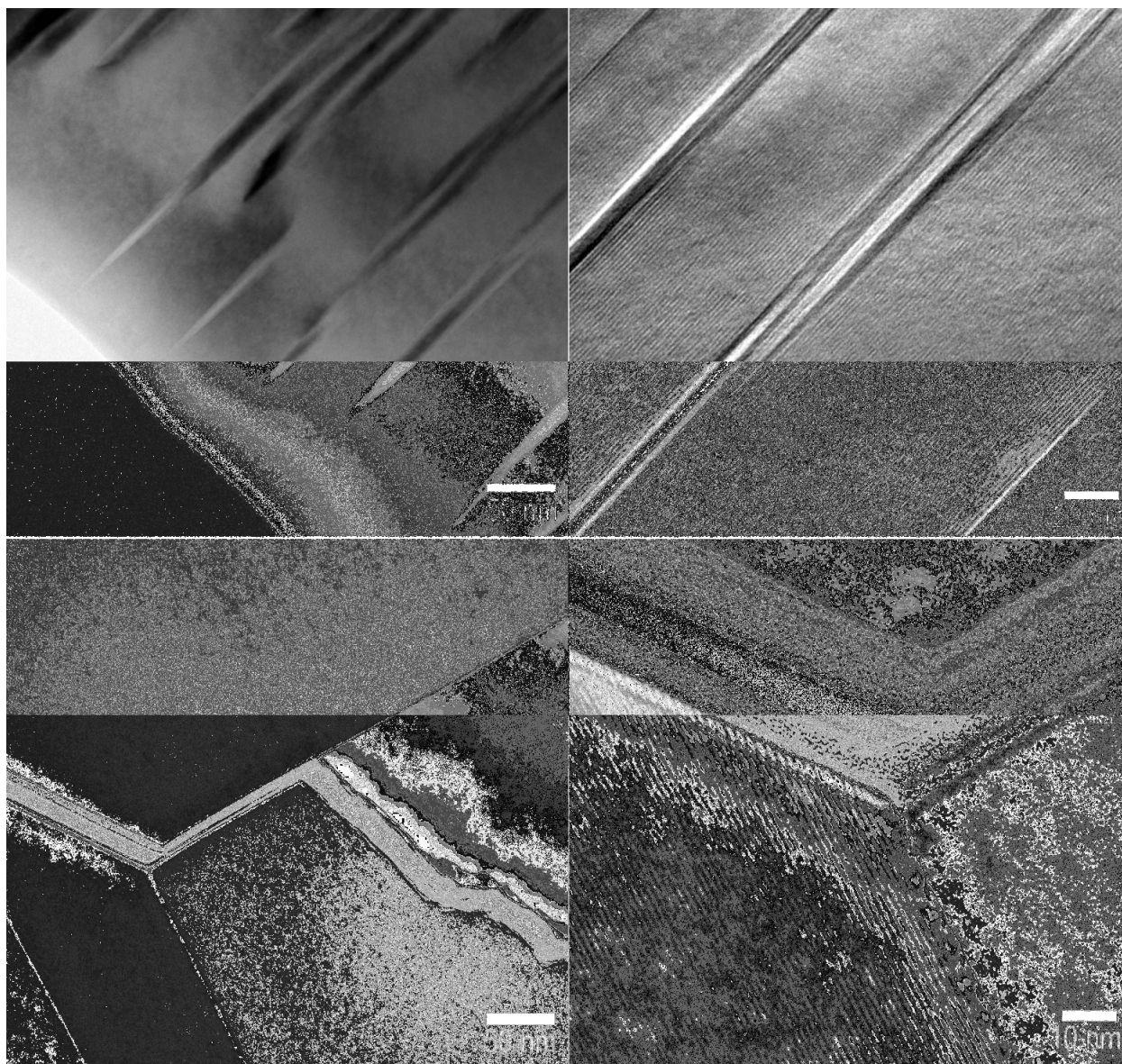


Figure 18. Microstructure of 6H-SiC irradiated with 1 MeV Kr ions to 10 dpa at a temperature of 800 °C. Radiation induced defects are not visible at this dose. The picture on the top shows a group of stacking faults similar to the unirradiated sample condition. The picture on the bottom shows a fracture at grain boundary triple junction. Pictures on the right provide a detailed view of the same area shown on the left.

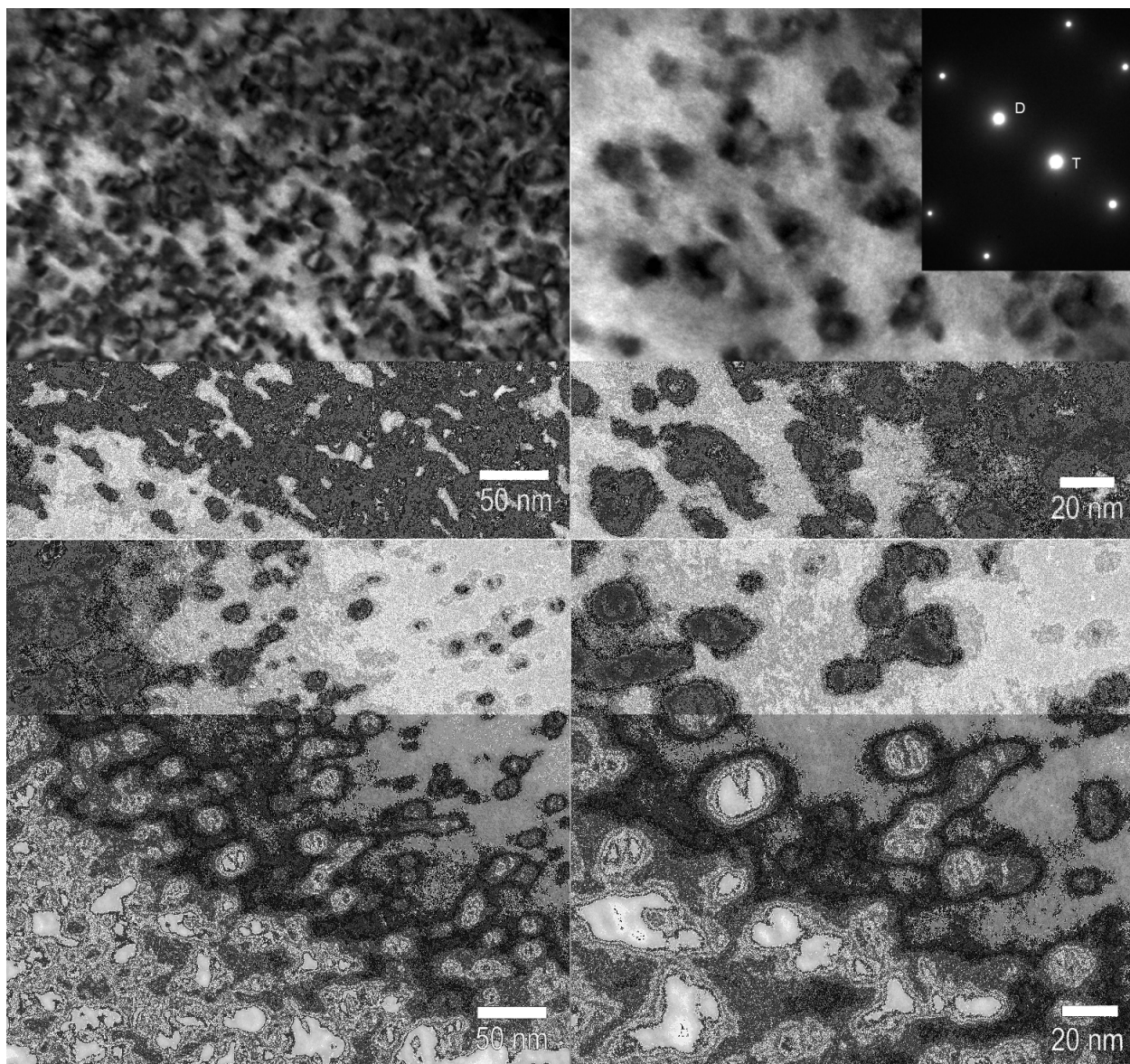


Figure 19. Microstructure of 6H-SiC irradiated with 1 MeV Kr ions to 70 dpa at a temperature of 800 °C. Dislocation loops are imaged with  $g = [2,-1,6]$  and the exact diffraction condition for the loops in the pictures (top) is shown in the insert. The pictures on the right provide a detailed view of the same area shown on the left.

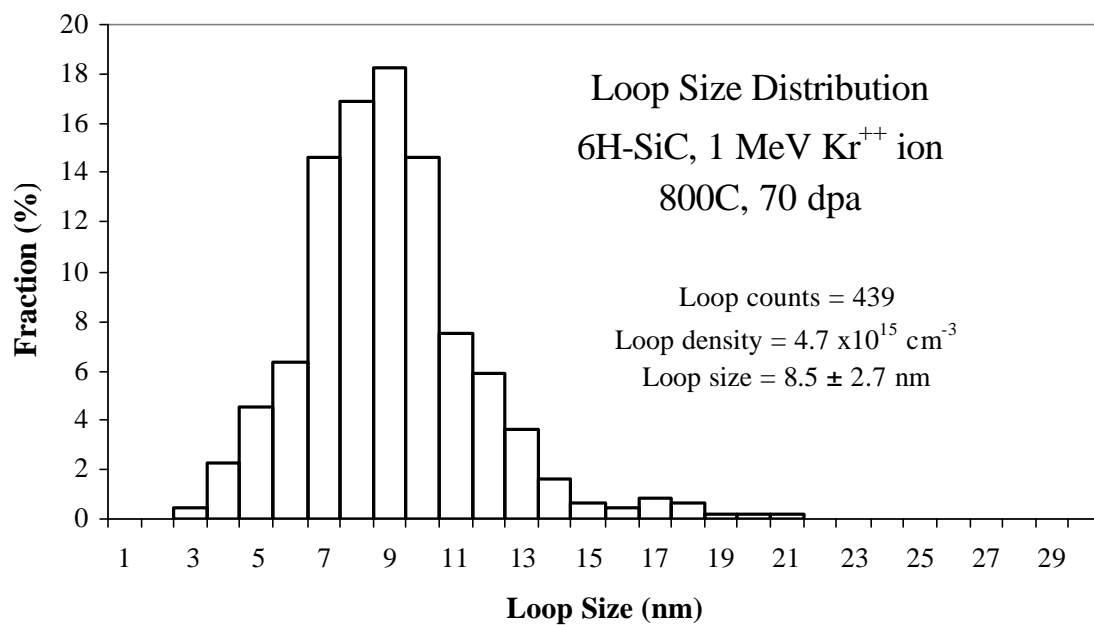


Figure 20. Loop size distribution for 6H-SiC irradiated with 1 MeV Kr ions to 70 dpa at a temperature of 800 °C.

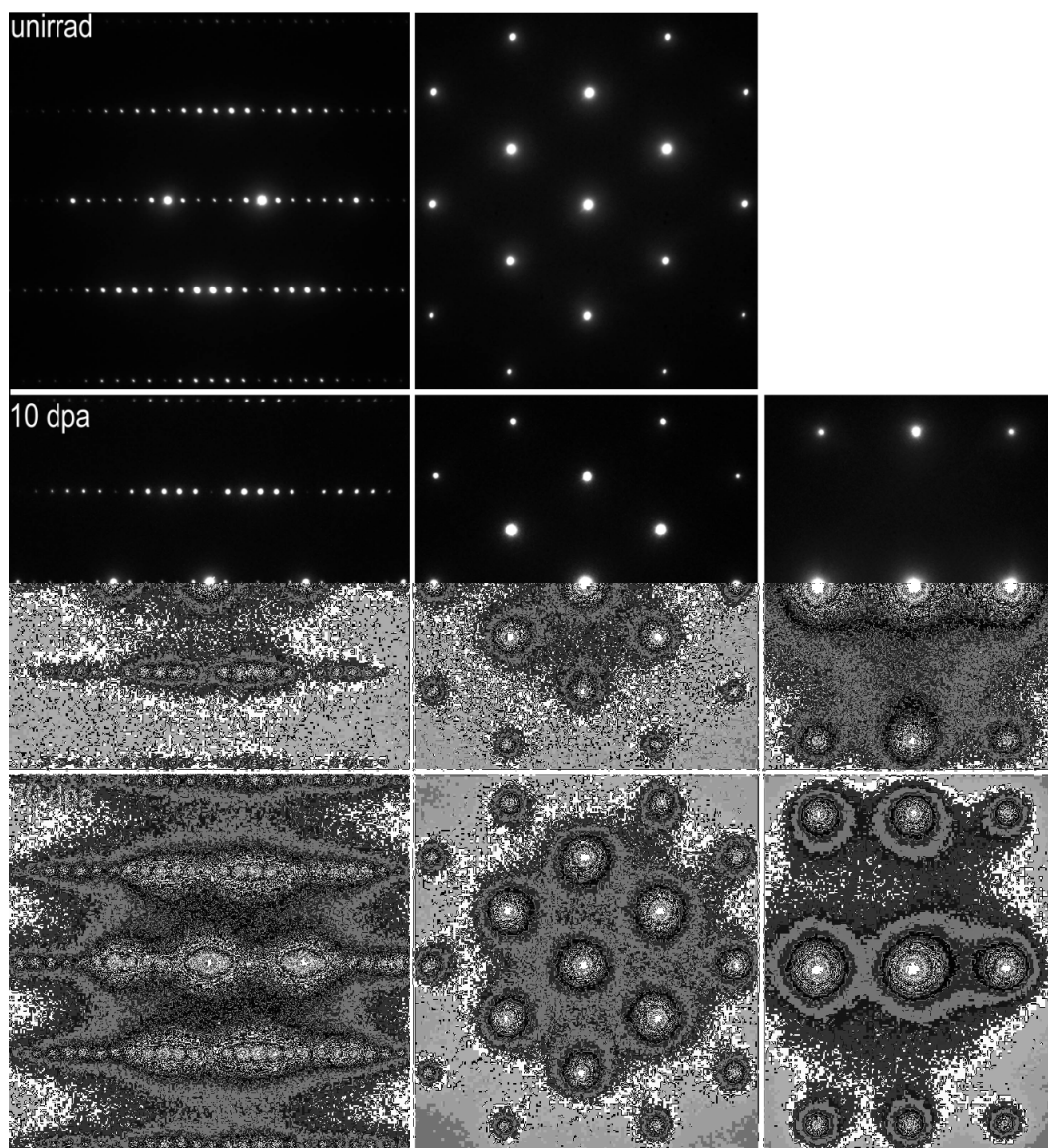


Figure 21. Diffraction patterns from the major zone  $[1,-2,1,0]$  (left),  $[0,2,-2,-1]$  (middle) and  $[0,-1,1,0]$  (right), for 6H-SiC in the condition of the unirradiated (top), irradiated at 800°C to dose of 10 dpa (middle) and 70 dpa (bottom) with 1 MeV Kr ions.

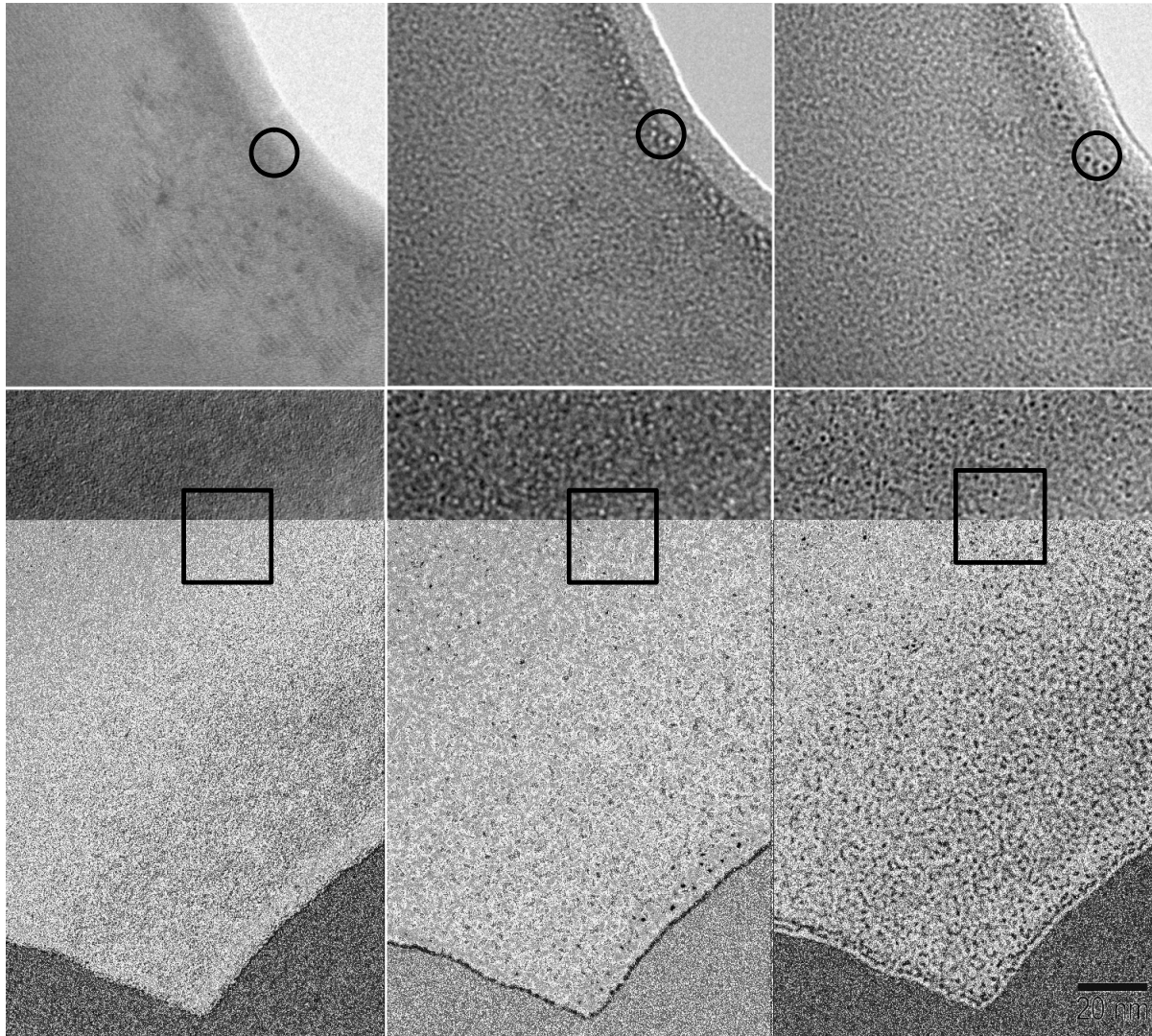


Figure 22. Small Bubbles ( $< 2$  nm) in the 6H-SiC irradiated with 1 MeV Kr ions at  $800^{\circ}\text{C}$  to 10 dpa (top) and 70 dpa (bottom) imaged under condition of in-focus (left), under-focus (middle) and over-focus (right). The density of bubbles is significantly higher in the 70 dpa sample. Small bubbles appear white and black dots with the under-focus and over-focus imaging condition, respectively.

## References



### **4.3 Grain Boundary Engineering**

#### **4.3.1 Coordination for I-NERI Project 2004-007-F**

On July 25, 2005 a review meeting was held at CEA Saclay of I-NERI project 2004-007-F, titled “Evaluation of Materials for Gas-Cooled Fast Reactors.” Work done in France on high temperature properties of T91 was reviewed. Additionally, work done in the U.S. on grain boundary engineering (GBE) on T91 and Alloy 800H, as well as radiation damage studies on Alloy 800H was reviewed. Both sides agreed to focus future work on GBE of multiple alloys and thermal stability of T91 both with and without loading. GBE studies in the U.S. will expand beyond T91 and 800H to include other ferritic-martensitic steels like HT9 and HCM12A, as well as a nickel-base alloy 617. The detailed report of the FY 2005 U.S. work will be issued in the fourth calendar year of 2005 in the final report for NERI project 02-0110.

The planned thermal studies of T91 are based on two observations. First, CEA has determined that the microstructural development of T91 at high (~550°C) temperature is significantly different if the sample has been loaded as opposed to samples that are just held at temperature. Second, the U.S. has determined that the creep properties of T91 can be improved using a GBE treatment that reduces the fraction of high-angle grain boundaries. The two programs will study the following experimental space in the coming year. Two batches of T91 with different starting chemistry and heat treatment will be studied, one provided by the U.S. and the other by CEA. Two treatments will be studied, normalized and tempered as well as GBE-treated samples. Samples will be examined that have undergone deformation and those that have not. Samples will be exchanged so that each side can examine samples of various treatments. Samples will either be deformed in an inert atmosphere or heat-treated in a vacuum.

#### **4.3.2 Performance and Stability of Grain Boundary Engineering Alloy 800H**

##### *Specimen Preparation*

Two types of specimens were prepared to verify the performance of the GBE-treated 800H as compared to as-received 800H. One is a round cross-section as shown in Fig. 1(a), and the other is a rectangular cross-section as shown in Fig. 1(b). Creep testing is being performed at the Pacific Northwest National Laboratory (PNNL) at 500°C and 600°C on the specimens with round cross-section. Tensile tests will be performed at 750°C and 900°C on the specimens with rectangular cross-section at the Oak Ridge National Laboratory (ORNL) to evaluate the effect of irradiation.

##### *Thermal Stability*

GBE treatment has the ability to increase the population of coincidence site lattice boundaries (CSLBs), improving many properties, e.g. creep, stress corrosion crack, and oxide stability. To maintain the benefits of GBE when a component is employed at high temperature, the thermal stability of the population of CSLBs is important. Since Incoloy Alloy 800H is designed for application to temperatures of 760°C, thermal stability of GBE-treated samples was tested at three temperatures, i.e. 500°C, 600°C, and 760°C, in air for 675 and 1004 hours. As-received samples were also tested at the same time and temperature conditions for comparison.

Preliminary results of the GBE thermal stability with annealing temperatures at 500°C and 760°C are shown in Fig. 2. A higher number fraction of CSLBs and lower number fraction of HABs (high-angle boundaries) are preferred. Figure 2 shows that GBE treatments increase the fraction of CSLBs relative to the control samples. Annealing at 500°C does not affect the fraction of CSLBs and HABs significantly as compared to the non-annealed (0h) GBE samples. In contrast, annealing at 760°C decreases the fraction of CSLBs and increases the fraction of HABs relative to the samples with no anneal (0h). In addition to the annealing temperature effect on the thermal stability of GBE, longer annealing time impairs the effect of GBE.

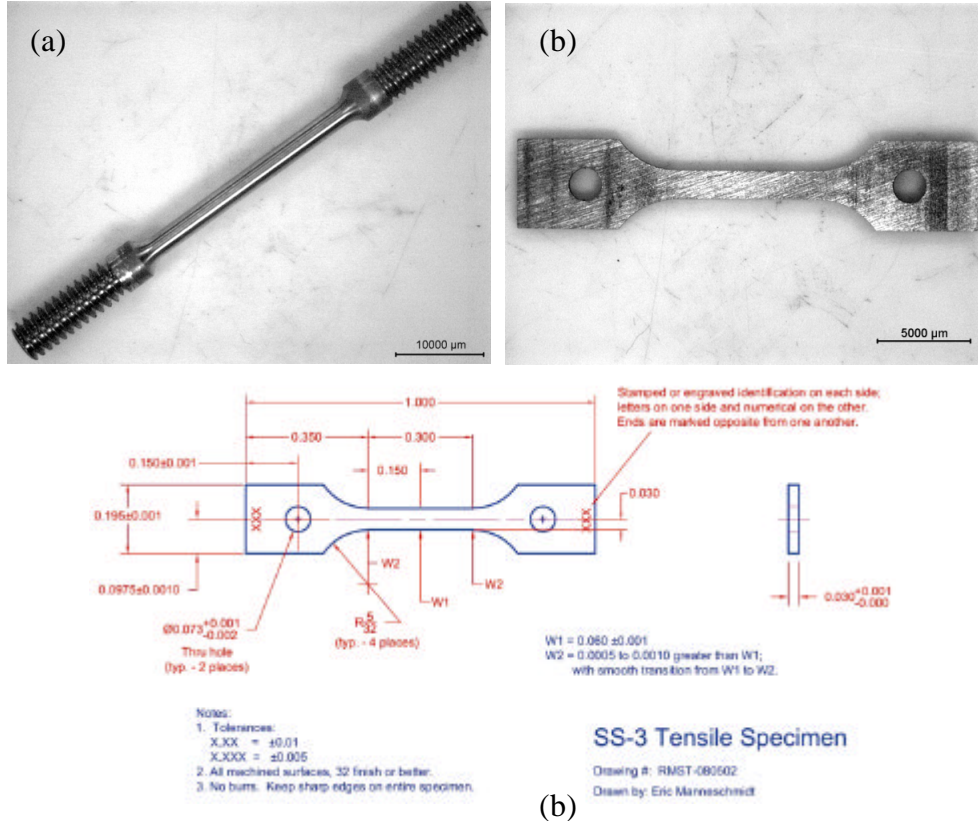


Fig. 1. Optical images of (a) mechanically machined creep test specimen with round cross-section, and (b) wire-EDM (Electro-Discharge Machine) fabricated tensile test specimen with rectangular cross-section. The design of the tensile specimen (b) is also included.

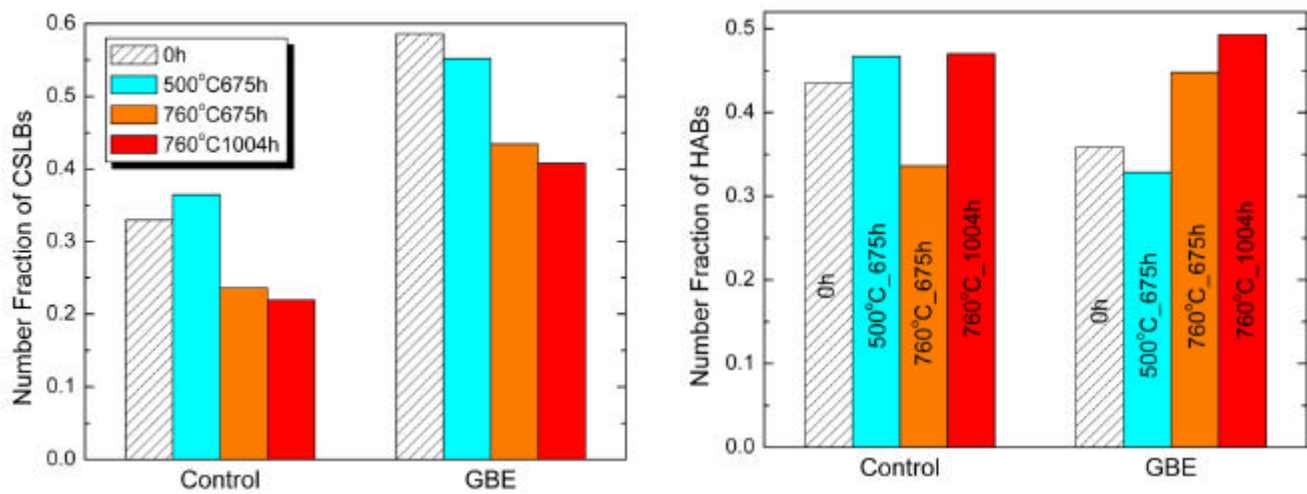


Fig. 2. Number of fraction of CSLBs and HABS of as-received and GBE-treated samples prior to annealing and annealing at 500°C and 760°C.



## 5. Fuels

While the fuels and fuel cycle work falls under the purview of AFCI, it is reported here due to its importance in the design of the GFR. Current fuel designs are based on dispersion fuels (either as fibers/small “pellets” or particles) in an inert plate/block type matrix, or solid solution fuel clad in a refractory ceramic (e.g., SiC/SiC composites). The reference fuels chosen for the GFR are mixed (i.e., U+Pu+MA) nitrides and carbides for their high heavy metal density, high conductivity, and minimal impact on neutron spectrum (although limited irradiation data exists). Most of the effort and work is focused on development of dispersion particle fuel, and fiber/stick/pellet fuels. Fuel particles have been successfully fabricated at ANL-W using a Rotating Electrode Process (REP) atomization. The process uses a low voltage, high current arc to melt a feedstock material, where droplets are flung from the rotating electrode (see Figure 1).

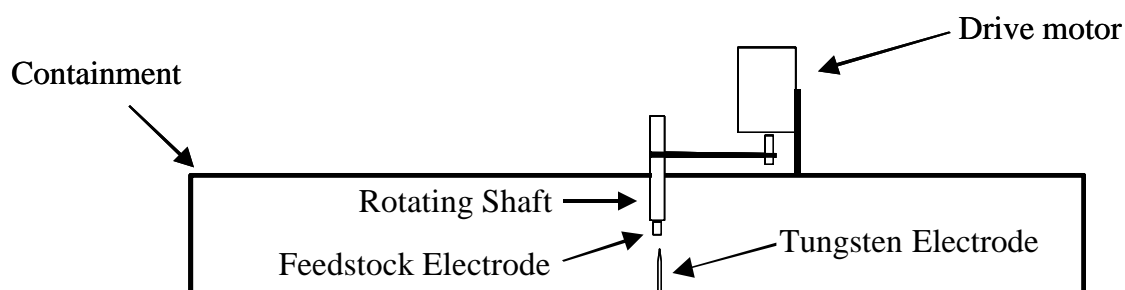


Figure 1. REP atomizer.

The droplet size depends on the rotational speed of the electrode, where the droplets are solidified into spheres. The feedstock is uranium carbide (UC), and is fabricated using simple resistance heating.

The heating time is ~ 30 s, and total production time < 1 hour. Fabricated UC particles can be seen in Figure 2.

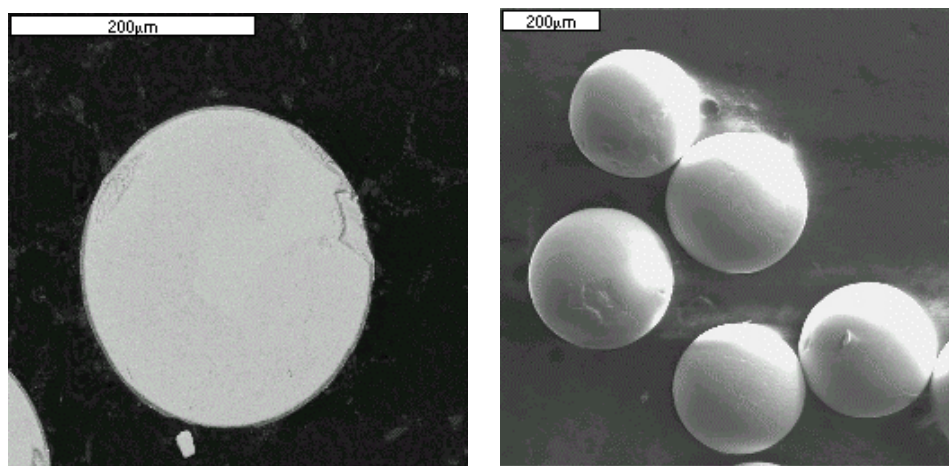


Figure 2. UC particles fabricated using the REP atomizer.

Advantages to using this process include a high yield and no liquid waste, but some shrinkage pores are evident.

A key issue for the particle fuel concerns the development of special coatings; particularly the use of non-halide precursors, and the development of low-density ceramic buffer layers. Through the previous I-NERI program, ORNL has been successful in coating surrogate particles, with a 50% dense SiC buffer layer, and dense (90%) SiC seal coat using non-halide precursors. Figures 3 and 4 are micrographs of the particles and coatings.

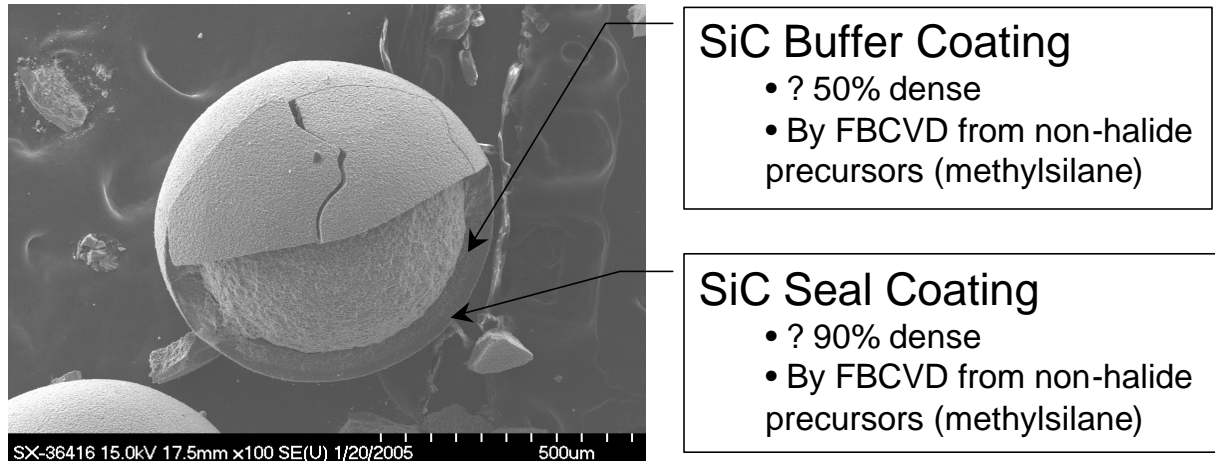


Figure 3. Successfully coated particle.

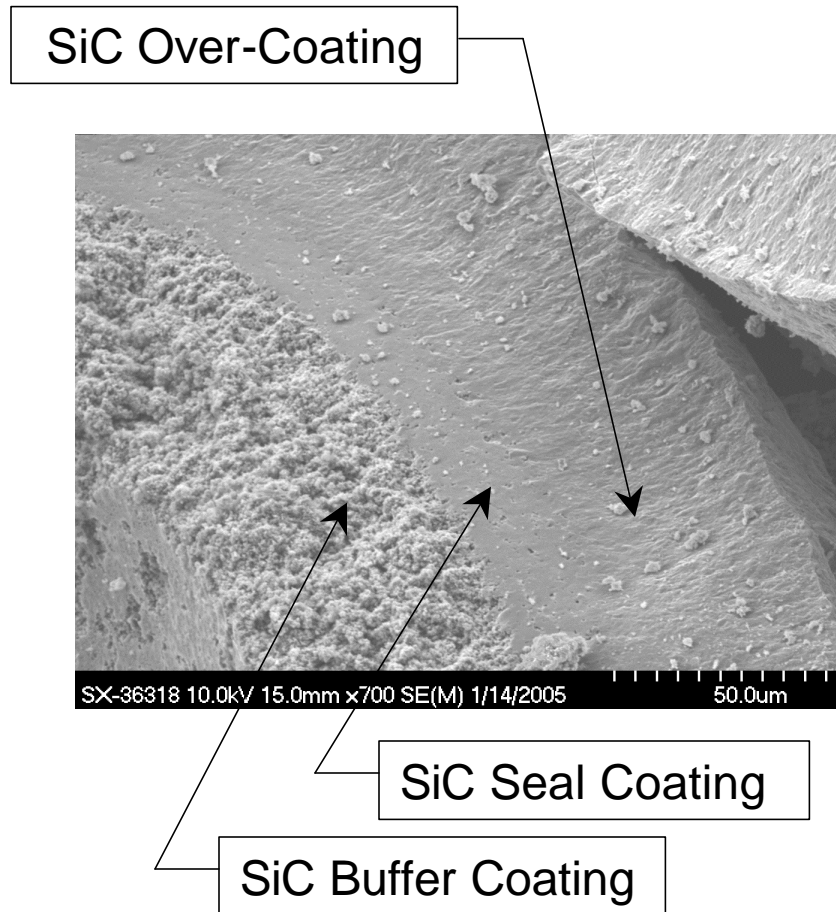


Figure 4. Micrograph of SiC coatings.

Fabrication of the matrix material continues. Current studies are focusing on using infiltration/reaction bonding to make SiC with imbedded fuel particles.